MODELING COLD-FORMED STEEL MEMBERS AND SYSTEMS

by

Guanbo Bian

A dissertation submitted to Johns Hopkins University in conformity with the requirements for the degree of Doctor of Philosophy

Baltimore, Maryland

May 2017

ABSTRACT

With the development of structural analysis software, computer simulation becomes an important tool for structural engineers and researchers to understand structural behavior. Structural performance can be evaluated by computer simulation at a low cost in contrast to physical experiments. The research in this dissertation is based on finite element analysis and simulation.

Torsion response for open cross-section members always interests researchers because of its complexity. In Chapter 2, torsional response of typical cold-formed steel members with channel cross sections was explored. Experimental and simulation results were compared with different boundary conditions. In the end of the chapter, a Direct Strength Method type design expression was provided based on simulation results.

Structural members, e.g. beam and column, are elementary components in a building. A subsystem is a higher-level component, e.g., lateral force resistance system and gravity load resistance system. Shear wall and diaphragm are crucial lateral force resistance subsystems in a building. A fastener-based CFS OSB sheathed shear wall model was developed and validated against existed shear wall experiments in Chapter 3. After that, this fastener-based shear wall model was used to illustrate gravity wall effect on wall line lateral force resistance and evaluate shear wall reliability. Chord stud buckling was also considered in the shear wall model by using a pinching04 model for chord stud element. The last two chapters include modeling work of bare steel deck panels.

The content in this dissertation has been presented in the following publications:

Bian, G., Peterman, K. D., Torabian, S., and Schafer, B. W. (2016). "Torsion of cold-formed steel lipped channels dominated by warping response." *Thin-Walled Structures*, 98 (2016): 565-577.

Buonopane, S. G., Bian, G., Tun, T. H., and Schafer, B. W. (2015). "Computationally efficient fastener-based models of cold-formed steel shear walls with wood sheathing." *Journal of Constructional Steel Research*, 110 (2015): 137-148.

Bian, G., Padilla-Llano, D. A., Buonopane, S. G., Moen, C. D., and Schafer, B. W. (2015). "OpenSees modeling of wood sheathed cold-formed steel framed shear walls." *Proceeding of the Annual Stability Conference: Structural Stability Research Council, Nashville, Tennessee* (pp. 24-27)

Bian, G., Padilla-Llano, D. A., Leng, J., Buonopane, S. G., Moen, C. D., and Schafer, B. W. (2015). "OpenSees modeling of cold-formed steel framed wall system." *Proceeding* of *the Eighth International Conference on Behavior of Steel Structures in Seismic Areas*. Shanghai, China.

Bian, G., A. Chatterjee, Buonopane, S. G., Arwade, S. R., Moen, C. D., and Schafer, B. W. (2017). "Reliability of cold-formed steel framed shear walls as impacted by variability in fastener response." *Engineering Structures* 142 (2017): 84-97.

Bian, G., Torabian, S., and Schafer, B. W. (2016). "Reduced Order Models for Profiled Steel Diaphragm Panels." *Proceeding of Wei-Wen Yu International Specialty Conference on Cold-Formed Steel Structures.* Baltimore, Maryland.

Bian, G., and Schafer, B.W. (2017). "Shell Finite Element Modeling of Elastic Shear Stiffness of Bare Steel Deck Diaphragm." *SDII Research Report*, *RR01*.

Guanbo Bian

May 2017

Advisor: Dr. Benjamin Schafer

Reader: Dr. Jamie Guest, Dr. Judith Mitrani-Reiser

ACKNOWLEDGEMENT

I would like to thank my Ph.D. advisor - Professor Ben Schafer for his supervision of my Ph.D. research. Without him 'adopting' me at the beginning of my study in the U.S., I would not have the chance to write this thesis for a Ph.D. degree. He was always supportive and allowed me the freedom to pursue my interests in the past five years: taking interesting courses, getting an extra Master's degree, taking my project in my own direction, etc. When I was stuck in my research, I never needed to worry about it – Dr. Schafer could always find a way to overcome the wall in front of us and make a clear path to proceed. He trained me to be a professional engineer. This is a process that will benefit me in my future career path. Other than in research and academics, he is also a role model for me in life - his attitude, dedication, work life balance will always inspire me in my future.

I would like to thank Prof. Spall in Applied Math and Statistics Department. He was very kind to advise me, a student from outside the field, on my research and helped me to understand a structural engineering problem from a mathematical point of view. He was a phenomenon teacher. I gained the foundation in statistics from his Monte Carlo Method course.

I would like to thank my thesis committee members Professors Guest and Mitrani-Reiser. Professor Guest helped me at the beginning of my Ph.D. and gave me many helpful

suggestions. Professor Mitrani-Reiser helped me with my oral exam, and gave me insightful advice on my research project, job searching and teaching practice.

I would like to thank many professors for their invaluable contributions to my research work. The idea of fastener-based shear wall model is from Professor Steve Buonopane. Prof. Buonopane generously shared his idea and code with me, and discussed with me very patiently countless times about my work. He also reviewed most of my papers on shear wall and always gave me very helpful comments. Dr. Shahab Torabian shared many of his ideas with me on cold-formed steel research, and helped me on torsion and diaphragm research work. Dr. Cris Moen and Dr. Sanjay Arwade gave me much helpful input on how to interpret shear wall simulation results and making meaningful plots in the shear wall reliability research. Without their help my Ph.D. research would not have gone so smoothly.

My great colleagues in Thin-Walled Structure group made my life full of happiness in the past five years. I am not sure my future colleagues will be as good as you guys, but for sure I will always remember the wonderful time we had in Latrobe 17. I would like to thank my colleagues: Astrid Fischer, Hamid Foroughi, Dave Fratamico, Fardad Haghpanah, Abdullah Mahmoud, and previous labmates: Dr. Deniz Ayhan, Dr. Jean Batista, Dr. Jiazhen Leng, Dr. Kara Peterman and Dr. Xi Zhao.

I would like to thank all friends and staff in the family of Civil Engineering Department. They gave me lots of help and fun times during my Ph.D.

I would like to thank my parents- they supported me constantly before and during my Ph.D. I also would like to thank my wife Yuxuan who always encouraged me when I faced challenges in the past few years. Lots of the work in this thesis was completed in her lab at nights and weekends. She also helped to proofread the draft of this thesis.

Table of Contents

List of Figures

List of Tables

CHAPTER 1

INTRODUCTION

1.1 Cold-Formed Steel Members and Systems

1.1.1 Cold-Formed Steel Members and Applications

Cold-formed steel members are widely used in many structural applications: buildings, storage racks, bridges, cars, aircraft, etc. Comparing to hot-rolled steel products, which are formed at elevated temperatures, the manufacturing of cold-formed steel products occurs at room temperature. The thicknesses for such cold-formed steel members usually range from about 0.10 mm to 7 mm. Some steel plates can be as thick as around 25 mm.

Building elements that can be framed with cold-formed steel include floors, roofs, walls, and other building parts. Both structural and non-structural assemblies can be framed with cold-formed steel. Cold-formed steel has many advantages over other material, including: light weight; fast and easy to fabricate and install; economy in transportation and handling; and very energy efficient. Figure 1-1 are typical cold-formed steel (CFS) buildings. Nowadays cold-formed steel framing buildings are used mostly as low to mid story buildings because of their member property, and the highest cold-formed steel buildings are ranged from eight to ten stories. The fire resistance of cold-formed steel buildings is often improved by its construction details.

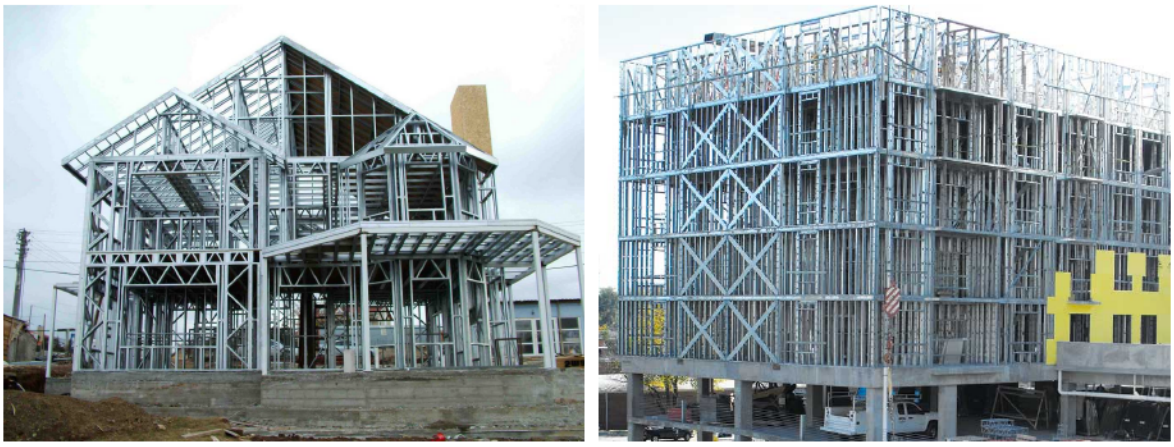

Figure 1-1. Typical cold-formed steel buildings ([8])

1.1.2 Torsion, Shear wall and Diaphragm in Cold-Formed Steel Structure

Since most common cross sections in cold-formed steel members are open, torsion is fundamental to the response of cold-formed steel members. For example, torsion is developed in cold-formed steel lipped channel beams (joists, purlins, girts, etc.) loaded away from their shear center. Torsion also plays a key role in buckling instabilities at the member level with lateral-torsional buckling of beams, and flexural-torsional buckling of columns; and at the cross-section level with (flange/web) distortional buckling. In cold-formed steel design the basic philosophy is to try to eliminate torsion to the greatest extent possible and little research has been done to examine torsion in isolation for cold-formed steel members.

The theory for the elastic torsional response of thin-walled open sections was developed by Vlasov, Timoshenko and other researchers, and remains the primary tool for design prediction methods. In this research basic aspects of torsion in cold-formed steel members is explored from a review of classical elastic response and a pilot set of

experiments at a single length. In addition, companion shell finite element models were developed that extend into the nonlinear geometric response and yielding.

Shear walls in cold-formed steel building are typically steel stud walls covered with structural sheathing material like plywood, oriented strand board or steel plate. Oriented strand board (OSB), which is made up of compressed cross-oriented layers of thin wooden strips together with wax and adhesives, is suitable for load-bearing applications in construction. Figure 1-2 is a typical wood sheathed, cold-formed steel shear wall. It includes three main parts: wood sheathing, cold-formed steel framing, and fasteners connecting the above two parts.

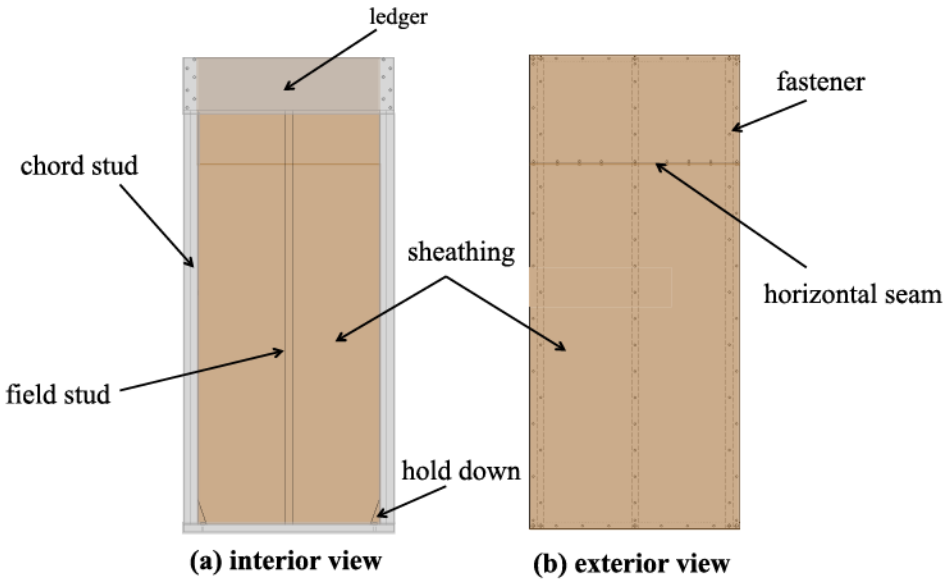

Figure 1-2 Sheathed, cold-formed steel framed shear wall

Shear wall strength is determined by the combined strengths of its three components: steel framing, sheathing and fasteners. As same as in other types of structures, light-framed shear wall transfers lateral loads through sheathing that is attached with fasteners to the framing members. Figure 1-3 shows cold-formed steel shear wall response under

lateral loading. The shear loads are transferred from the shear wall to the floor or foundation through the framing members while the induced overturning forces are transferred through the vertical studs to the ends of the wall through hold down.

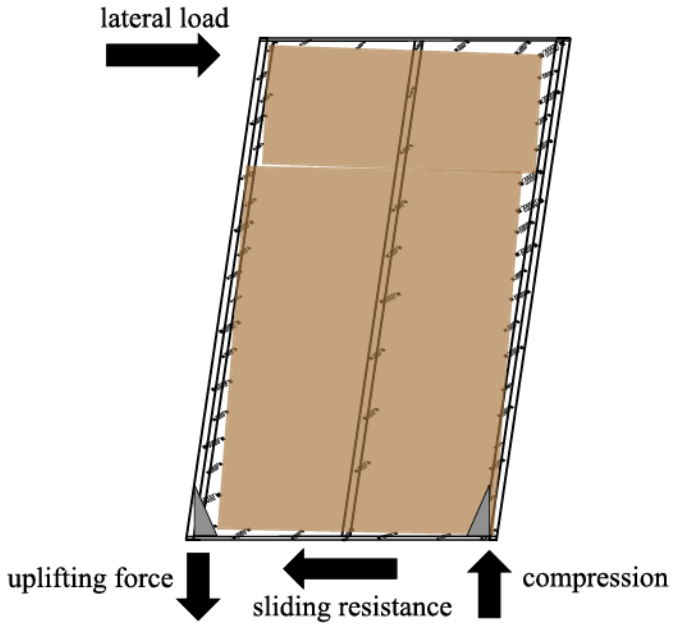

Figure 1-3 Cold-formed steel shear wall behavior and response

There are two types of defined CFS shear wall in AISI S400 (or AISI S213) design code: type I shear wall and type II shear wall. As shown in figure 1-4 (a), type I shear walls are fully sheathed with wood structural panels and hold-downs at each end. If Type I shear walls have openings, details need to be provided to account for force transfer through openings. Figure 1-4(b) shows a typical type II shear wall. Unlike in type I shear wall, the width of openings in in type II shear walls is not accounted and there is no detailing for force transfer.

A fastener-based shear wall model is developed for cold-formed steel shear wall system in this research work. This model can be used to predict the capacity of shear wall with

different configurations. Gravity wall modeling and reliability analysis is conducted on cold-formed steel shear wall based on this fastener-based model.

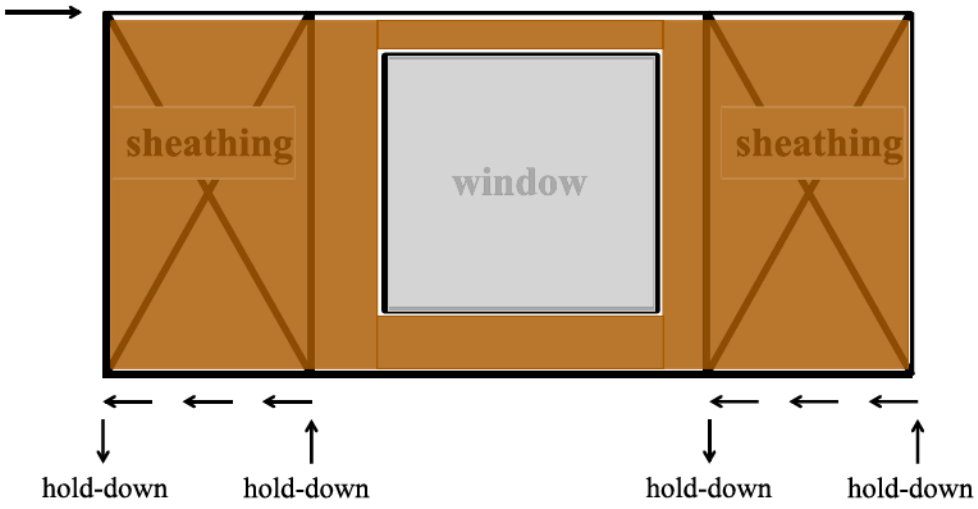

(a) Type I shear wall

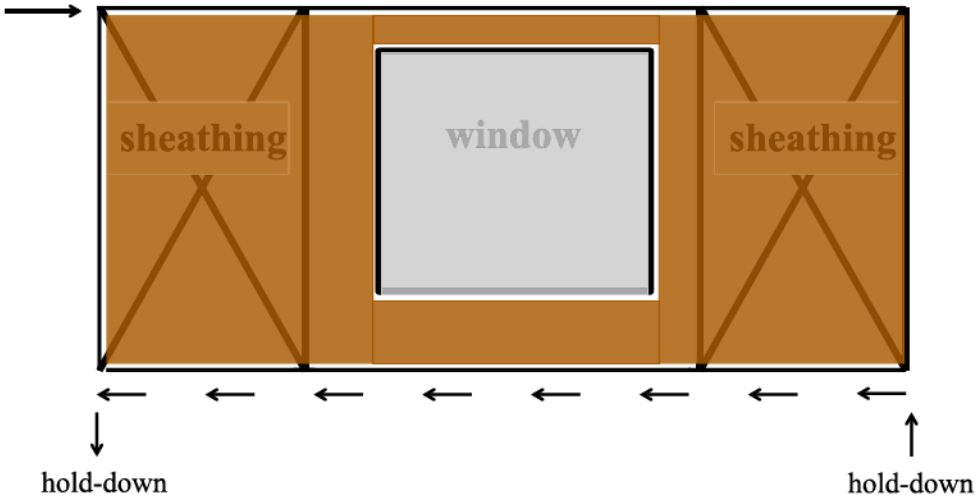

(b) Type II shear wall

Figure 1-4 Shear wall in cold-formed steel building

Profiled steel panels, i.e., metal deck, are roll-formed from thin steel sheet and can result in simple corrugated shapes or relatively complex longitudinal profiles with additional

transverse features such as embossments. These panels can serve as walls, floors or roof in many metal buildings, and form an integral component of common floor systems in a wide variety of buildings. When distributing lateral load this system acts as a diaphragm, with all elements in the system contributing: panel, panel inter-connections, joists, joist-to-panel connections, primary framing, and framing-to-panel connections. Under lateral loads the panels play a particularly important role as a distribution element, one in which the in-plane shear behavior of the panel is paramount. In the last two chapters of this dissertation, modeling work on bare steel deck is presented.

1.1.3 Codes and Standards

For cold formed steel member design, AISI S100 provides design details for members under axial loading, flexure, shear, and combined forces. In terms of lateral force resistance system design in cold-formed steel building, AISI S213-07 provides different shear wall capacities based on previous CFS shear wall tests. Components in CFS shear wall design should also follow AISI-S100 etc. for member (stud, ledger, etc.) design.

In 2016, new AISI cold-formed steel design specifications were released. Several different previous specifications are merged into two new specifications: North American Standard for Seismic Design of Cold-form Steel Structural Systems (AISI S400-15) and North American Standard for Cold-Formed Steel Structural Framing (AISI S240-15). Figure 1-5 illustrated what change happened and how they are merged to the new specifications.

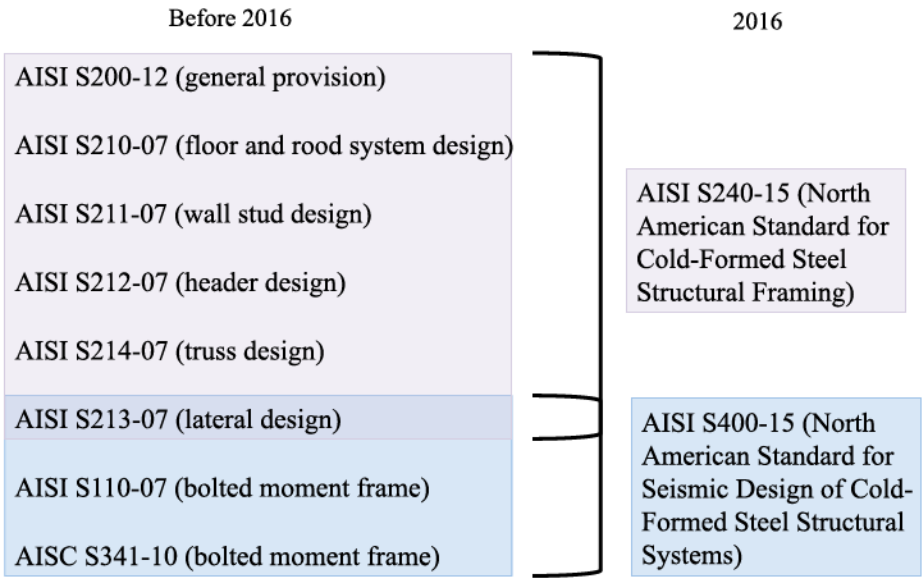

Figure 1-5 Update of AISI design specifications in 2016

1.2 Cold-formed Steel Modeling

For different cold-formed steel building members and systems, researchers can choose different materials and elements to model them. Figure 1-6 (a) and (b) illustrate typical cold-formed steel members and systems. In figure 1-6 (a), cold-formed steel members are often modeled using shell element and shear walls are modeled using shell element or simplified nonlinear truss element. In a metal building as shown in figure 6(b), bare steel deck diaphragm and roof are always modeled using shell element as well. In the following few sections, details on different modeling method are summarized.

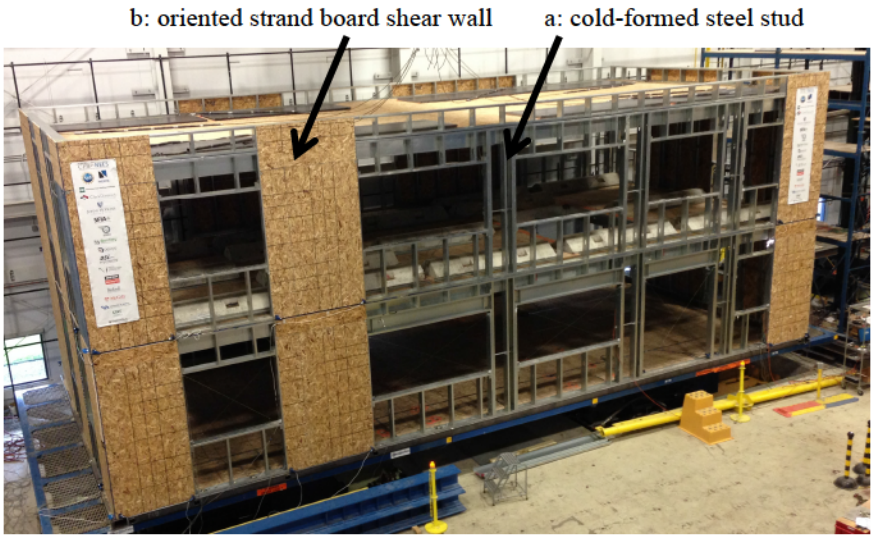

(a) CFS-NEES building ([8])

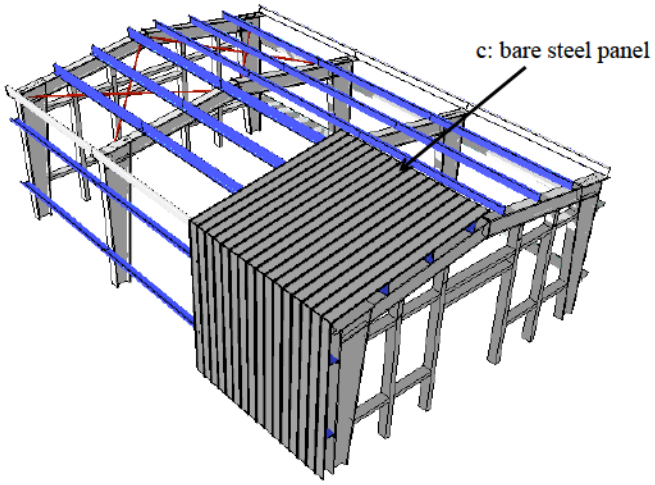

(b) Cold-formed steel metal building

Figure 1-6 Cold-formed steel members and systems

1.2.1 Shell Finite Element Models

To model cold-formed steel members, shell element is always a good option because of the geometric feature in thin-walled members: the dimension in transverse direction is much smaller than in other directions.

Schafer and Pekoz included imperfections and membrane residual stress in ABAQUS models for a compression flange to check the impact of different modeling assumptions. Schafer, Li and Moen performed a comprehensive study on computational modeling of CFS members for both buckling and collapse analysis. They compared elastic buckling analysis results between ABAQUS shell finite element models, finite strip method and classical solutions. In terms of collapse analysis, sensitivities of solvers, element type and discretization, boundary conditions, initial imperfections and residual stress are all considered in GMNIA analysis. In Foroughi et al 2014, they summarized current approaches and of thin metallic shell structural members and evaluated the existed GMNIA analysis tools.

1.2.2 Nonlinear CFS Shear Wall Models

Several different computational or analytical methods have been used to capture the non-linear behavior of CFS or wood-framed shear walls. One modeling approach is to use a single, complex spring element to represent each shear wall. This approach requires full-scale cyclic test data to calibrate the spring element properties, but allows for modeling of entire buildings. A second approach uses finite element models of CFS shear walls with non-linear shell and fastener elements. In such models the computational complexity typically precludes modeling of full buildings or a large number of different shear wall configurations.

For wood-framed shear walls, a fastener-based approach has been used to derive analytical expressions for key response parameters, such as lateral strength or total

displacement, a detailed discussion of which is provided in Chen. A fastener-based modeling approach for the full cyclic behavior of wood-framed shear walls has also been incorporated into the nail-pattern analysis module of the SAWS and SAPWood software, as well as into general-purpose finite-element software.

For CFS shear walls fastener-based analytical approaches to strength and displacement have also been developed. These analytical approaches only estimate peak strengths and deflections and do not attempt to capture the complete monotonic or cyclic load-displacement behavior. These analytical approaches also introduce some simplifying assumptions, such as rigid framing members with pin-connections or rigid hold-downs.

1.2.3 Bare Steel Deck Models

The notion of employing an equivalent orthotropic flat plate to simulate a corrugated plate has long been used in engineering. Typically, out-of-plane bending behavior is of primary interest as opposed to in-plane behavior and early work such as Easley and Mcfarland (1969) investigated equivalent flexural rigidities. More recently Samanta and Mukhopadhyay (1999) re-examined the problem and developed closed-form expressions for the orthotropic plate rigidities for both out-of-plane (flexure) and in-plane (extension and shear). This was followed by Xia et al. (2012), who expanded on the earlier work including correcting some assumptions, and derived a set of plate rigidities for equivalent orthotropic plates to model the elastic stiffness of a corrugated plate.

C.A. Rogers and R. Tremblay have conducted a several years research project on bare steel deck diaphragm. They developed linear elastic finite element (FE) models in

SAP2000 for the initial stages of the roof diaphragm in-plane shear behavior in their test. In the model, four-node flat shell element was selected capable of developing bending and membrane behavior. Link element was used to model the sidelap, deck-to-frame connections and contact surfaces. This shell FE model can reproduce the elastic load–deformation behavior of the diaphragm tests accurately.

1.3 References

[1] AISI-S213-07. North American standard for cold-formed steel framing—lateral design. Washington, D.C.: American Iron and Steel Institute; 2007.

[2] AISI-S400-16. North American standard for Seismic Design of Cold-Formed Steel Structural Systems. Washington, D.C.: American Iron and Steel Institute; 2016.

[3] AISI-S100-16. North American Specification for the Design of Cold-Formed Steel Structural Members. Washington, D.C.: American Iron and Steel Institute; 2016.

[4] AISI-S200-12. North American Standard for Cold-Formed Steel Framing - General Provisions. Washington (DC): American Iron and Steel Institute; 2012.

[5] Vlasov VZ. Thin-walled Elastic Beams. Jerusalem Israel Program for Scientific Translations; 1961.

[6] Timoshenko SP, Gere JM. Theory of Elastic Stability. McGraw-Hill; 1961.

[7] Don Allen, Robert Wills. (2017). Specifying cold-formed steel to meet project goals. The Construction Specifier, 2017.

[8] Schafer, B. W., D. Ayhan, J. Leng, P. Liu, D. Padilla-Llano, K. D. Peterman, M. Stehman et al. (2016). Seismic Response and Engineering of Cold-formed Steel Framed Buildings." In Structures, vol. 8, pp. 197-212.

[9] Schafer, B. W., & Peköz, T. (1998). Computational modeling of cold-formed steel: characterizing geometric imperfections and residual stresses. Journal of Constructional Steel Research, 47(3), 193-210.

[10] Schafer, B. W., Li, Z., & Moen, C. D. (2010). Computational modeling of cold-formed steel. Thin-Walled Structures, 48(10), 752-762.

[11] Foroughi H., Moen C.D., Myers A.T., Tootkaboni M., Vieira L. and Schafer B.W. (2014), “Analysis and Design of Thin Metallic Shell Structural Members - Current Practice and Future Research Needs”, Proceedings of Structural Stability Research Council Annual Stability Conference, Toronto, Canada, March 25-28, 2014

[12] Steel Deck Institute. Diaphragm Design Manual, fourth edition, 2015.

[13] Leng J, Schafer BW, Buonopane, SG. (2013). Modeling the seismic response of cold-formed steel framed buildings: model development for the CFS-NEES building. Proceedings of the Annual Stability Conference, SSRC 2013; [St. Louis, MO USA].

[14] Fülöp LA, Dubina D. (2004). Performance of wall-stud cold-formed shear panels under monotonic and cyclic loading. Part II: Numerical modelling and performance analysis. Thin-Walled Struct 2004; 42: 339-49.

[15] Martínez-Martínez J, Xu L. (2011). Simplified nonlinear finite element analysis of buildings with CFS shear wall panels. J Constr Steel Research 2011; 67(4): 565-75.

[16] Xuhong Z, Yu S, Tianhua Z, Yongjian L, Jin D. (2006). Study on shear resistance of cold-formed steel stud walls in residential structure. Advances in Engineering Structures, Mechanics & Construction 2006; 423-35 [Waterloo, Ontario, Canada].

[17] Chen CY. (2004). Testing and performance of steel frame/wood panel shear walls. Department of Civil Engineering and Applied Mechanics, McGill University, Montreal, Canada; 2004.

[18] Folz B, Filiatrault A. (2004). Seismic analysis of woodframe structures. I: model formulation. II: model implementation and verification. Journal of Structural Engineering 2004; 130(9): 1353-70.

[19] Pei S, van de Lindt, JW. (2010). SAPWood for Windows seismic analysis package for woodframe structures, version 2.0. Colorado State Univ; 2010. https://nees.org/resources/818.

[20] Fiorino L, Della Corte L, Landolfo R. (2006). Lateral response of sheathed cold-formed shear walls: an analytical approach. Eighteenth International Specialty Conference on Cold-Formed Steel Structures 2006; 603-19 [Orlando, FL, USA].

[21] Xu L, Martínez J. (2006). Strength and stiffness determination of shear wall panels in cold-formed steel framing. Thin-Walled Struct 2006; 44: 1084-95.

[22] Mastrogiuseppe, S., Rogers, C. A., Tremblay, R., & Nedisan, C. D. (2008). Influence of nonstructural components on roof diaphragm stiffness and fundamental periods of single-storey steel buildings. Journal of Constructional Steel Research, 64(2), 214-227.

CHAPTER 2

TORSION OF COLD-FORMED STEEL LIPPED CHANNELS DOMINATED BY WARPING RESPONSE

2.1 Abstract

The objective of this chapter is to provide benchmark test results, explanatory shell finite element models, and preliminary Direct Strength Method prediction for cold-formed steel lipped channels undergoing torsion dominated by warping response. Although the elastic theory for the torsional response of a thin-walled cold-formed steel lipped channel member is well-developed, the extent to which warping torsion dominates the response of cold-formed steel members is not widely appreciated. Further, for cold-formed steel members in torsion little exists in terms of experimental benchmarks and even less on situations beyond the classic elastic theory, including geometric nonlinearity and post-buckling, and/or material nonlinearity from partial to full plastification of the section. Here, a typical cold-formed steel lipped channel member loaded experimentally in torsion exhibits significant strength beyond first yield. Shell finite element models of the testing correlate well with the experiments and indicate the extent of plastification as the thin-walled member undergoes torsion dominated by warping response. Idealized end boundary conditions are developed for the shell finite element model that is conservative with respect to the response, and in agreement with classical expressions in the elastic regime. The shell finite element model with idealized end boundary conditions is used to develop a parametric study on ultimate torsional capacity for members dominated by

warping torsion. The results indicate that torsional slenderness may be used to predict torsional capacity and indicate that Direct Strength Method predictions for torsion for members dominated by warping torsion are possible. Preliminary design expressions for warping torsion strength prediction are provided.

2.2 Introduction

Torsion is fundamental to the response of cold-formed steel members since common sections are open, with relatively weak torsional resistance, and often singly- or un-symmetric. For thin-walled cold-formed steel members torsion manifests itself in direct form or through instability. For example, cold-formed steel lipped channel beams (joists, purlins, girts, etc.) loaded away from their shear center develop torsion. Torsion also plays a key role in buckling instabilities at the member level with lateral-torsional buckling of beams, and flexural-torsional buckling of columns; and at the cross-section level with (flange/web) distortional buckling. The theory for the elastic torsional response of thin-walled open sections was developed by Vlasov [1] and utilized by Timoshenko [2] and others, and remains the primary tool for design prediction methods (see [3], [4] and [5]).

In the classical theory [3,4] torsion (T) is resisted by shear (T_{sv}) and by shear related to restrained warping (T_w):

$$T = T_{sv} + T_w = GJ\theta' - EC_w\theta''' \tag{2-1}$$

where, G is the shear modulus, J is the St. Venant torsional constant, E is the elastic modulus, C_w is the warping torsion constant, and θ is the angle of twist (and ' denotes derivatives). For thin-walled cold-formed steel sections, as discussed further in the next section, the shear contribution (T_{sv}) and related shear stresses (τ_t) are relatively small and the dominant resistance develops from warping restraint (e.g., see [6]). Warping restraint creates longitudinal (σ_w) and shear stresses (τ_w) in the cross-section. The longitudinal stresses, which are the primary contributor to instability and degraded strength in thin-walled members, may be determined from:

$$\sigma_w = E\omega\theta'' = B\omega / C_w \tag{2-2}$$

where ω is the sectorial coordinates, and B is the bimoment. Warping stress σ_w may be found directly through differentiation of the twist ([3], [4], and [5]), or through B, which develops in the section as it responds to torsion, T, and is available from numerical beam finite element solutions (e.g. MASTAN [7], [8]). The shear stresses due to warping vary around the cross-section according to:

$$\tau_w = -\frac{ES_w\theta'''}{t} \tag{2-3}$$

where S_w is the warping static moment, and t is the thickness of the member. The shear stresses due to St. Venant torsion vary through the thickness, per:

$$\tau_t = Gt\theta' \tag{2-4}$$

Research on cold-formed steel beams in torsion demonstrated the detrimental role of the torsional response on bending strength and the importance of including this response in design [9]. Analysis demonstrates that the torsional warping stresses change significantly as the beam twists and are highly sensitive to the end boundary conditions [10]. Exploration of the stability of the section further indicates that cross-section buckling is also sensitive to the longitudinal warping stresses that develop in the twisted section [10]. For the common case of a cold-formed steel beam with restraint on one flange the torsional stresses that develop are even more complex, but their correct inclusion can aid design ([11], [12], and [13]). Research provides significant insight on torsional response of cold-formed steel members, but less has been done to examine torsion in isolation for cold-formed steel members – the approach that has long been used to understand axial, bending, and shear actions.

In cold-formed steel design the basic philosophy is to try to eliminate torsion to the greatest extent possible. For example, AISI-S100 [5] provides prescriptive bracing criteria to limit torsion in beams. When torsion must be considered, design directly or indirectly applies stress-based interaction expressions to limit the impact of torsion. Eurocode [14] limits the total longitudinal stress from all actions, including torsion, to be less than the yield stress, F_y (divided by a partial safety factor). AISI-S100 [5] employs a reduction factor, R, on bending strength to account for bending-torsion interaction, where

R is the ratio of the maximum bending stress to the combined bending (σ_b) plus warping stress (σ_w), i.e.:

$$R = \frac{(\sigma_w)_{\max}}{|\sigma_b + \sigma_w|} \leq 1.0 \tag{2-5}$$

The resulting reduction, which is applied to the bending capacity calculated without consideration of torsion, provides a reduction similar to a longitudinal stress-based linear interaction equation. The dominance of a stress-based approach to account for a limit state (torsion) is unusual in modern design where strength-based limit states are used for all other actions.

The approach taken in this chapter is to explore basic aspects of torsion in cold-formed steel members first from a review of classical elastic response, then from a pilot set of experiments at a single length, and finally from companion shell finite element models that extend into the nonlinear geometric response and yielding. Torsional response in buckling, initial yielding, and full plastification are all explored. Ultimately, the goal is to provide strength-based expressions for the prediction of torsional limit states, when warping torsion dominates the response, that can be integrated into design through appropriate interaction equations.

2.3 Classical Elastic Torsional Response in Cold-Formed Steel Members

While it is generally understood that thin-walled open members, such as those used in cold-formed steel applications, rely on warping to restrain torsion the extent to which this is true and the conditions under which this is true are less well understood. Distribution of

torsion between T_w and T_{sv} is dependent on cross-section properties, boundary conditions, and the member length.

To illustrate, consider the torsional response of a 400S162-54 [345 MPa (50 ksi)] cold-formed steel member (nomenclature per AISI-S200 [15]). Two cases with midspan torsion applied, as illustrated in Figure 2-1 are considered: torsionally supported – warping-free (i.e. the ideal fork type boundary conditions), and torsionally supported – warping-fixed. The members are modeled in MASTAN [8] and the results post-processed in terms of the warping torsion (T_w) diagram and provided in Figure 2-2 for a series of different *L/H* ratios, where L is the member length and H is the cross section depth (i.e. 100mm (4 in.)). The L/H ratio is varied between 2, consistent with a well-braced framing member, to 20 a large torsionally-unbraced span. The response, provided in Figure 2-2b, indicates that at the midspan and at the fixed end of a warping-fixed beam T_w dominates response. In a warping-fixed beam T_w is a minimum at the ¼ points, but even for *L/H* as high as 20, T_w still dominates response (Figure 2-2b). For a beam with warping continuity, but warping-free at its ends, T_w is a minimum at the ends, as shown in Figure 2-2a. In this case, T_w is still as much as 80% of the total torsion, but T_{sv} plays an important role.

The selected member cross-section dimensions influence the results and this may be captured by considering the non-dimensional variable $\alpha = EC_w/(GJL^2)$ as a means to classify the section. For our typical 400S162-54 cold-formed steel section with *L/H*=6, α = 5.34. Figure 2-3 provides the warping torsion diagram response for α from 1 to as small

as 0.01. Here one can see that in sections that have relatively large J in comparison with C_w the dominance of warping torsion response is decreased.

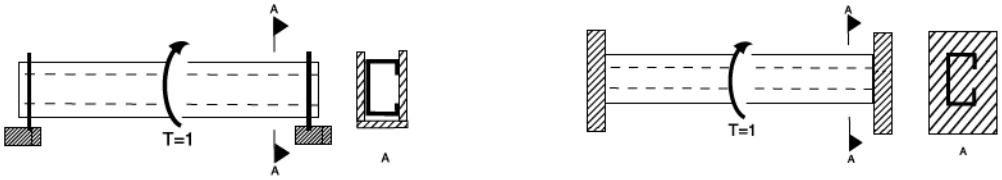

(a) (b)

Figure 2-1. Beam with mid-span torsion load: (a) torsionally supported – warping-free and (b) torsionally supported – warping-fixed

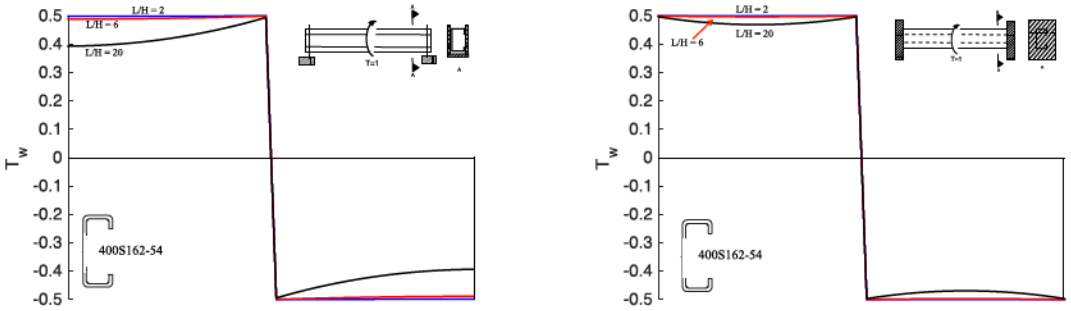

(a) (b)

Figure 2-2. Diagram of restrained torsion along member length for 400S162-54 for different member lengths (a) torsionally supported – warping-free and (b) torsionally supported – warping-fixed

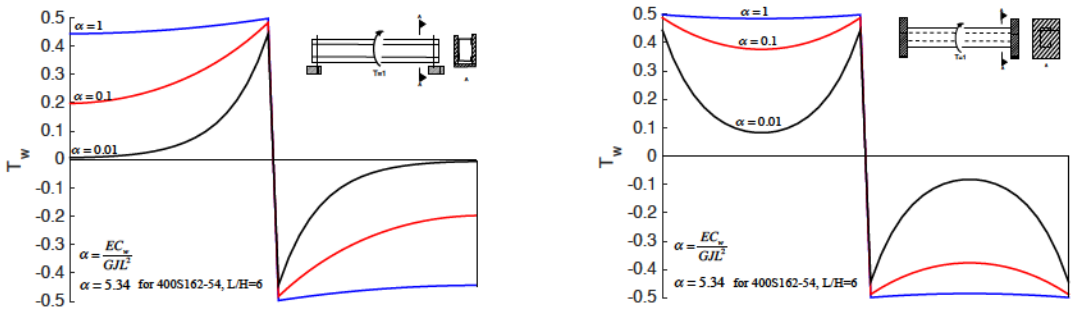

(a) (b)

Figure 2-3. Diagram of restrained torsion along member length for different α: (a) torsionally supported – warping-free and (b) torsionally supported – warping-fixed

Systematic study of the ratio of warping torsion (T_w) to the total torsion ($T_w + T_{sv}$) across a broad range of cross-sections (α's) at three key locations: midspan in the warping-fixed case, ¼ span in the warping-fixed case, and at the member ends in the warping-free case are provided in Figure 2-4. Histograms of the α at *L/H* of 2 and 20 for all commercially available structural cold-formed steel lipped channel members in North America [15] are also provided in Figure 2-4. (For *L/H* of 2 and 20 the 400S162-54 of Figures 2-2 a and b has an α of 48 and 0.48, respectively.) Figure 2-4 indicates that for the vast majority of cold-formed steel members and boundary conditions T_w dominates the elastic response. Only for warping-free members with long unbraced lengths (high *L/H*) does T_{sv} play a significant role.

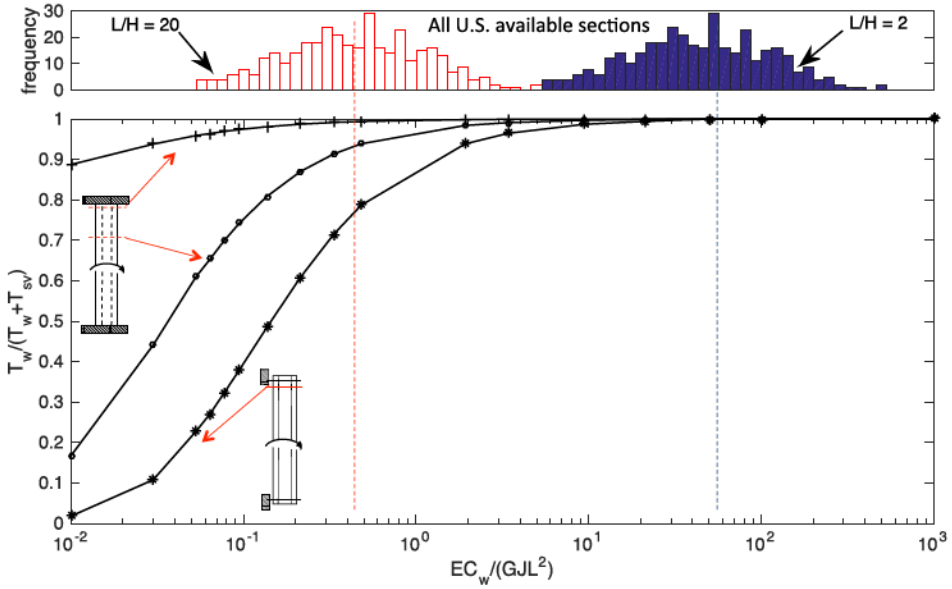

Figure 2-4. Ratio of restrained torsion to total torsion for warping-free and warping-fixed boundary conditions across different member properties

The stresses developed in a cold-formed steel cross-section due to torsion include σ_w, τ_w, and τ_t, as introduced in Eq. 2-4. The distribution of each of these stresses for a typical cold-formed steel section is depicted in Figure 2-5. The extent to which the stresses of Figure 2-5 are realized is dependent on how the torsion is distributed between T_w and T_{sv}, and the derivatives of the twist as related to bimoment in Eq. 2-2.

The impact of the developed stresses may be understood in terms of the von Mises stress, which is commonly associated with prediction of steel yielding in multi-axial stress states, and in this case simplifies to:

$$\sigma_{eff} = \sqrt{\sigma_w^2 + 3\left(\tau_w^2 + \tau_t^2\right)} \tag{2-6}$$

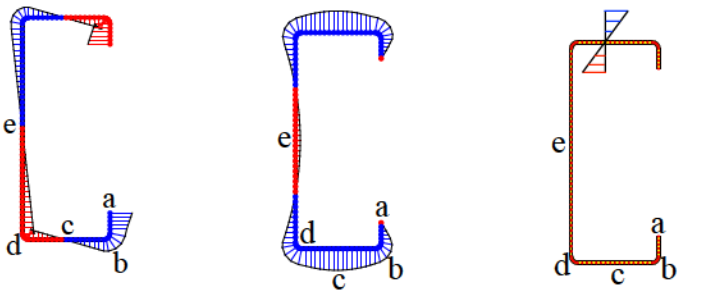

	$B = 3.44\text{N}\cdot\text{m}^2$	$T_w = 5.56\text{N}\cdot\text{m}$	$T_{sv} = 0.13\text{N}\cdot\text{m}$
	σ_w (MPa)	τ_w (MPa)	τ_t (MPa)
a	-1.00	0.00	1.00
b	-0.52	-0.67	1.00
c	-0.00	-1.00	1.00
d	0.47	-0.77	1.00
e	0.00	0.22	1.00

Figure 2-5. Stress analysis of 400S162-54 under torsion (a) warping longitudinal stress (b) warping shear stress (c) pure shear stress (note: B=3.44N-m2 is equivalent to a mid-span T of 1.15 N-m in the 400S162-54 with L of 0.61 m.)

The maximum warping stress (σ_w) in the cross section is compared to the von Mises stress (σ_{eff}) along the member for the 400S162-54 at L/H= 6 for the studied torsion cases in Figure 2-6. For warping-fixed end conditions, σ_w is a reasonable estimate of σ_{eff} except near the ¼ point, where stress is low. Even for warping-free end conditions, only at the member ends, where σ_{eff} is attributable to τ_w and τ_t alone is their significant error – generally σ_{eff} is dominated by σ_w and specifically this holds true at maximum stress locations.

For cold-formed steel sections warping torsion is more likely to dominate response than St. Venant torsion. However, the elastic stresses developed in the classical theory are based on the undeformed cross-section, and provide no insight on what happens after yielding.

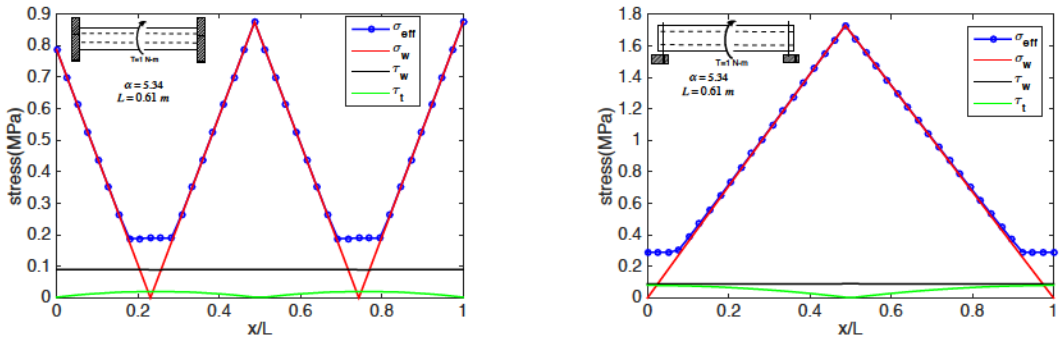

(a) (b)

Figure 2-6. Cross-sectional maximum stress distribution along the member under torsion: (a) warping-fixed boundary condition and (b) warping-free boundary condition

2.4 Pilot Experiments in Torsion

A small experimental pilot study was conducted to explore torsion on the behavior of cold-formed steel lipped channels dominated by warping torsion, and loaded past initial yield. The tests employed an MTS tension-torsion rig with hydraulic grips. The specimens consisted of cold-formed steel lipped channel sections with welded end plates and a circular shaft inserted into the grips as shown in Figure 2-7. Specimens were held constant in the axial direction and twisted to approximately 45 degrees with actuator torsional moment and angle of twist recorded. The bottom grip, per Figure 2-7, applied the twist to the specimen while the top remained fixed.

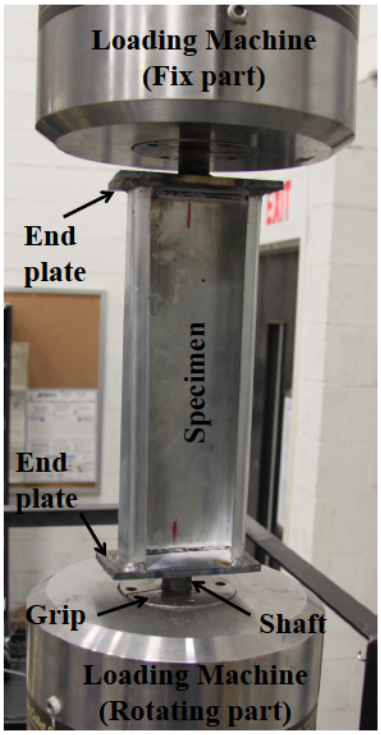

Figure 2-7. Torsion testing of cold-formed steel lipped channel: untwisted specimen in rig

2.4.1 Test Specimen and Loading Protocol

The specimens were cut from a single 6.7 m long punched 400S162-54 [50 ksi] stud (nomenclature per AISI-S200 [15]). This cross section was chosen based upon material availability, but represents a common depth, 102 mm (4 in.), thickness, 1.37 mm (0.054 in.), and grade 345 MPa (50 ksi), for load-bearing wall studs in cold-formed steel light frame construction. A tensile coupon was taken from the web of the stud and testing conducted per ASTM [16] with the result provided in Figure 2-8, the measured yield stress is 373 MPa (54 ksi) per the 2% offset method.

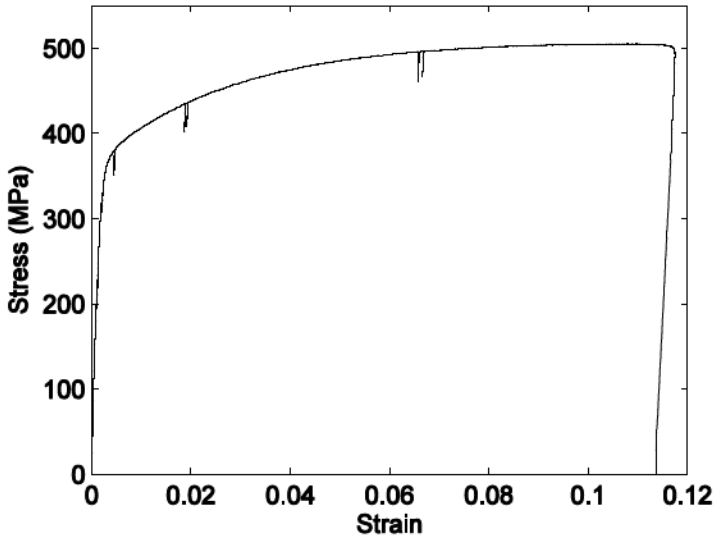

Figure 2-8. Experimental tensile stress-strain relationship for coupon cut from 400S162-54 [50 ksi]

As detailed in Figure 2-9 the typical 304.8 mm (12 in.) long specimens, had steel end plates, 6.4 mm (0.25 in.) or 25.4 mm (1 in.) thick, welded to the ends. In addition, to connect to the grips of the torsion rig, 25.4 mm (1 in.) diameter steel shafts were welded to the end plates. The shafts were aligned with the cross-section centroid. Based on as-built measurements, error in this alignment was within 2.5% of ideal.

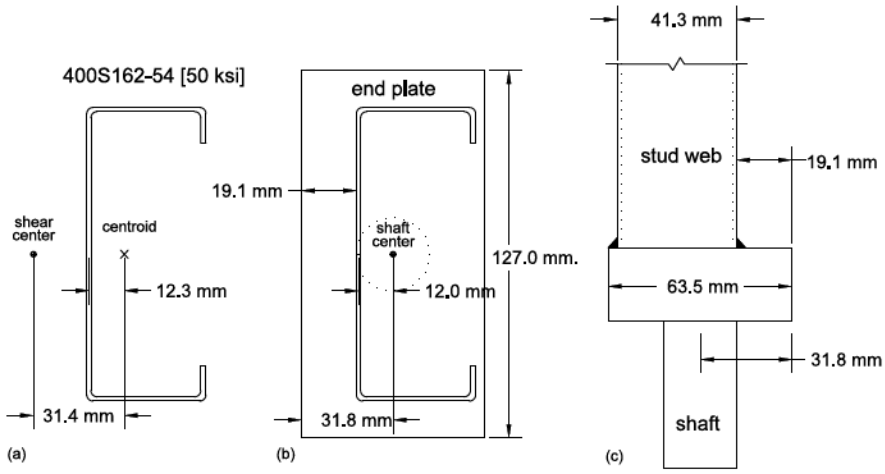

Figure 2-9. Typical test specimen, plan view showing (a) basic designation, and (b) size and location of end plates and (c) elevation view of stud, end plate, and shaft

Specimens were monotonically loaded to a twist of 45 degrees at a rate of 0.025 degrees per second. Once a 45-degree twist was achieved, the specimen was unloaded at a rate of 0.75 degrees per second. Basic test parameters are summarized in Table 2-1. Tests b-d, identical save for the load rate in test c, establish a core set of results for torsional response of a section with approximately rigid end conditions.

Table 2-1. Test details and basic response for torsion tests

ID[1]	Length (mm)	End Plate (mm)	T_u (kN-m)	$\theta@T_u$ (deg.)
a	304.8	6.4	0.63[4]	45.0[3]
b	304.8	25.4	0.62	34.0
c[2]	304.8	25.4	0.64	31.6
d	304.8	25.4	0.70	29.2

1. 400S162-54 [50 ksi] stud, nomenclature per [16, 18].
2. Loaded at faster rate: see [17] for detail.
3. Maximum rotation tested = 45 degrees.

2.4.2 Experimental Result

Results for the experimental testing are shown in Figure 2-10, and the moment at maximum torsion and its corresponding rotation are provided in Table 2-1. All of the specimens are able to undergo large twist rotations (at least ~ 30 deg.) prior to reaching their peak torsional moment. The specimens with thicker (25.4 mm [1 in.]) end plates (b, c, d) had stiffer response than that with thinner (6.4mm [0.25 in.]) end plates. Nominally identical specimens (b, c, and d) share a common elastic stiffness, similar rotations at failure, but modestly different peak torsional moments. Observed failure modes for representative specimens are provided in Figure 2-11. The specimen with a thin end plate (6.4 mm [0.25 in.]) experienced significant end plate deformations as a result of warping deformations generated by the specimen in torsion (Figure 2-11(a)). The warping boundary condition for the thin end plate is semi-rigid. Specimens with 25.4 mm (1 in.)

end plates experienced inelastic lip local buckling past yield (Figure 2-11(b) and ultimately, failed in the weld between the channel and the end plate (Figure 2-11(c)). This is considered indicative of a warping-fixed end boundary condition. The tested specimens were all of a relatively short length and dominated by warping response.

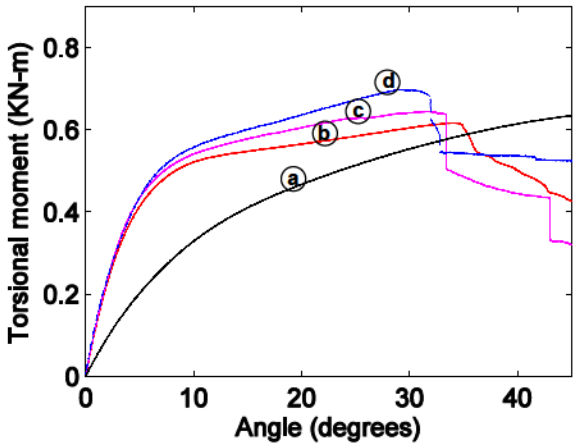

Figure 2-10. Load-displacement of test results

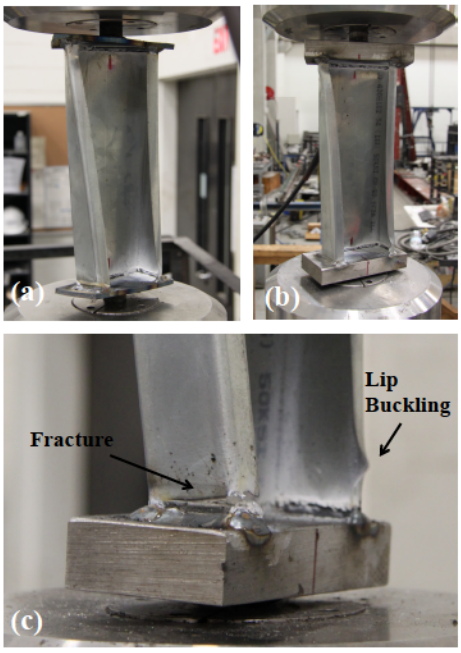

Figure 2-11. Observed deformations and failure (a) test a, significant distortions in end plates, (b) test b, inelastic lip local buckling, (c) test c, inelastic lip local buckling followed by fracture along the opposing weld

2.5 Shell Finite Element Model of Experiments

Shell finite element models motivated from the tests were developed and conducted in ABAQUS [19] to further evaluate the test results and provide an estimation of the internal stresses developed under torsion. Specifically, this section provides the basic model characteristics, comparison with the conducted experiments, and the spread of plasticity through the section under twist.

2.5.1 Model Characteristics

To model the cold-formed steel stud the ABAQUS S4R shell element was used. When applicable the end plate and shaft were modeled with the C3D8R solid element. Typical finite element meshes are shown in Figure 2-15.b.

End boundary conditions play a particularly important role in the response, and three distinct models are explored in this regard: (i) test model, essentially true to the testing apparatus; (ii) fully fixed model, providing an idealized upper-bound response; and (iii) idealized warping-fixed model, creating conditions consistent with classical warping torsion theory. As depicted in Figure 2-12, in the test model, Figure 2-12(a), both the end plate and loading shaft are added to the stud. For the fully fixed model, Figure 2-12(b), one end of the stud is coupled to a reference point with all six degrees of freedom fixed, while the other end of the stud is coupled to a reference point with five degrees of freedom fixed (only the torsion/twist degree of freedom where the twist action is applied is free). For the idealized warping-fixed model, as shown in Figure 2-12(c), the ends of the stud are tied to a reference point at the centroid, but only torsional moment is allowed to develop all other forces/reaction are released (this is accomplished by allowing

longitudinal deformations associated with axial deformation and major- and minor-axis movements, but not torsion warping deformations). The idealized warping-fixed model is the subject of Section 5, while the test and fully fixed model are compared with the experiments in this section.

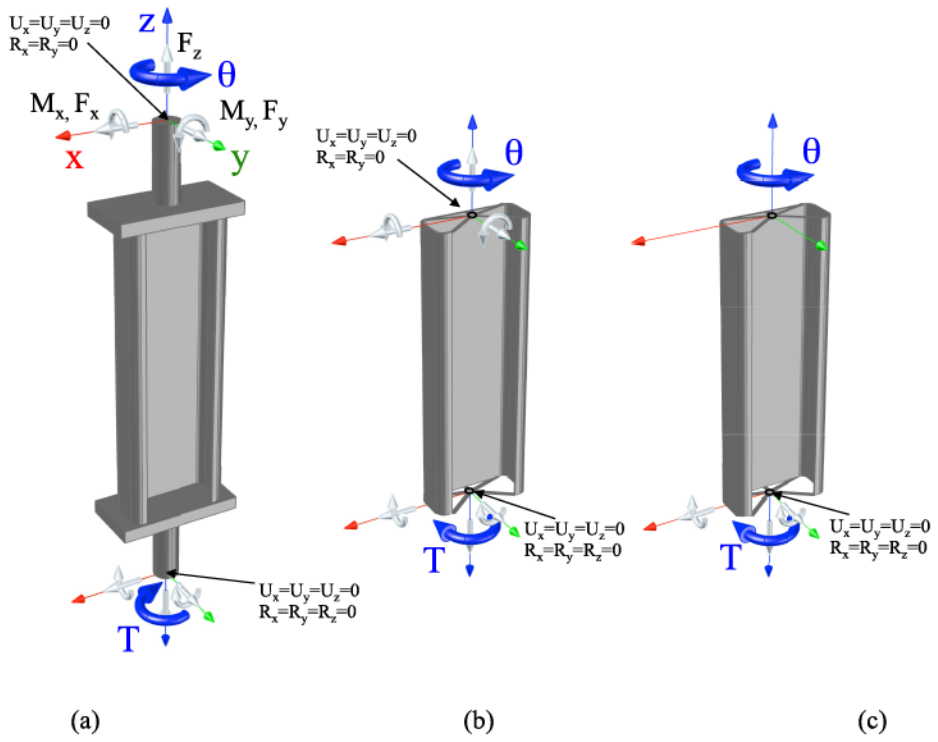

Figure 2-12. Typical FE model and depiction of end boundary conditions for: (a) tested stud; (b) fully fixed; (c) idealized warping-fixed using multi-point coupling to the centroid and releasing all actions except torsion

Material nonlinearity was accounted for using classical metal plasticity theory based on von Mises yield criterion and isotropic hardening. For direct comparison with the tests, the measured, engineering stress and strain values as given in Figure 2-8 were employed. For implementation in ABAQUS the engineering values were converted to true stress and strain.

Imperfections and residual stresses were not considered in the models. Initial geometric imperfections play a modestly reduced role in the response of the tested specimens due to the large rotations (>10 degrees) that exist prior to local buckling initiation. Residual stresses, both from forming and welding, deserve future study. The model does not consider fracture.

Two variations on the tested specimens were examined to understand model sensitivity: (i) offset in the loading shaft, and (ii) torsional stiffness of the loading shaft. To understand the impact/sensitivity to errors when welding the loading shaft to the end plate a +/- 6.4 mm offset was considered. To vary the stiffness of the loading shaft its diameter was varied from 12.7 mm (1/2 the tested diameter, or $1/16^{th}$ the actual J) to 63.5 mm (2.5 times the tested diameter, or 39 times the actual J).

2.5.2 Comparison with Experiments

The torsion-twist response of the developed finite element models are compared with the tests with the thick end plate (25.4 mm, Test a) and the thin end plate (6.4 mm Test c) in Figure 2-13. The "fully-fixed" model is unrealistically stiff and strong indicating the end plate and loading shaft (though stiff) contribute meaningfully to the as-measured response. The "test model" with the end plate and loading shaft explicitly modeled gives results that are most comparable to the testing prior to fracture (< 30 degrees for the thick end plate, and < 40 degrees for the thin end plate).

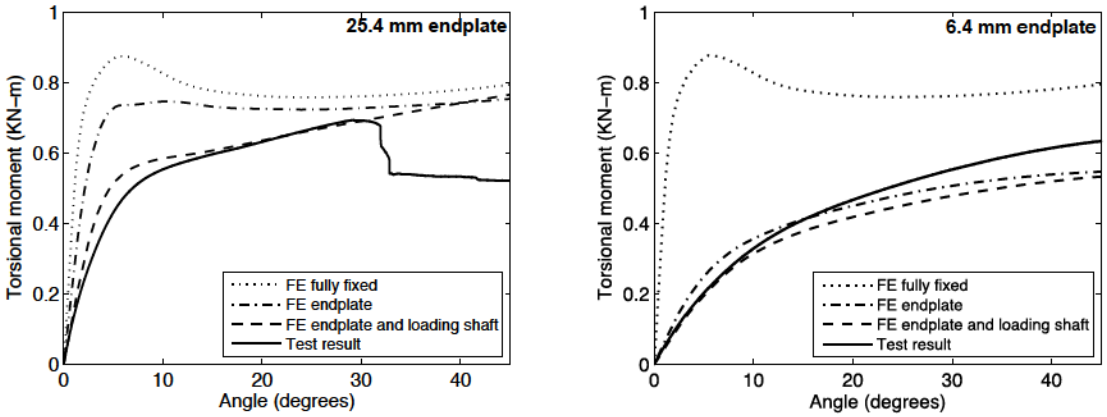

(a) (b)

Figure 2-13. Torsional moment-angle relationship for:(a) 25.4 mm endplate model (b) 6.4 mm endplate model

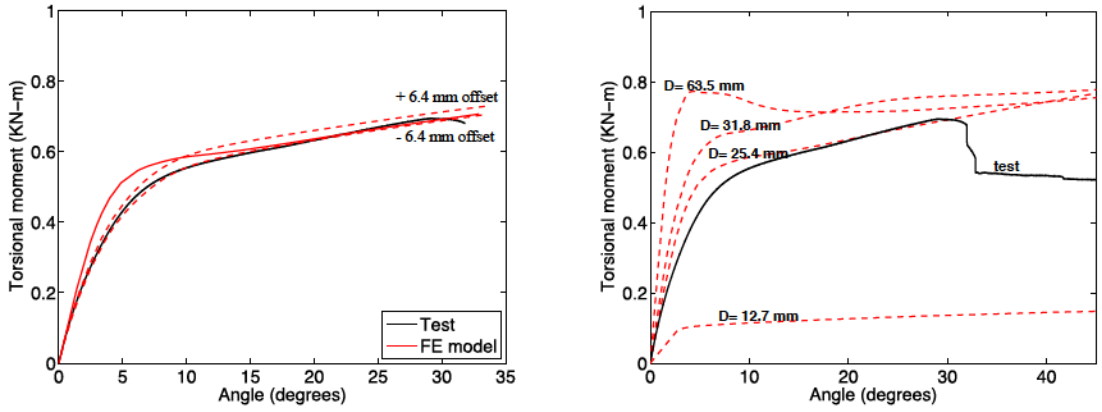

(a) (b)

Figure 2-14. Loading shaft effect on FE result: (a) offset effect; (b) diameter effect

The impact of shaft offset and torsional rigidity is provided in Figure 2-14 (a) and (b) respectively in comparison with Test 6. Including a small shaft offset increases the accuracy of the initial stiffness prediction, and provides a small measure of scatter in the torsional moment. In effect the offset is a useful, small imperfection in the model. The studied shaft diameters provide a variation in shaft torsional rigidity (J) from 0.0625 to 39 times the actual shaft J. The response thus ranges from nearly fully dominated by shaft

twist to the fully fixed case, as shown in Figure 2-14(b). One must take care with using the shaft diameter as a simple end torsional rigidity proxy since the model uses solid elements for the shaft and thus influence the end plate rigidity.

2.5.3 Characterization of Cross-Section Yielding and Plasticity

The torsion-twist response is initially elastic, but large deformations and yielding lead to a softening in the response. It is common in design to use elastic stress predictions and first yield criterion for torsion, here we explore the extent of observed yielding in the modeled section under twist to determine the limits of these common approaches. Consider the torque at which first yield occurs: in the developed shell finite element model one can determine the first integration point in an element in the stud in which the von Mises stress $\max(\sigma_{eff}) = F_y$. The shell finite element model includes the full three-dimensional state of stress resulting from warping, shear, and even local plate bending and end effects developed in response to torsion. In the model first yield occurs at the end cross section due to warping restraint at the ends.

To examine yielding, consider the torsion-plastic strain response for the "test model" and "fully fixed" model as provided in Figure 2-15. For comparison, $\max(|\sigma_w|) = F_y = 373$ MPa at $T = T_w = 0.2$ kN-m by classical theory. The end conditions have a clear impact on the observed torsional moment and plastic strain. However, for all cases the torsional moment, even for a small limiting peak plastic strain of e.g. 1%, is nearly double the torsional moment at which yielding initiates in the model. Significant torsional inelastic reserve is observed. Figure 2-15(b) provides a prediction of the developed plastic strain and deformed shape, deep into the inelastic reserve in torsion.

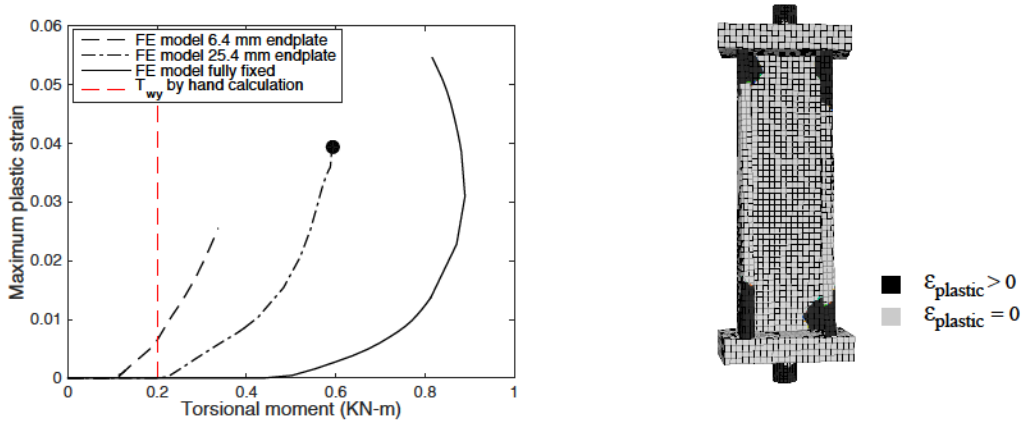

(a) (b)

Figure 2-15. Plastic demands in models (a) peak plastic strain – torsional moment relationship; (b) plastic strain locations in deformed geometry of "test model" with 25.4 mm end plate

To more fully explore the inelastic reserve, consider yielding in the cross-section as opposed to just the peak plastic strain. First, consider a simple indicator function for yielding in element j:

$$I_j = \begin{cases} 1 & \varepsilon_p > 0 \\ 0 & \varepsilon_p = 0 \end{cases} \tag{2-7}$$

where, ε_p is the effective plastic strain at mid-thickness of the shell element. Thus, the yielding must be through the thickness not just on the surface. This partially mitigates the influence of local plate bending on the measure. Plastification of a cross-section is then defined by:

$$P = \frac{\sum_{j=1}^{N} I_j}{N} \tag{2-8}$$

where, I_j, is the plasticity indicator for element j in a cross section; and N is the number of elements around the cross section. The plastic cross section ratio, P, is 0 when the cross section is elastic and 1 when the cross section is fully plastic. Figure 2-16 provides predicted P for the end and middle cross-sections as a function of (a) rotation, and (b) torsional moment. Plasticity initiates at the ends and continues to be greatest at the ends throughout the twist. Significant twist is required to approach full plastification of the section; however 75% of the end section is plastified by a twist of 10 degrees. The deformed shape and plastic strain for the model provided in Figure 2-15(b) is shown as • in Figure 2-16(a) and Figure 2-16(b).

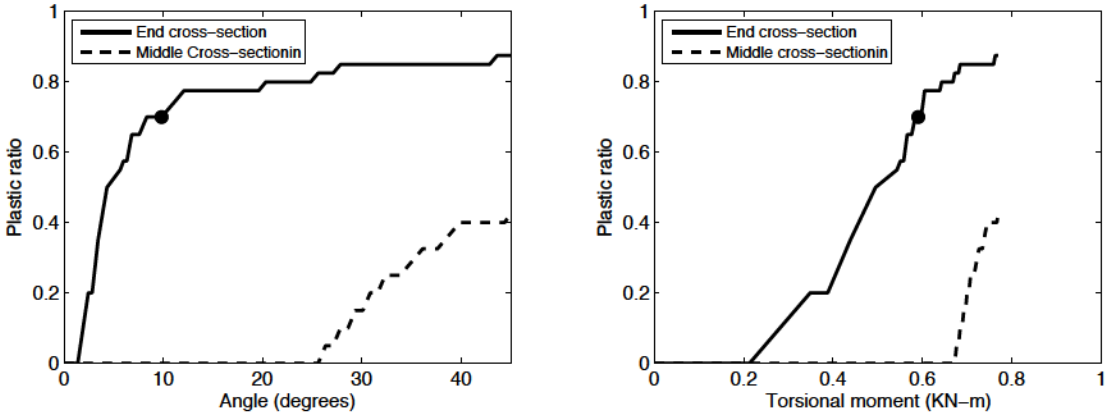

(a) (b)

Figure 2-16. Loading shaft effect on FE result: (a) offset effect; (b) diameter effect

2.6 Idealized Warping-Fixed Shell Finite Element Model for Torsion

The testing model required the addition of end plates and a loading shaft to the specimens. The result, as depicted in Figure 2-12(a), is that secondary bending moments and shears can develop as the member is twisted. In the "fully fixed" limit, Figure 2-12(b), the warping fixity is complete, and the secondary bending moments and shears are maximized. In this case the secondary stresses are large, and even for small deflection, the elastic stress response is in poor agreement with classical Vlasov torsion unless all secondary stresses are explicitly included. The objective of this work is to investigate torsion in isolation, so a third "idealized warping-fixed" model, Figure 12(c), is pursued in this section and used for subsequent parametric studies. This model allows bending to occur, but restricts warping, by restraining the member ends to remain in a rigid plane, but allowing that plane to twist (thus releasing the end moments, except for torsion).

The elastic longitudinal stresses (σ_z) that develop in the idealized warping-fixed shell finite element model are compared with the classical Vlasov warping theory in Figure 2-17. The σ_z from the shell finite element model are extrapolated to the nodes at the mid-thickness of the shell elements. The σ_w for the classical theory are determined via Eq. 2-2 which is implemented by finding the bimoment at the end from a beam finite element model ([7], [8]) and numerically determined ω and C_w [20]. The basic stress distribution is similar in both models, and the peak stress location is the same in both models, but the stresses in the shell finite element model are generally slightly lower (reflecting the additional flexibility of the non-rigid cross-section) resulting in a slightly higher prediction of the torque at which first yield occurs.

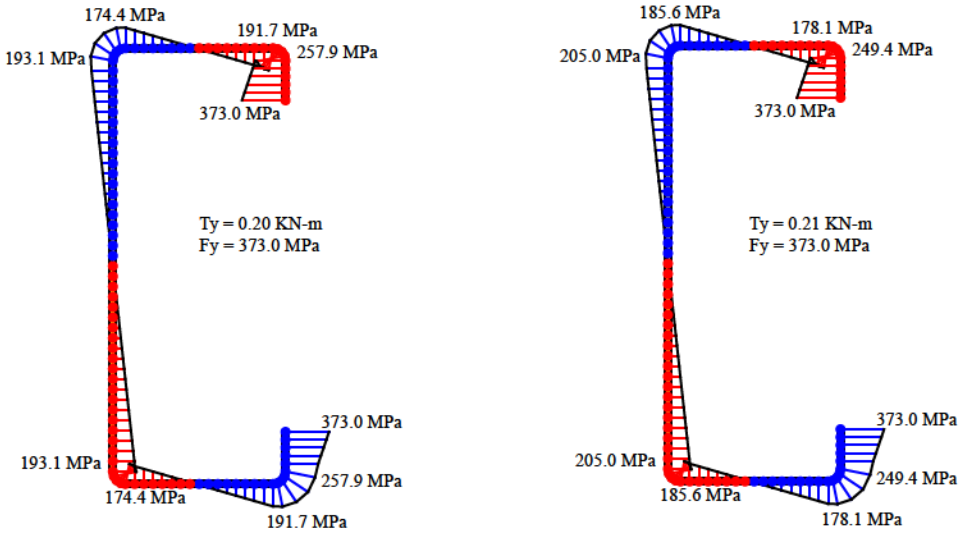

Figure 2-17. Longitudinal stress distribution at yielding torque (T_y=0.2 kN-m) from (a) classical Vlasov theory and (b) idealized warping-fixed shell FE model at the end cross-section

The torsion-twist response for the idealized warping-fixed model of the 400S162-54 with a length of 304.8 mm is compared with the fully fixed model and test results in Figure 2-18(a). The idealized warping-fixed model provides the most conservative estimation of the response: T_u = 0.48 kN-m and θ = 5.4 degrees at T_u. The deformation and developed plasticity at T_u are provided in Figure 2-18(b). Based on these results, it is included that the idealized warping-fixed model is most appropriate for exploring the strength in (isolated) torsion.

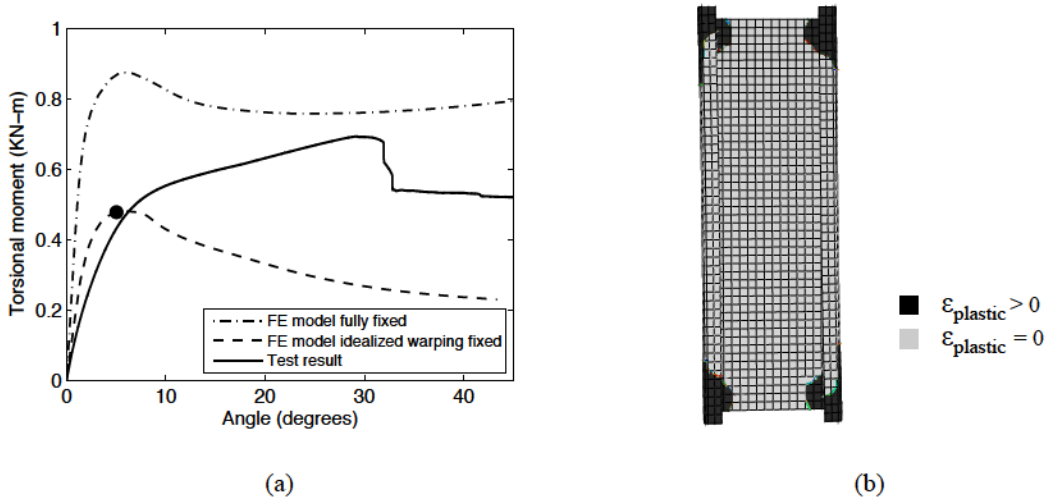

(a) (b)

Figure 2-18. (a) Torsional moment-angle curve for fully fixed model and idealized warping-fixed model; (b) Idealized warping-fixed FE model in ABAQUS

2.7 Development of Direct Strength Method for Torsion

The Direct Strength Method of cold-formed steel member design [5], [21] has shown that slenderness, with due consideration of both member and cross-section buckling modes, may be used to predict member strength in axial, bending, and shear actions. Similar relationships do not exist for torsion, and are investigated herein. The idealized warping-fixed shell finite element model is used to provide "exact" predictions of ultimate torsional capacity. Torsional slenderness is then used to develop "approximate" Direct Strength predictions appropriate for use in design.

Torsional slenderness is defined as

$$\lambda_T = \sqrt{T_y / T_{cr}} \tag{2-9}$$

where T_y is the torque at first yield and T_{cr} is the critical elastic torsional buckling moment, considering plate buckling. T_y is most rigorously defined as the T when $\sigma_{eff} = F_y$; however, for cross-sections dominated by warping torsion response T_y may be approximated by T_{wy}, i.e. the T when $\max(|\sigma_w|) = F_y$. The torsional elastic buckling moment T_{cr} may be determined from the shell finite element model, or approximated with other methods as discussed later in this section. For the 304.8 mm long 400S162-54 at F_y= 373 MPa, T_y= 0.21 kN-m as reported in Figure 2-17, and T_{cr} for selected modes of the shell finite element model are provided in Figure 2-19.

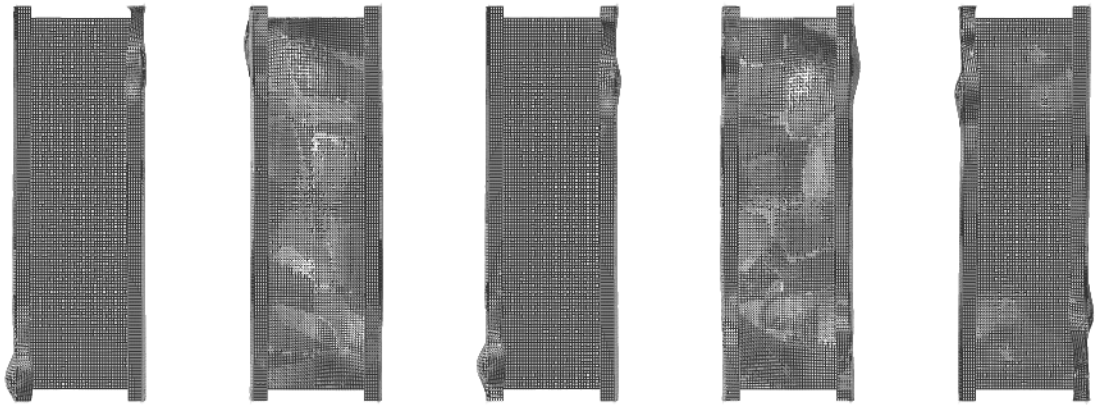

1st mode	2nd mode	3rd mode	4th mode	5th mode
T_{cr}/T_y= 7.47	T_{cr}/T_y = 7.76	T_{cr}/T_y = 9.08	T_{cr}/T_y = 10.45	T_{cr}/T_y =10.53

Figure 2-19. Buckling modes and critical torque for idealized warping-fixed shell finite element model

2.7.1 Parametric Study

To explore the relationship between torsional slenderness, λ_T and strength, a small parametric study is conducted. In the study λ_T is varied from 0.25 to 2.5 for four different physical lengths all completed with the 400S162-54 cross-section, by varying the yield

stress as summarized in Table 2-2. The basic torsion-twist results, for the studied sections are provided in Figure 2-20. By varying the physical length the elastic stiffness is varied and by varying the yield stress the ultimate torsional strength is varied. The end result is that a wide variety of strength responses from elastic, to nearly fully plastic, are realized in the studied models.

Table 2-2. Summary of parametric variation for 400S162-54 section

L	T_{cr}	$\alpha = EC_w/(GJL^2)$[1]	T_u min	T_u max
(mm)	(kN-m)		(kN-m)	(kN-m)
152	4.92	21.4	0.31	30.7
229	2.92	9.5	0.18	18.2
305	1.90	5.3	0.12	11.9
457	1.26	2.4	0.08	7.9

[1] consistent with Figure 2-4, for α, L is defined here as twice the model length

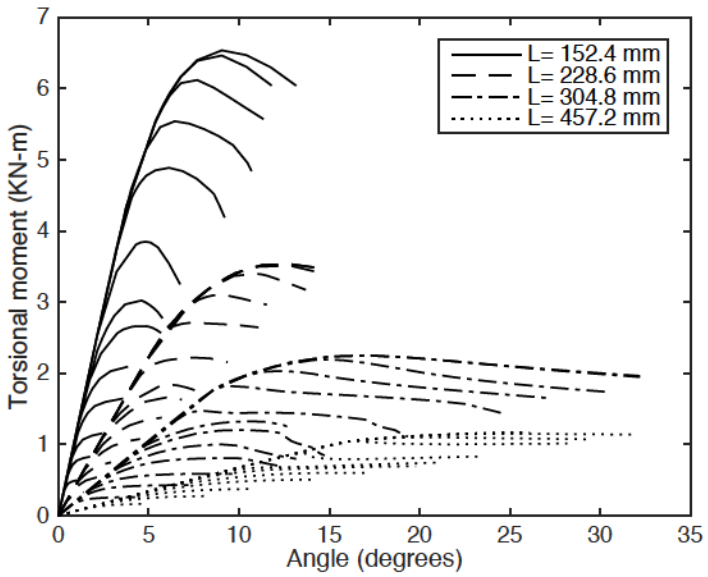

Figure 2-20. Torsional moment-angle curve for idealized models with different torsional

For each of the studied shell finite element models T_y and T_{cr} are determined. T_y is the applied torque at which the first yielded element occurs in the shell finite element model and T_{cr} is the first positive buckling moment from eigen-buckling analysis of the shell

finite element model. The observed peak strength (T_u) is examined as a function of torsional slenderenss in Figure 2-21 for the studied sections. The results indicate that significant torsional inelastic reserve is common, but lipped channels which are globally slender in torsion have only limited elastic post-buckling.

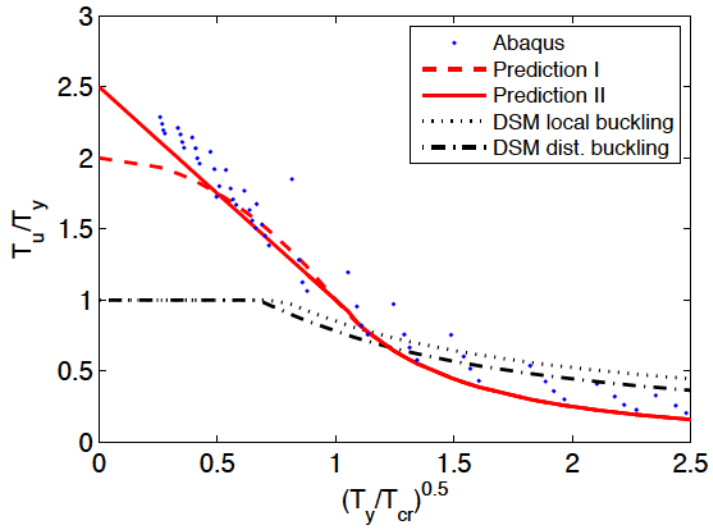

Figure 2-21. Direct Strength Prediction curve for members under torsion, exact solution for T_y and T_{cr}

2.7.2 Design Expressions

As provided in Figure 2-21, two possible design expressions are postulated: a two-part expression (Prediction I) that is quadratic in the inelastic reserve regime and asmytpotes to the elastic bucking solution for large global slenderness regime; and a two-part expression (Prediction II) that is linear throughout the inelastic reserve regime and then asymptotes to the elastic buckling solution. The expressions are as follows:

Prediction I: two-part with quadratic inelastic reserve

For $\lambda_T \leq 1$

$$T_n / T_y = 2 - \lambda_T^2 \tag{2-10}$$

For $\lambda_T > 1$

$$T_n / T_y = 1 / \lambda_T^2 \tag{2-11}$$

Prediction II: two-part design expression with linear elastic reserve

For $\lambda_T \leq 1$

$$T_n / T_y = 2.5 - 1.5\lambda_T \tag{2-12}$$

For $\lambda_T > 1$

$$T_n / T_y = 1 / \lambda_T^2 \tag{2-13}$$

The test-to-predicted ratio (P) for Prediction I is 1.19 with a coefficient of variation (V_P) of 0.19. Based on the reliability procedures outlined in Chapter F of AISI-S100 [5] for a reliability index β=2.5 this implies an LRFD resistance factor ϕ=0.84 or and ASD safety factor of Ω=1.9. Prediction II has a P of 1.13 with a V_P of 0.21 and therefore a ϕ=0.83 or Ω=1.9. For the studied sections either method is acceptable in design. Prediction II is consistent with the simplified method adopted for inelastic reserve in beams in AISI-S100 [5]; however Prediction I has a smaller COV and places a more conservative limit on the maximum torque, and is generally recommended.

2.7.3 Implementation in Design

To implement the prediction method the engineer must be able to quickly provide T_y and T_{cr}. Although approximate, it may be sufficiently accurate to determine classic Vlasov warping stresses due to torsion (σ_w) and set T_y as the torque at which $\max(|\sigma_w|) = F_y$. The warping stresses may be found using classical methods [3, 4, 5] or numerical methods [7,

8, 20]. If a shell finite element model is available it may be used for determining T_{cr}, in the absence of such a model we have investigated the use of the computationally efficient semi-analytical finite strip method (FSM) as implemented in CUFSM [22].

For the 400S162-54 the warping stresses that cause first yield in the section are generated and applied as the reference stress for an elastic buckling analysis. The signature curve results are provided in Figure 2-22. Three buckling modes are postulated by the signature curve analysis: lip local buckling, flange/web local buckling, and distortional buckling. The first two modes are observed in the shell finite element model, but at different buckling torques. These two buckling modes are compared to the shell finite element solutions of a 304.8mm long model with idealized warping-fixed end boundary conditions in Table 2-3. The FSM model presumes constant longitudinal stress, while in reality the longitudinal warping stress varies linearly along the length of the member with maximum values of opposing sign at the member ends. As a result of this variation the distortional buckling mode identified in the signature curve is not relevant since it has a long buckling length.

The implementation employed for the semi-analytical finite strip method [21] contains three serious simplifications for use in this application: (1) constant longitudinal stress (2) warping-free end conditions, and (3) no influence from shear stress. Assuming constant longitudinal stress is conservative, and one must consider the length of the stress gradient vs. the length of the buckling mode to determine the severity of this simplification. Typically local buckling is unaffected by stress gradients – and this is largely true even in

this case; however, other buckling modes generally require some consideration of stress gradient. Assuming warping-free end conditions when the applied stresses are based on warping-fixed end conditions is inconsistent and may be presumed as a coarse design approximation at best. The last 4 columns of Table 2-3 provide the FSM solutions for clamped, warping-fixed, end conditions. The model still assumes constant longitudinal stress, so even this remains conservative, and T_{cr} is further elevated by these conditions. The last assumption, ignoring the shear stress, is unconservative and recent work provides a means to include this aspect in the context of the semi-analytical FSM [23].

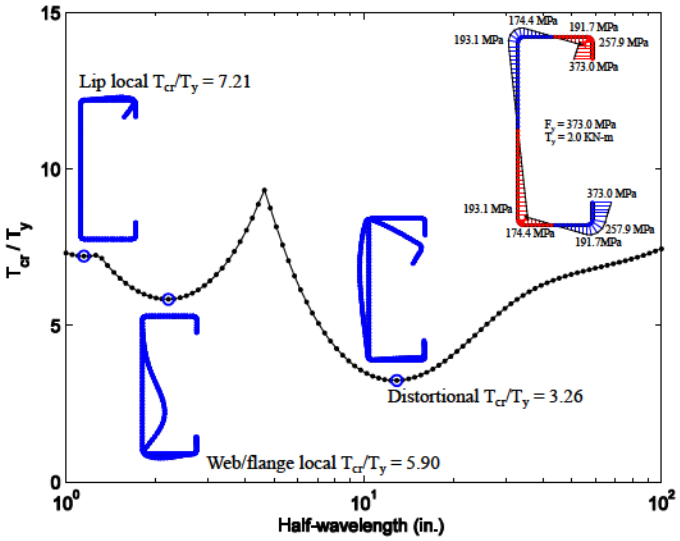

Figure 2-22. Signature curve in CUFSM for member under torsion

If T_y is defined by Vlasov's warping stress, and T_{cr} by the lip local buckling mode from a signature curve finite strip analysis then the parametric study results may be revisited. For these approximate solutions the strength as a function of slenderness is slightly modified, as provided in Figure 2-23 and the statistics for Prediction I and II are also modified. Prediction I has P=1.26, V_P=0.22, and ϕ=0.84 for β=1.9, while Prediction II has P=1.26,

V_P=0.22, and ϕ=0.84 for β=1.9. The approximate methods for T_y and T_{cr} determination are adequate for design.

Table 2-3. Comparison of elastic buckling solutions

	Shell FE[2]	Finite strip method[3] (constant longitudinal stress)					
		Warping-free ends		Warping-fixed ends			
L=	305 mm	signature curve		152mm	229mm	305mm	457mm
	T_{cr}/T_y	L_{cr} (mm)	T_{cr}/T_y	T_{cr}/T_y	T_{cr}/T_y	T_{cr}/T_y	T_{cr}/T_y
Lip Local Buckling	7.47	28	7.21	7.38	7.27	7.24	7.22
Flange/Web Local Buckling	7.76	56	5.90	6.63	6.20	6.06	5.97
Distortional Buckling	>10.53[1]	307	3.26	19.41	10.46	7.17	5.15

1. Not in first 5 modes, 2. "idealized warping-fixed" model, 3. CUFSMv4, 4. T_y, classic torsion F_y= 373MPa

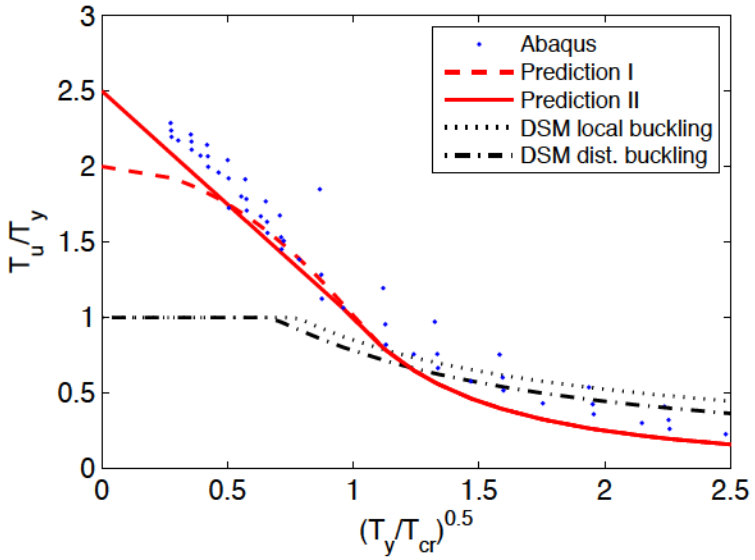

Figure 2-23. Direct Strength Prediction curve for members under torsion employing approximate solution for T_y and T_{cr} to evaluate the slenderness

2.7.4 Limitations and Future Work

The work presented herein is a limited investigation of torsion in cold-formed steel members. Significant work remains to develop a robust means of handling torsion. Although thin-walled members are dominated by warping torsion, additional cases (e.g. due to thickness, end boundary conditions, etc.) where the contribution of St. Venant torsion is non-negligible need further study. The potential longitudinal variation of warping stresses (i.e. variation in bimoment) is significant in structural applications, e.g. a floor joist loaded away from its shear center has a much different longitudinal warping stress distribution than the twisted member studied here. Systematic study of the impact of this variation (i.e., stress gradient) is needed to understand the impact on buckling modes and on yielding. Simplified methods are needed for predicting torque under partial or full plastification. The lack of a simplified calculation for plastic torque in thin-walled members leads to the type of gross simplifications provided in the currently developed prediction methods. Focused tests and models varying torsional slenderness in each of local, distortional, and global buckling are needed to fully understand the complete torsional strength. Torsion in combined loading should be revisited with the goal of investigating limit-states based strength interaction equations to replace the stress-based expressions in current use in design. Further testing, modeling, and analytical developments are all needed.

2.8 Conclusion

Torsional response is fundamental to understanding thin-walled cold-formed steel members; but beyond classical work on elastic response and prescriptive guidance little is available to engineers that must consider either torsion or buckling modes undergoing

torsion. Classical analysis of cold-formed steel members indicates that they often have high values of the non-dimensional constant $EC_w/(GJL^2)$ and may be often dominated by warping response. A small series of torsion tests on a cold-formed steel lipped channel demonstrates that cold-formed steel members can: undergo large twist rotations prior to failure, exhibit significant post-yield (inelastic reserve) strength, and are sensitive to end conditions. Complementary shell finite element models demonstrate the large extent of plastification in a common cold-formed steel member undergoing torsion and provide further insight on the sensitivity to end boundary conditions. The end boundary conditions in the torsion testing allow secondary shears and moments to develop at the fixed member ends, therefore an alternative idealized warping-fixed boundary condition is developed in the shell finite element models. This idealized warping-fixed model generates longitudinal warping stresses consistent with classic Vlasov torsion theory and is utilized to develop a small parametric study on torsional strength. For sections dominated by warping torsion, the study demonstrates that torsional slenderness may be used to predict ultimate torsional strength, in a manner consistent with Direct Strength Method design expressions previously developed for axial, shear, and bending actions. Simplified methods for calculating torsional slenderness are explored and shown to be adequate for design. Significant additional work remains to generalize the results and develop a fully limit-states based approach to torsional strength in cold-formed steel members, but the completed work is intended to provide proof that a clear path is possible and available.

2.9 Acknowledgements

The authors would like to thank the National Science Foundation (NSF-CMMI #1041578), American Iron and Steel Institute (AISI), ClarkDietrich, Steel Stud Manufacturers Association, and the Steel Framing Industry Alliance, The views expressed in this work are those of the authors and not NSF, AISI, or any of the participating companies or advisors. Testing was performed at the Structural Engineering and Earthquake Simulation Laboratory (SEESL) at the University at Buffalo. The authors would like to thank the SEESL staff for their expertise and cooperation.

2.10 References

[1] Vlasov VZ. Thin-walled Elastic Beams. Jerusalem Israel Program for Scientific Translations; 1961.

[2] Timoshenko SP, Gere JM. Theory of Elastic Stability. McGraw-Hill; 1961.

[3] Yu WW, LaBoube RA. Cold-Formed Steel Design. John Wiley & Sons, Inc.; 2000.

[4] AISC-Design Guide 9. Torsional Analysis of Structural Steel Members. Chicago, IL: American Institute of Steel Construction; 2003.

[5] AISI-S100-12. North American Specification for the Design of Cold-Formed Steel Structural Members. Washington (DC): American Iron and Steel Institute; 2012.

[6] Schafer BW, Madsen, R. AISI Torsion Provisions and Torsional Analysis of Cold-formed Steel Members. Structures Congress 2014, Massachusetts, Boston, March 2014.

[7] McGuire W, Gallagher R, Ziemian R. Matrix Structural Analysis. Wiley & Sons, Inc; 2000.

[8] MASTAN2 v3.3. Tutorial for MASTAN2. www.mastan2.com .

[9] Put BM, Pi YL, Trahair NS. Bending and Torsion of Cold-Formed Channel Beams. *Journal of Structural Engineering* 1999; 125 (5): 540-546.

[10] Gotluru BP, Schafer BW, Peköz T. Torsion in Thin-Walled Cold-Formed Steel Beams. *Thin-Walled Structures* 2000; 37 (2): 127-145.

[11] Ye Z, Kettle R, Li L. Analysis of Cold-Formed Zed-Purlins Partially Restrained by Steel Sheeting. *Computers and Structures* 2004; 82 (9-10): 731-739.

[12] Vieira L, Malite M, Schafer BW. Simplified Models for Cross-Section Stress Demands on C-section Purlins in Uplift. *Thin-Walled Structures* 2010; 48 (1): 33-41.

[13] Gao T, Moen C. Extending the Direct Strength Method for Cold-Formed Steel Design to Through-Fastened Simple Span Girts and Purlins with Laterally Unbraced Compression Flanges. *Journal of Structural Engineering* 2014; vol. 140: 6.

[14] EN 1993-1-3. Eurocode 3: Design of steel structures —Part 1-3: General Rules Supplementary rules for cold-formed members and sheeting. European Standard, CEN.; 2004.

[15] AISI-S200-12. North American Standard for Cold-Formed Steel Framing - General Provisions. Washington (DC): American Iron and Steel Institute; 2012.

[16] ASTM E8/E8M-13. Standard Test Methods for Tension Testing of Metallic Materials; 2013.

[17] Peterman KD, Bian G, Schafer BW. Experimental and Computational Analysis of Direct Torsion in Cold-Formed Steel Lipped Channels. In: Proceedings of Structural Stability Research Council Annual Stability Conference. Toronto, Canada. March 2014.

[18] Steel Stud Manufacturers Association. Product Technical Information. http://www.ssma.com .

[19] ABAQUS. ABAQUS/CAE User's Manual Version 6.12. Simulia; 2012.

[20] Li Z., Schafer, B.W. Buckling analysis of cold-formed steel members with general boundary conditions using CUFSM: conventional and constrained finite strip methods. In: Proceedings of the 22nd international specialty conference on cold-formed steel structures, St. Louis, MO. November, 2010. 17-32.

[21] Schafer BW. Review: The Direct Strength Method of Cold-Formed Steel Member Design. *Journal of Constructional Steel Research* 2008; 64(7): 766-778.

[22] Schafer BW, Ádány S. Buckling Analysis of Cold-Formed Steel Members Using CUFSM: Conventional and Constrained Finite Strip Methods. In: Proceedings of the 18th International Specialty Conference on Cold-Formed Steel Structures. St. Louis, MO. Octomber, 2006.

[23] Hancock GJ, Pham CH. Development in the Finite Strip Buckling Analysis of Plates and Channel Section under Localized Loading. In: Proceedings of the 22nd international specialty conference on cold-formed steel structures. St. Louis, MO, November, 2014. 295-309.

CHAPTER 3

COMPUTATIONAL EFFICIENT FASTENER-BASED MODELS OF COLD-FORMED STEEL SHEAR WALLS WITH WOOD SHEATHING

3.1 Abstract

The lateral behavior of sheathed, cold-formed steel (CFS) framed shear walls depends considerably on the complex behavior that occurs at each fastener location. Screw fasteners attach the sheathing material to the CFS framing, but relative motion of these components creates local damage, resulting in non-linearity at the scale of the entire shear wall. A computational model of a CFS shear wall is developed in which each fastener is represented by a non-linear, radially-symmetric spring element. The material parameters of the fastener element are determined from physical tests of sheathing-to-stud connections with small numbers of fasteners. The fastener material model includes a softening backbone curve, pinching, and loading and unloading parameters. The remainder of the model employs rigid sheathing panels, beam-column elements for framing, semi-rigid rotational springs for stud-to-track connections, and springs for hold-downs. The models are subjected to lateral cyclic displacement histories using the OpenSees structural analysis software. Thirteen full-scale shear wall tests of two different widths are modeled with various construction details related to the ledger track, gypsum board, vertical and horizontal seams, and number and thickness of field studs. The computational analyses are compared to the full-scale physical tests based on load-displacement behavior, lateral strength, drift at failure, initial stiffness, and energy

dissipation, and are compared to specification-based strengths and displacements. The computational models provide detailed information on forces in the framing members and interaction forces at individual fasteners. This fastener-based computational approach is able to efficiently reproduce key aspects of the lateral behavior of CFS shear walls.

3.2 Introduction

Load bearing cold-formed steel (CFS) structural systems are commonly used for low and mid-rise construction. Shear walls sheathed with oriented-strand board (OSB) are frequently used as the lateral force resisting system for seismic loads. The current seismic design standard for CFS structures in North America [1] allows only specific shear wall configurations based on type and thickness of sheathing, aspect ratio, fastener spacing, stud and track thickness, and screw size. The need to perform full-scale cyclic testing on all of the shear wall designs allowed by specification limits the possible configurations to a relatively small number [2]. Common elements of CFS construction, such as vertical or horizontal seams, gypsum wall board, and ledger tracks attached to the studs to allow the joists to frame in at their own spacing, are not accounted for in the specification-based lateral force and deformation values.

The development of performance-based seismic design methods for CFS structures requires the ability to efficiently perform realistic, non-linear computational modeling of shear walls with a wide variety of construction details. The computational modeling, of course, needs to be supported by specific physical testing at all scale levels, ranging from fasteners to shear walls to buildings. The research described in this 3hapter develops a computational model for the non-linear lateral behavior of CFS shear walls and validates

that model against thirteen existing full-scale cyclic test results. The key feature of the modeling approach is accurate representation of the non-linear force-displacement behavior that occurs at each fastener. This fastener-based shear wall model is incorporated into the general purpose structural analysis software OpenSees [3].

3.3 Behavior of Wood-Sheathed CFS Fastener and Shear Walls

Previous research on both wood-framed [4, 5] and CFS [6, 7] shear walls has established that the interaction between individual fasteners and the sheathing material is a significant factor in the non-linear response of the shear wall as a whole. Since the vertical framing members are essentially pin-connected to the horizontal members, the frame will deform into a parallelogram under lateral loads. The large in-plane rigidity of the sheathing will result in the sheathing remaining nearly rectangular in shape, while it primarily undergoes rigid body translation and rotation. The incompatibility between the deformed shapes of the frame (parallelogram) and sheathing (rotated rectangle) creates a relative displacement, or fastener displacement demand, at the location of each fastener. The fastener displacement demand must be accommodated by tilting and bending of the fastener itself, as well as deformation and damage to the sheathing material immediately surrounding the fastener. The ability of a fastener to tilt depends on the relative size of the screw to the CFS member thickness; large steel thicknesses prevent tilting and can lead to shear failure of the screws [8]. CFS shear walls tested with lateral loading commonly exhibit fastener failure modes such as tearing, pull-through or fastener fracture, which result from the fastener displacement demand imposed by the differing deformations of CFS members and sheathing material [9, 10].

3.3.1 Available Characterization of Fastener Response

The nonlinear shear response of a fastener connected through sheathing to steel can be determined in isolated testing. Motivated from work in sheathing braced design of studs a small test rig was modified by Peterman et al. [8] and used to generate monotonic and cyclic response of steel-fastener-sheathing combinations consistent with the shear wall testing in [10]. The small scale testing rig consists of two standard studs in a universal uniaxial testing machine, attached together by sheathing using fasteners. For symmetry two fasteners are placed between the sheathing and the stud and both faces of the stud are sheathed (See [8] for details). Focusing on a single fastener, before and after testing, the response for typical tests are provided in Figure 3-1.

(a) prior to testing (b) pull through (c) monotonic response

Figure 3-1. Isolated sheathing-fastener-stud testing for shear response (Peterman et al. [8])

3.3.2 Pinching04 Model for Fastener Response Fitting

In [8] it proposed that the shear response of the stud-fastener-sheathing may be approximated by the pinching04 model in OpenSees. Pinching04 model can be used to model 1D nonlinear behavior, including strength and stiffness degradation for unloading and reloading. To consider cyclic behavior, a backbone curve, reloading and unloading

criteria all need to be defined. Peterman et al. [8] provided these criteria based on their test. The backbone curve and four key backbone points for a typical pinching04 response are illustrated in Figure 3-2. From a modeling perspective, these four key points (or four branches in the backbone curve) represent the stiffness degradation for the fastener connection in shear. From a performance-based perspective, the origin point to node 1 is essentially the elastic range. The fastener tilts but with little to no permanent damage in the OSB. In the second branch (pt1 to pt2), some permanent damage occurs in the sheathing, primarily due to bearing. In the third branch (pt2 to pt3), the bearing damage of the fastener shifts against the sheathing begins to engage the head of the fasteners and pull-through initiates and further softening occurs. When the fastener pulls through a significant amount of sheathing, the nearing resistance lost and the strength quickly degrades. The final branch is the residual capacity of the connection and can approach 0. For thicker studs and smaller fasteners it is possible that the second and third branch is cutoff by shearing of the fastener. For fasteners with small edge distance, it is also possible that the second or third branch is cutoff by tear out in the sheathing. The specimens used herein did not suffer from fastener shear or edge tear out- so only bearing and tilting followed by pull-through is considered herein.

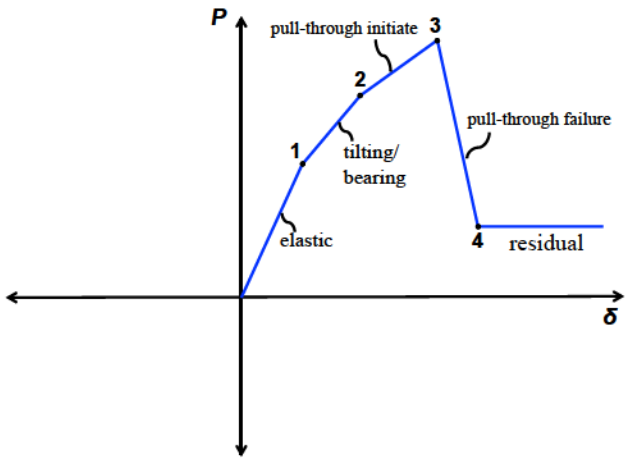

Figure 3-2. Backbone curve for fasteners

3.3.3 CFS Shear Wall Performance

Lateral deflection of wood-sheathed CFS shear walls may be estimated by Equation C2.1 of AISI S213 [1], which includes three linear mechanics-based deflection terms (cantilever bending, sheathing shear, hold-down deformation) and one empirical non-linear term. For typical shear wall configurations, the non-linear term is the largest contributor to the overall deflection and its percentage contribution increases with increasing load [11].

Several different computational or analytical methods have been used to capture the non-linear behavior of CFS or wood-framed shear walls. One modeling approach is to use a single, complex spring element to represent each shear wall [12, 13]. This approach requires full-scale cyclic test data to calibrate the spring element properties, but allows for modeling of entire buildings. A second approach uses finite element models of CFS shear walls with non-linear shell and fastener elements [14, 15]. In such models the

computational complexity typically precludes modeling of full buildings or a large number of different shear wall configurations.

For wood-framed shear walls, a fastener-based approach has been used to derive analytical expressions for key response parameters, such as lateral strength or total displacement, a detailed discussion of which is provided in Chen [16]. A fastener-based modeling approach for the full cyclic behavior of wood-framed shear walls has also been incorporated into the nail-pattern analysis module of the SAWS and SAPWood software [17, 18], as well as into general purpose finite-element software [5].

For CFS shear walls fastener-based analytical approaches to strength and displacement have also been developed [19, 20]. These analytical approaches only estimate peak strengths and deflections and do not attempt to capture the complete monotonic or cyclic load-displacement behavior. These analytical approaches also introduce some simplifying assumptions, such as rigid framing members with pin-connections or rigid hold-downs.

Fastener-based models of wood-sheathed CFS shear walls are able to capture key aspects of the non-linear response of the full shear wall by accurately modeling the local non-linear behavior at each fastener. The fastener-based models include realistic construction details, such as the actual pattern of fasteners, sheathing panel sizes and thicknesses, seam locations and seam backing members. In addition, the models accurately capture deformations and forces in the studs, tracks, ledgers and hold-downs. Fastener-based models can be implemented with a minimal amount of empirically derived input—

primarily non-linear fastener behavior—allowing them to be used for a wide range of non-standard construction details, as might occur in retrofit or development of new products or construction details. By implementing the fastener-based models within OpenSees additional analysis capabilities are available, such as combined gravity and lateral loading or dynamic excitation. The fastener-based approach can be used to assess the lateral behavior of the gravity load carrying elements of CFS buildings and the load sharing between the gravity and lateral systems. Fastener-based analyses of single shear walls provide sufficiently detailed non-linear behavior to allow calibration and validation of single, complex spring element models of shear walls that are more commonly used in non-linear analysis of full buildings. Computationally efficient non-linear analysis of CFS shear walls is ultimately required to advance performance-based seismic design of CFS buildings.

3.4 Description of Prototype Shear Wall and Computational Models

Thirteen different shear wall configurations (Figure 3-3, Table 3-1) were modeled, based on full-scale specimens previously tested. Complete details of the design and construction of the specimens are provided in Liu et al. [21]; model numbers used herein are the same as the physical test specimen numbers. All of the shear walls have a height of 2.74 m, and widths of either 1.22 m or 2.44 m. Walls 4 and 14 represent the baseline wall configurations with only CFS members, fasteners and sheathing, and correspond to the components that are directly accounted for in the lateral strength as determined by specification. Walls 2 and 12 include the ledger track; walls 3 and 13, gypsum board sheathing (on the face opposite the OSB). Prior experiments used in the development of the lateral strength provisions of the design specifications have almost exclusively used

specimens constructed with full 1.22 m x 2.44 m sheets of sheathing. Construction of shear walls of other dimensions requires both horizontal or vertical seams. Thus, walls 5, 6 and 10 study the effects of horizontal seam locations; and walls 7 to 10, of vertical seam and field stud locations. Finally, wall 15 examines the effect of field stud thickness.

All fasteners are #8 screws spaced at 15.2 cm on the perimeters of the OSB or gypsum panels, and spaced at 30.4 cm on the field studs. Hold-downs at the chord studs are Simpson S/HDU6. At locations on the bottom track where shear anchors (self-drilling screws or low-velocity fasteners) would normally be used, the physical tests used 16 mm diameter anchor bolts fastened to a steel tube.

The nodes and elements of Model 4 are shown in Figure 3-4; other models are similar in arrangement. Studs and tracks are subdivided by a node at every fastener location and are modeled by displacement-based beam elements with appropriate cross-sectional properties. The full composite section properties are used for back-to-back chord studs. The studs are connected to the top and bottom tracks with rotational spring elements to allow for semi-rigid connections (Figure 3-4b). The rotational stiffness of the semi-rigid connections was estimated to be 11.3 kN-m/rad, based on the measured lateral stiffness of bare CFS frames [21].

Each OSB or gypsum board panel is modeled as a separate rigid body (*RigidDiaphragm* in OpenSees), with slave nodes at every fastener location and a master node at the center of the panel. This model assumes that the significant deformation in the sheathing occurs

locally around the fasteners, and it does not include global shear deformation of the sheathing. Prior research on wood sheathed CFS walls has shown that a combination of low local stiffness at the fasteners with high sheathing diaphragm stiffness results in the overall wall behavior being controlled by the local behavior at the fasteners [22]. The rigid panel assumption may not be appropriate for shear walls sheathed with other materials, such as thin steel sheet, which undergo substantial deformation within the panel and smaller deformations surrounding the fasteners. As no panel edge contact or interference is included in the model, adjacent sheathing panels are free to move past one another or through the ground plane.

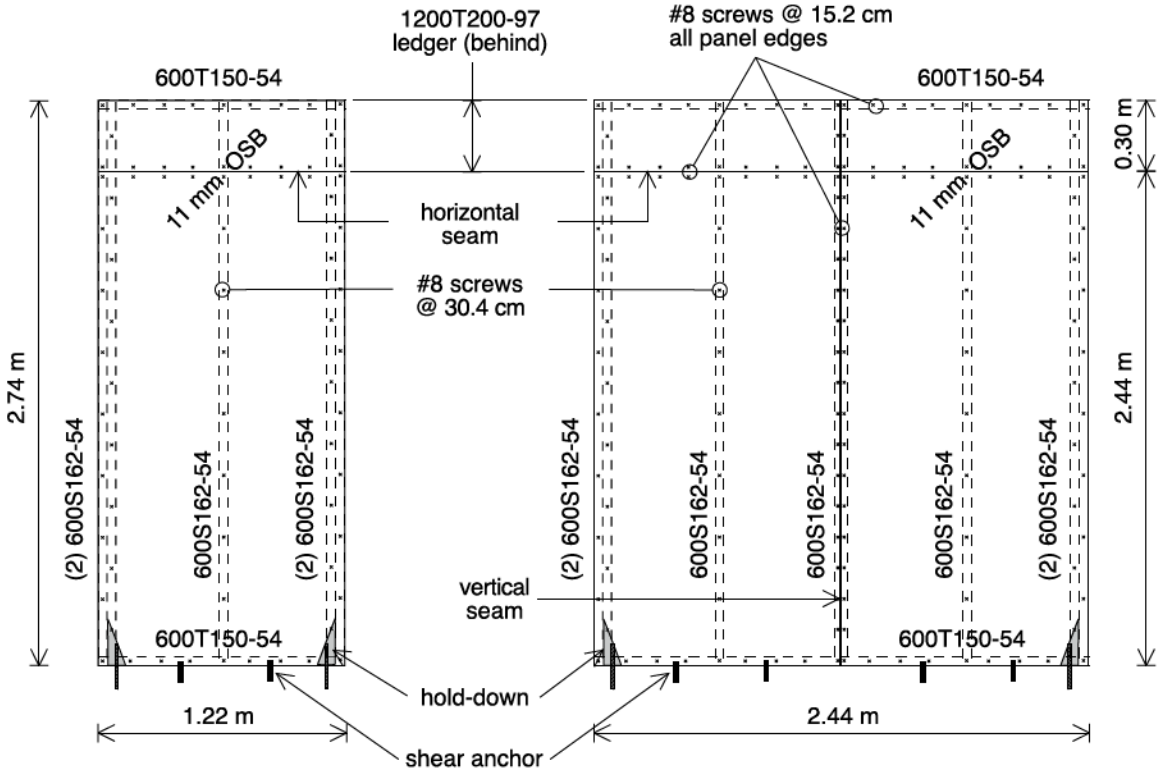

Figure 3-3. Shear wall configurations for Wall No. 2 (left) and Wall No. 12 (right); other walls are similar.

At each fastener location, there are two coincident nodes: one on the CFS framing member and one on the sheathing panel. These nodes are connected by a zero-length

element (*CoupledZeroLength* in OpenSees) with uniaxial force-deformation behavior, radially symmetric in the plane of the sheathing. Fastener-based models often use two independent perpendicular uniaxial spring elements, requiring approximation in the inelastic response; a single radially-symmetric spring element avoids such approximations.

The fastener elements are assigned the *Pinching4* material in OpenSees (Figure 3-5), which includes a multi-linear backbone curve, cyclic response, pinching, and unloading and reloading parameters [23]. The parameters of the *Pinching4* material were estimated from small-scale test results of fastener-sheathing assemblies, using combinations of fastener size, fastener spacing, sheathing thickness and CFS member thickness corresponding to the details of the shear walls tested at full scale and modeled herein (Table 3-2). A detailed comparison between the idealized *Pinching4* behavior and the experimental results of the fastener-sheathing assemblies is provided in Peterman et al. [24]. With the unloading and reloading parameters in Table 3-2, the *Pinching4* model of the fastener behavior is confined to the first and third quadrants, resulting in complete pinching to the origin. It is important to note that other than the material response parameters of the fastener elements, no other properties of the computational model are experimentally determined.

At vertical seams between sheathing panels, two independent fastener elements connect the adjacent rigid sheathing panels to a common node on the vertical stud. At horizontal seams, the two independent fastener elements are connected to a beam-column element representing the seam strap, which is pin-connected to the studs.

Table 3-1. Shear wall construction details and reference cycle displacements.

Wall or Model No.	Wall width	Ledger?	Gypsum Board?	Height of Horizontal Seam	Location of Vertical Seam	Field Studs (no. x thickness)	Reference Cycle (100% level)		Failure Cycle	
							Disp.	Drift	Comp.	Exp.
	m	✓ / --	✓ / --	m	m	mm	cm	%	%	%
2	1.22	✓	--	2.44	--	1 x 1.37	5.05	1.84	100	150
3	1.22	✓	✓	2.44	--	1 x 1.37	6.10	2.22	100	150
4	1.22	--	--	2.44	--	1 x 1.37	5.05	1.84	100	150
5	1.22	✓	--	2.13	--	1 x 1.37	5.05	1.84	100	150
6	1.22	--	--	2.13	--	1 x 1.37	5.05	1.84	150	150
7	1.22	--	--	2.44	0.31	2 x 1.37	5.05	1.84	100	150
8	1.22	--	--	2.44	0.61	2 x 1.37	5.05	1.84	150	200
9	1.22	--	--	2.44	0.61	1 x 1.37	5.05	1.84	200	200
10	1.22	--	--	1.37	0.61	1 x 1.37	5.05	1.84	200	200
12	2.44	✓	--	2.44	--	3 x 1.37	4.45	1.62	100	150
13	2.44	✓	✓	2.44	--	3 x 1.37	4.45	1.62	100	150
14	2.44	--	--	2.44	--	3 x 0.84	4.45	1.62	100	150
15	2.44	--	--	2.44	--	3 x 1.37	4.45	1.62	100	100

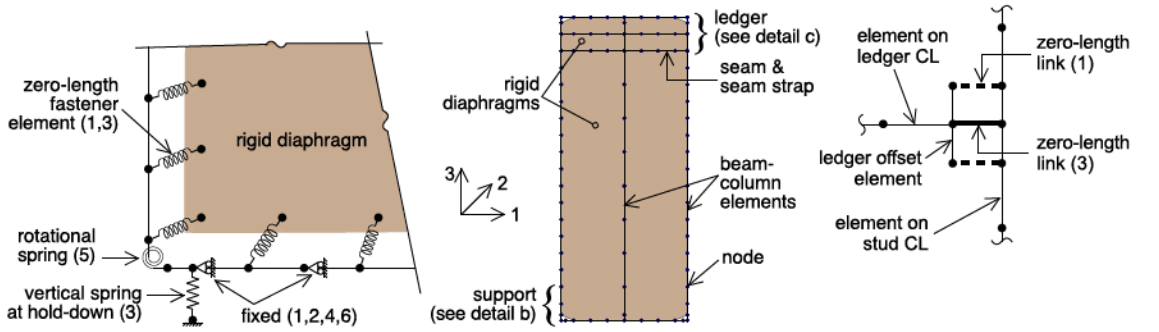

(b) Detail of fasteners and supports. (a) Typical mesh. (c) Detail of ledger-to-stud connection.

Figure 3-4. Computational Model 4: (a) full wall, (b) base details, and (c) ledger track details; other models similar. Numbers indicate restrained degrees-of-freedom at supports and active DOFs at springs or links.

The hold-downs are modeled as uniaxial spring elements active in the vertical direction only (Figure 3-4b). The hold-down elements have a tension stiffness of 9.9 kN/mm [12] and a compression stiffness 1000 times as large, to simulate a rigid foundation. At the locations of the hold-downs and shear anchors, the horizontal and vertical degrees-of-freedom are restrained.

The ledger track is modeled by a series of beam-column elements along its centerline, which are connected to the chord studs using a rigid link which transfers only vertical

forces (Figure 3-4c). Since the depth of the ledger track is large in comparison to the depth of the studs, bending moment will be transferred from the ledger to the studs through a moment couple of horizontal forces at the locations of the ledger flanges. Thus rigid offset elements and constraints are used to transfer horizontal forces to the chord studs at the ledger flange locations.

The model was subjected to the same cyclic lateral displacement history as the physical tests, applied through the center node of the top track. The cyclic displacement history followed the CUREE protocol in which each primary displacement cycle is followed by multiple trailing cycles of smaller amplitude [25]. The reference, or target, displacement (100% level) for each wall is based on the measured monotonic response of the shear walls. The cyclic displacement history also includes primary cycles of 150% and 200% of the reference displacement.

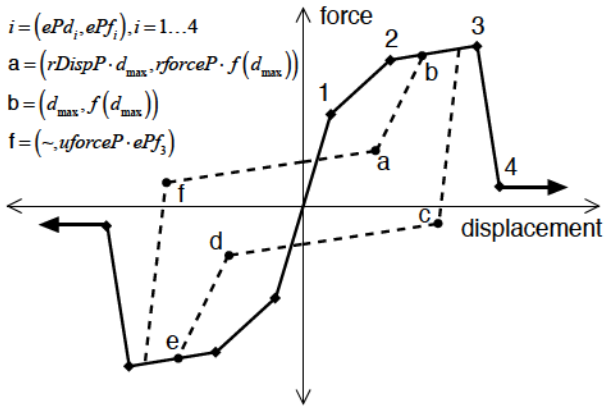

Figure 3-5. *Pinching4* material behavior with parameter definitions for positive branch; negative branch symmetric.

3.5 Results and Discussion

3.5.1 Load-Displacement Behavior and Energy Dissipation

The complete cyclic load-displacement responses from the computational models are compared to those from the physical tests in Figure 3-6 for the 1.22 m wide walls and in Figure 3-7 for the 2.44 m wide walls. Complete results from the physical testing program are presented in Liu et al. [21]. The computational models reasonably capture the backbone curve and pinching behavior. The load-displacement response of the computational models is confined entirely to the first and third quadrants, because the individual fastener behavior is similarly confined to the first and third quadrants. In contrast, the experimental data do exhibit some response in the first and third quadrants.

The load-displacement responses also show that the computational models and corresponding experimental tests do not always achieve peak lateral force during same displacement cycles of the same magnitude (Table 3-1). In most cases, such as for Model 5, the computational model reaches its peak strength at a smaller magnitude target displacement cycle than observed in the physical tests (Table 3-1). For Models 6, 9, 10 and 15, the computational model reaches its peak strength during the same displacement cycle as the physical tests. Even in the cases in which the computational model and physical tests reached peak strength during the same displacement cycle, the computational models tend to fail earlier in that displacement cycle. For example, Model 6 reaches its peak strength of 13.5 kN/m at a drift of 1.93% during the 150% cycle (2.76% target drift) and then loses lateral load capacity sharply. In contrast, the

experimental specimen continues to carry increasing lateral force until it reaches a drift of 2.57%.

Detailed comparisons between several primary peak load-displacement cycles are shown for Models 2 and 12 in Figures 3-8 and 3-9, respectively. Each figure compares the five largest amplitude displacement cycles from the CUREE protocol (40%, 70%, 100%, 150% and 200% of reference drift). Two smaller amplitude cycles occur between each of these peak cycles. The comparison of the individual cycles demonstrates that the model reasonably captures the overall hysteretic behavior at a wide range of imposed displacements, from nearly linear behavior to post-peak response. Both Models 2 and 12 (Figure 3-8) reached peak lateral force during the positive branch of the 100% cycle; while the corresponding experiments reached peak strength during the 150% cycle.

Table 3-2. Single fastener *Pinching4* parameters for positive branch; negative branch symmetric

	OSB		Gypsum	
	Backbone Parameters			
	ePd_i	ePf_i	ePd_i	ePf_i
point i =	cm	kN	cm	kN
1	0.051	0.98	0.02	0.22
2	0.198	1.56	0.119	0.44
3	0.625	2.05	0.605	0.53
4	1.052	0.22	1.422	0.53
	Unloading and Reloading Parameters			
rDispP	0.42		0.56	
rForceP	0.01		0.01	
uForceP	0.001		0.001	

The load-displacement cycle plots in Figures 3-8 and 3-9 also report the hysteretic energy dissipated in the given cycles. The computational models provide reasonable predictions of the single cycle hysteretic energy dissipation, except in the cycles for which the computational model has already failed in a prior peak cycle. For most single cycles, the experimental energy dissipation is larger than the computational due to several factors.

First, as mentioned above, the computational model does not capture energy dissipated in the second and fourth quadrants. Second, the experiments include sources of energy dissipation that are not captured in the computational models, such as friction between inner faces of the sheathing and the flanges of the CFS members, or edge effects between adjacent sheathing panels.

The final plot in Figures 3-8 and 3-9 provides the cumulative hysteretic energy dissipation as a function of peak drift. Individual points are plotted only at the primary cycles of the imposed displacement, but include energy dissipated in the smaller intermediate cycles. The vertical lines indicate the drift at which peak lateral force occurred for the computational analyses and the physical tests. The per cycle differences between energy dissipated in the computational model and experimental specimens, result in the cumulative computational energy always being less than that of the experiments. Nevertheless, the energy dissipation as calculated from the computational models may serve as a conservative and useful lower bound for the hysteretic energy dissipation in a physical test or real building. For seismic excitation of CFS buildings, the shear walls provide a significant source of energy dissipation. The ability to realistically reproduce the hysteretic energy dissipation in a computationally efficient model, even as a lower-bound, is an important capability for time history analysis of CFS buildings.

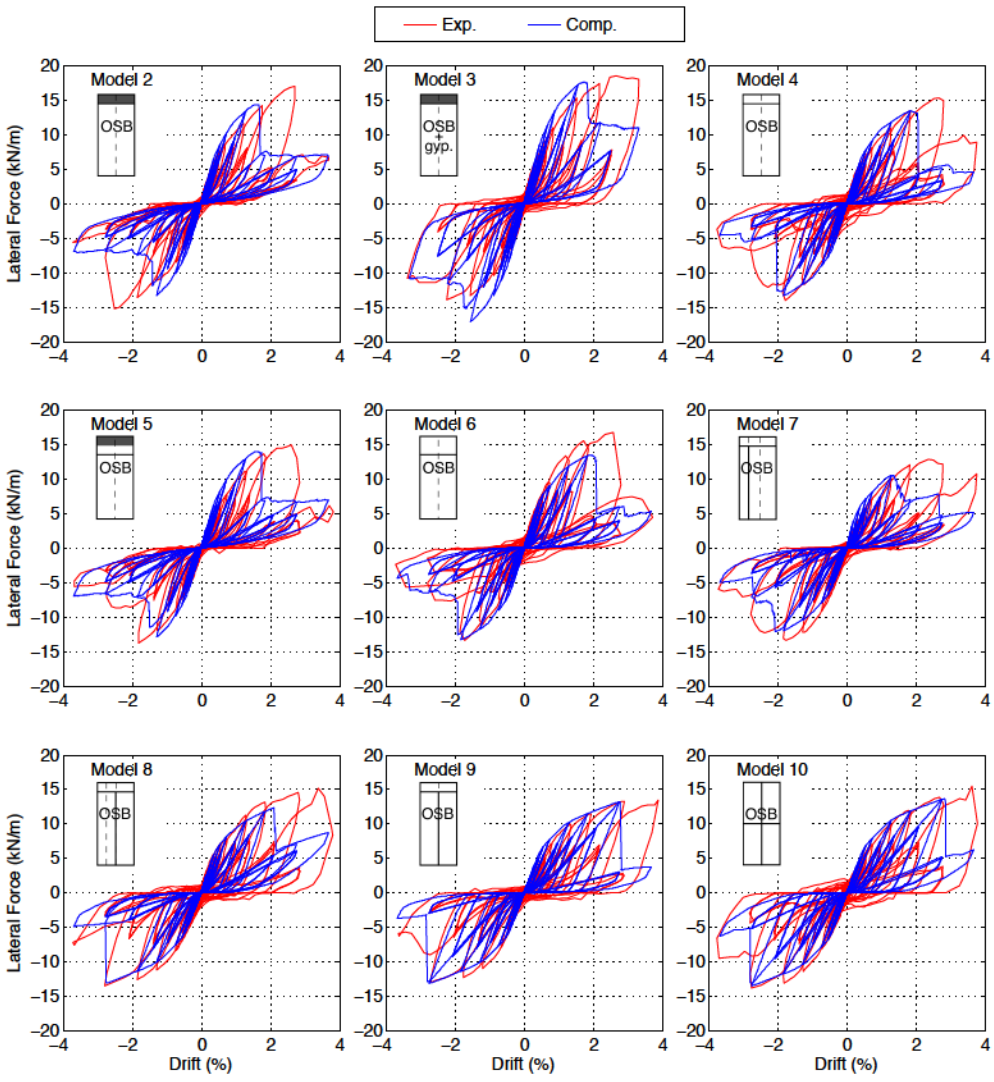

Figure 3-6. Load-displacement response for 1.22 m wide shear walls, Models 2 to 10.

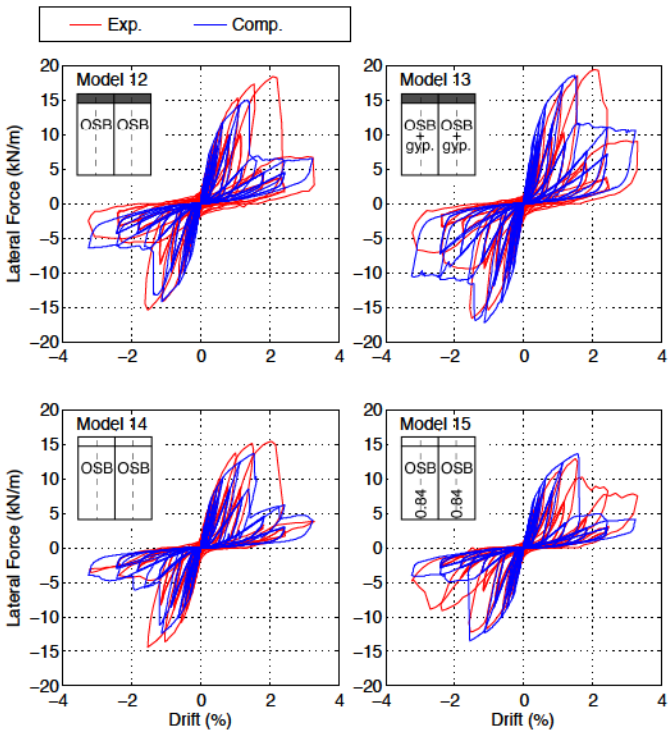

Figure 3-7. Load-displacement response for 2.44 m wide shear walls, Models 12 to 15.

3.5.2 Lateral Strength

Table 3-3 compares the peak strengths, normalized by the wall width, in the positive and negative directions from both the computational analyses and experimental tests, and it includes the mean and coefficient of variation (COV) of the strengths. In all cases except Model 15, the computational analysis provides a conservative (lower) prediction of the strength as compared to the experimental results, with ratios ranging from 0.81 to 0.98 and a mean of 0.88. For Model 15, the computational to experimental strength ratio is 1.06.

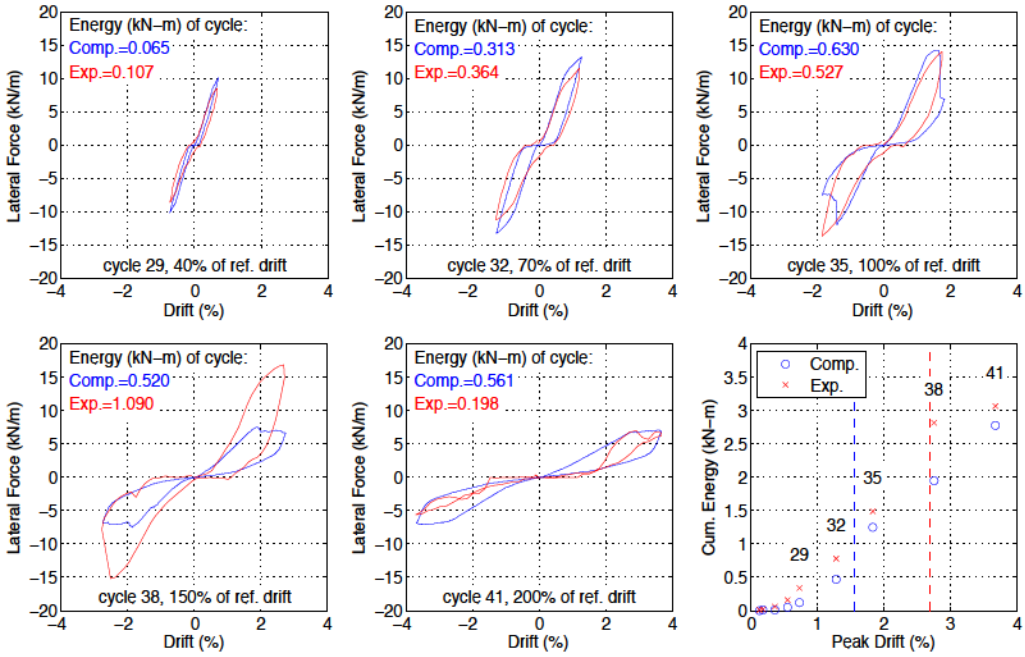

Figure 3-8. Model 2 load-displacement response for five peak cycles and cumulative hysteretic energy dissipation.

Many of the computational models reach their peak strength during a smaller magnitude target displacement cycle than the experiments; therefore an adjusted experimental strength is also determined for comparison. This adjusted experimental strength is equal to the experimental lateral force from the same displacement cycle and at the same lateral displacement for which the computational lateral strength occurred. This adjusted strength provides a better measure of the accuracy of the computational model up to the point of predicted failure. In this case, the ratio of computational to adjusted experimental strength ranges from 0.89 to 1.24, with an average of 1.03.

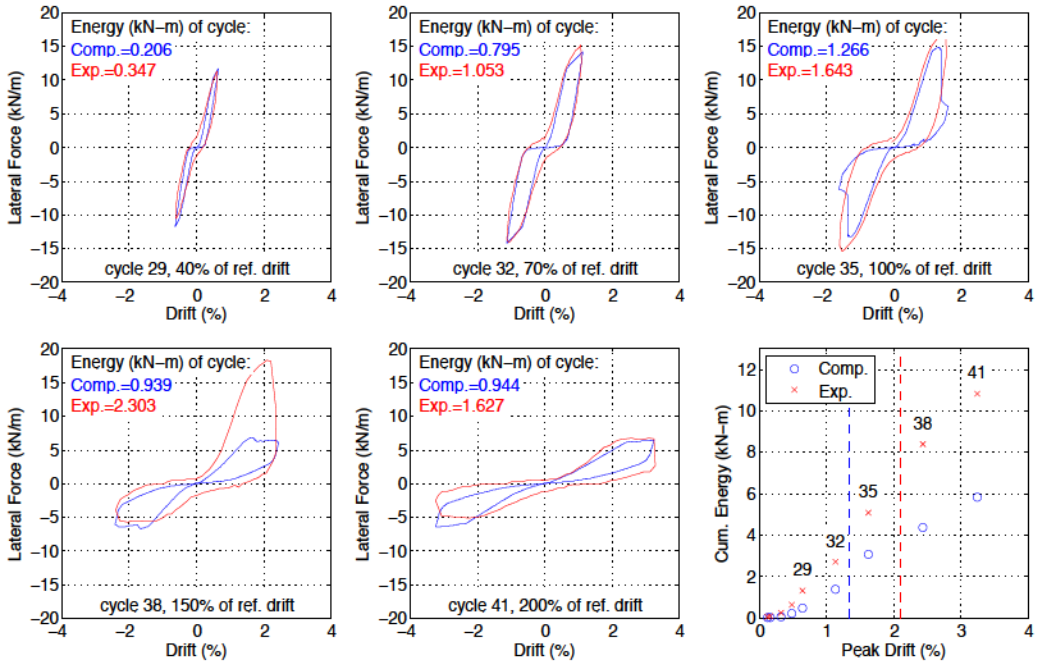

Figure 3-9. Model 12 load-displacement response for five peak cycles and cumulative hysteretic energy dissipation.

Peak strengths in the negative direction are smaller than those in the positive direction for all cases except Models 7 and 8 (Table 3-3). Both Models 7 and 8 have an asymmetrically placed field stud and atypical locations of vertical seams. The imposed cyclic displacement always has a peak in the positive direction first, as a result the strength in the negative direction is influenced by the prior failure of elements of the wall in the positive direction. See for example the 150% cycle for the experimental specimen of Model 12 in Figure 3-9. The computational-to-experimental strength ratios also exhibit greater variability for the strengths in the negative direction as compared to the positive direction.

Table 3-3. Raw and adjusted lateral strengths and strength rations in positive and negative directions.

	Positive direction					Negative direction				
Model	Comp. kN/m	Exp. kN/m	Exp. Adjusted kN/m	Comp. / Exp. --	Comp. / Exp. Adj. --	Comp. kN/m	Exp. kN/m	Exp. Adjusted kN/m	Comp. / Exp. --	Comp. / Exp. Adj. --
2	14.3	16.9	13.1	0.84	1.09	-13.3	-15.2	-11.2	0.87	1.19
3	17.6	18.5	15.9	0.95	1.11	-17.1	-14.0	-13.3	1.22	1.29
4	13.4	15.3	13.4	0.87	1.00	-13.4	-14.0	-13.3	0.95	1.01
5	14.0	14.9	12.7	0.93	1.10	-12.9	-13.9	-12.1	0.93	1.07
6	13.5	16.7	15.2	0.81	0.89	-13.3	-13.4	-12.3	1.00	1.08
7	10.5	12.8	10.0	0.83	1.06	-12.2	-13.4	-11.8	0.91	1.04
8	12.3	15.1	13.2	0.81	0.93	-13.1	-13.6	-13.5	0.97	0.97
9	13.2	13.4	10.6	0.98	1.24	-13.1	-13.0	-13.0	1.01	1.01
10	13.6	15.5	12.6	0.88	1.08	-13.5	-13.9	-13.7	0.97	0.99
12	14.9	18.3	16.4	0.81	0.91	-14.2	-15.4	-13.7	0.92	1.04
13	18.5	19.4	18.0	0.96	1.03	-17.3	-16.6	-9.3	1.04	1.86
14	13.6	15.4	15.1	0.88	0.90	-12.4	-14.4	-13.6	0.86	0.91
15	13.6	12.9	12.5	1.06	1.09	-13.5	-12.2	-11.0	1.10	1.23
Mean	14.1	15.8	13.7	0.89	1.03	-13.8	-14.1	-12.4	0.98	1.13
COV	0.14	0.13	0.16	0.08	0.10	0.11	0.08	0.10	0.10	0.21

Models 2 to 4 and 12 to 14 are most representative of typical CFS construction. Models 5 to 10 of the 1.22 m wide walls include variations in horizontal and vertical seam locations, and all of the 2.44 m wide walls include vertical and horizontal seams. In the physical tests, edge bearing between sheathing panels was clearly observed at large displacements. The computational models do not include interaction of adjacent sheathing panels, yet as a group the models with vertical seams have approximately the same mean strength ratios as those without the seams. An improved computational model could include panel interaction, but would also need to include a means of capturing local deformation and damage due to edge bearing forces.

Overall, the fastener-based computational models can effectively and conservatively predict the cyclic response of the shear walls up to the point of their peak lateral strength. Additional lateral strength may be available beyond this point, although it is not captured consistently with the present computational model. Many of the computational models fail during a smaller magnitude peak displacement cycle than the physical experiments,

indicating that the computational models are less accurately able to capture peak displacements and drift.

3.5.3 Lateral Displacement and Drift

Table 3-4 presents the deflections and drifts at peak load in both the positive and negative directions. The computational drift at lateral strength varies from 1.33% to 2.84% with a mean of 1.82%. The ratio of computational-to-experimental drift ranges from 0.56 to 1.05 with a mean of 0.70. As discussed above, most of the computational models reach peak lateral load during a smaller amplitude displacement cycle as compared to the experimental specimens, and thus are expected to have a smaller lateral displacement at peak load. Models 8, 9 and 10, which include additional vertical seams within a 1.22 m wide shear wall, exhibit greater drift capacity with little or no decrease in strength. Similar behavior was observed for these experimental specimens as well.

3.5.4 Comparison to Specification Values of Strength and Displacement

The lateral strength of each shear wall determined according to AISI S213-07[1] is compared to the strengths from the computational models and experiments in Table 3-5 and Figure 3-10. The ratios of computational-to-specification strengths, in the positive direction, range from 0.86 to 1.44 with a mean of 1.14. This ratio provides a measure of the over-strength that exists beyond the specification-based strength. Only for Model 7 is the computational strength (10.5 kN/m) substantially less than the specification-based value (12.2 kN/m). Model 7 includes a vertical seam that creates a very narrow sheathing panel (0.31 m wide) that is not accounted for in the specification. Although in this case the experimental strength (12.8 kN/m) was greater than both the specification and computational strengths. The computational models do not capture interaction between

adjacent panels, which is likely to be more significant for more walls with multiple vertical seams or narrow panels.

Comparison of displacements at the peak lateral strength calculated according to AISI S213-07 [1] and from the computational models (Table 3-5) shows that the specification typically substantially under-predicts the lateral drift capacity. The ratios of computational-to-specification displacements range from 0.87 to 2.01 with a mean of 1.33. Again, only Model 7 results in a predicted lateral displacement smaller than the specification-based value. The experimental specimens exhibited lateral displacements even greater than those from the computational models. These results confirm the previous conclusion from the experimental testing alone, that CFS shear walls may possess additional drift capacity beyond the specification-based value, although the amount of additional drift capacity varies widely [10, 21]. The computational models provide a far more accurate means to assess lateral displacements of shear walls as compared to the equations provided in AISI S213-07 [1].

3.5.5 Lateral Stiffness at Low Force Levels

Experimental and computational values of lateral stiffness at low force levels are compared in Table 3-6. The low-level computational stiffness is determined from the first analysis step, and thus is the true linear stiffness of the model. The experimental low-level stiffness is estimated in two ways from the data. First, the initial experimental stiffness is based on a best fit approximation from the measured force-deflection response over the first six displacement cycles of a magnitude of 5% of the reference displacement. This low-level experimental displacement should not create any damage to

the specimen, although small amounts of hysteresis do occur due to the experimental apparatus and lack-of-fit. Second, the experimental *Pinching4* stiffness is based on the idealization of the experimental load-displacement response of the wall as a whole using the *Pinching4* model [10]. Thus the *Pinching4* initial stiffness in Table 3-6 is the slope of the first branch of the backbone curve, which was defined to extend to 40% of the lateral strength, consistent with an equivalent energy elastic-plastic model. For most cases, the computational initial stiffness is less than the initial experimental stiffness, and in all cases the computational initial stiffness is greater than the stiffness based on the *Pinching4* backbone curve. As the non-linear response in both the computational models and experimental specimens begins at relatively low load levels, the lateral strength is not greatly affected by small differences in initial stiffness.

Table 3-4. Lateral deflections and drifts in positive and negative directions.

	Positive direction					Negative direction				
	Displacement		Drift		Comp. /	Displacement		Drift		Comp. /
	Comp.	Exp.	Comp.	Exp.	Exp.	Comp.	Exp.	Comp.	Exp.	Exp.
Model	mm	mm	%	%	--	mm	mm	%	%	--
2	43	74	1.56	2.70	0.58	-68.9	-35.3	-2.51	-1.29	1.95
3	49	73	1.79	2.66	0.67	-61.8	-42.7	-2.25	-1.56	1.45
4	50	73	1.84	2.66	0.69	-48.9	-50.3	-1.78	-1.84	0.97
5	43	72	1.57	2.62	0.60	-49.8	-35.3	-1.81	-1.29	1.41
6	53	71	1.93	2.58	0.75	-47.1	-50.5	-1.72	-1.84	0.93
7	36	65	1.33	2.36	0.56	-48.5	-57.4	-1.77	-2.09	0.85
8	58	93	2.12	3.38	0.63	-76.3	-75.1	-2.78	-2.74	1.02
9	77	107	2.79	3.89	0.72	-74.1	-75.7	-2.70	-2.76	0.98
10	78	100	2.84	3.64	0.78	-75.6	-75.7	-2.76	-2.76	1.00
12	37	58	1.34	2.10	0.64	-42.2	-31.2	-1.54	-1.14	1.35
13	40	56	1.47	2.04	0.72	-41.1	-31.2	-1.50	-1.14	1.32
14	43	56	1.56	2.06	0.76	-42.1	-31.2	-1.53	-1.14	1.35
15	43	41	1.57	1.50	1.05	-42.5	-43.1	-1.55	-1.57	0.99
Mean	50	72	1.82	2.63	0.70	-55.3	-48.8	-2.02	-1.78	1.20
COV	0.26	0.25	0.26	0.25	0.17	-0.24	-0.34	-0.24	-0.34	0.25

3.5.6 Typical Member and Fastener Behavior

Once benchmarked against the physical tests for global load-displacement behavior, the computational models allow for more detailed study of the response of the fasteners or framing members than is typically possible in a full-scale physical test. The magnified displaced shape of Model 4 (Figure 3-11) shows the sheathing panels rotating as rigid bodies, while the frame deforms as a parallelogram with some member curvature. Nodes that were coincident in the undeformed position separate, producing the fastener displacement demand. Since there are no contact elements included in these models, the edges of adjacent sheathing panels can move past one another or through the ground plane without interference, as can be seen in the upper left and lower right.

Table 3-5. Lateral strengths and displacements from computational models (positive direction) and AISI S213-07 design specification.

	Strength			Displacement		
Model	AISI Spec.	Comp.	Comp. / Spec.	AISI Spec.	Comp.	Comp. / Spec.
	kN/m	kN/m	--	mm	mm	--
2	12.2	14.3	1.17	42	43	1.02
3	12.2	17.6	1.44	42	49	1.16
4	12.2	13.4	1.09	42	50	1.20
5	12.2	14.0	1.14	42	43	1.02
6	12.2	13.5	1.10	42	53	1.26
7	12.2	10.5	0.86	42	36	0.87
8	12.2	12.3	1.01	42	58	1.38
9	12.2	13.2	1.08	42	77	1.82
10	12.2	13.6	1.11	42	78	1.85
12	13.7	14.9	1.09	32	37	1.14
13	13.7	18.5	1.35	32	40	1.25
14	13.7	13.6	0.99	32	43	1.32
15	10.2	13.6	1.34	21	43	2.01
Mean	12.4	14.1	1.14	38	50	1.33
COV	0.07	0.14	0.13	0.17	0.26	0.25

Figure 3-12 compares normalized axial force and moment diagrams at peak lateral force for the compression chord studs of Model 4 (no ledger) and Model 2 (with ledger). The axial forces are normalized by the yield force of the cross-section (P_y=247.5 kN based on

a yield stress of 345 MPa) without accounting for effects of buckling. At each fastener location, the vertical component of the fastener force creates a discrete step in the axial force diagram. The magnitudes of the individual fastener forces are similar for the models with and without the ledger. At the location of the ledger centerline in Model 2, a normalized axial force of about 3% of P_y is transferred to the stud, creating a slightly larger force throughout the height of the stud. A recent technical note suggests that the gradual transfer of axial force that occurs over the full height of the chord studs can be accounted for in design [26]. However, these computational models do not include gravity loads from the floor system or walls of higher stories, which may be larger than the variation within the height of the shear wall.

Table 3-6. Computational and experimental lateral stiffnesses at low force levels.

	Comp.	Experimental	
	initial	initial	at 40% strength
Model	kN/m	kN/m	kN/m
2	833	935	658
3	933	1097	722
4	743	1024	620
5	797	983	515
6	742	961	705
7	936	943	479
8	722	919	637
9	598	527	420
10	604	839	485
12	2812	2387	2001
13	3351	3224	1842
14	2315	3742	2192
15	2309	2262	1627

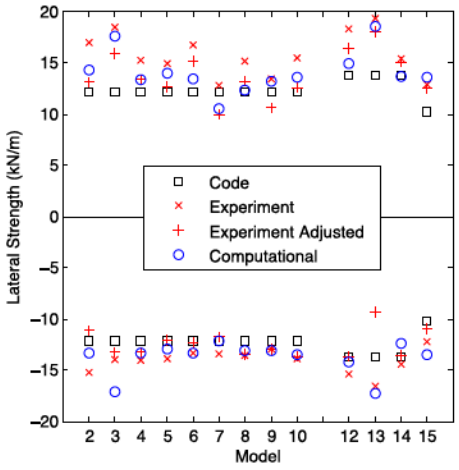

Figure 3-10. Summary of lateral strength measures for all models

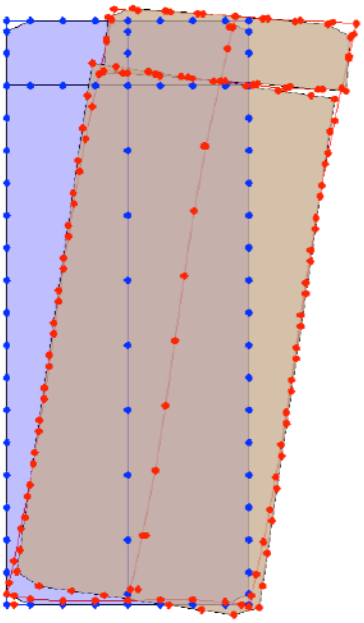

Figure 3-11. Initial and displaced shape (scaled by 10x) of Model 4 at peak lateral force

The moments in Figure 3-12 are normalized by the yield moment (M_y) of the double chord stud (2x600S162-54, where M_y = 1923 kN-mm, based on the weak-axis composite section modulus and a yield stress of 345 MPa). The chord stud in Model 4 (no ledger) undergoes approximately symmetric reverse curvature with peak normalized moment

ratios of about 0.25 M_y. There are small non-zero moments at the top and bottom of the chord studs due to the rotational springs that connect the chord studs to the tracks.

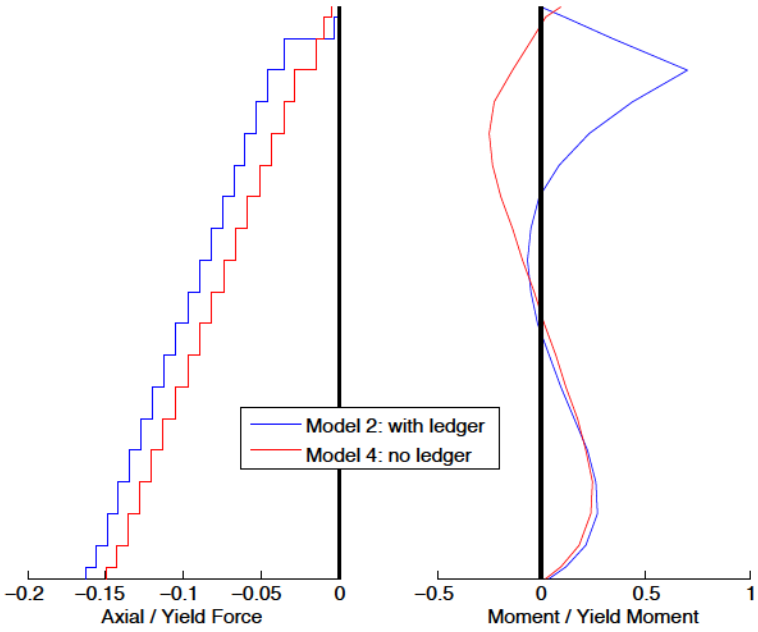

Figure 3-12. Normalized axial and bending forces in compression chord studs of Models 2 and 4 at peak lateral force

In Model 2 (with ledger), the chord stud also undergoes reverse curvature, but the stiff ledger track creates a large moment of about 70% of the yield moment at the location of the lower flange of the ledger. In a CFS-framed building, the ledger track would be continuous beyond the limits of the shear wall. Thus, the full ledger moment would not need to be transferred to the studs; some of the moment could be carried lengthwise along the ledger and distributed to other building elements. Future research should include modeling shear walls together with adjacent gravity-framed walls to more fully understand the influence of the ledger beam in distributing force and moment between the lateral and gravity wall systems.

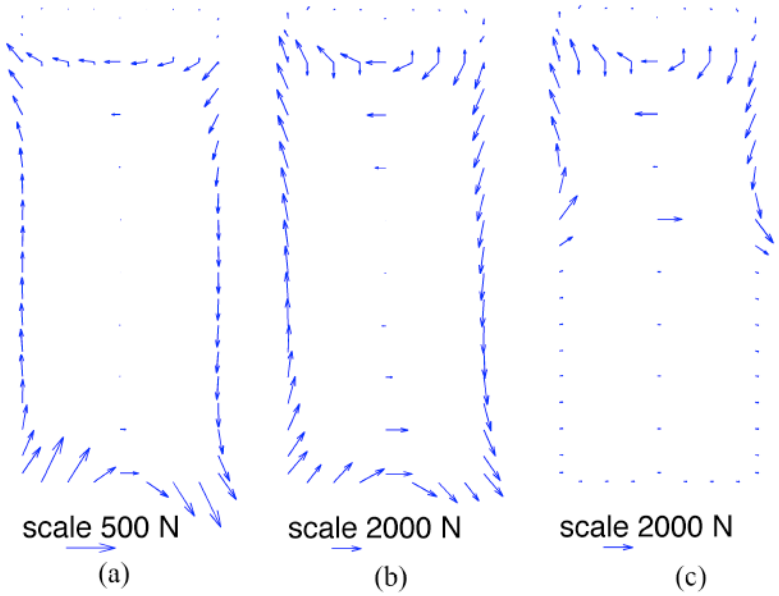

Figure 3-13. Vector force diagrams of fastener forces in Model 2 at three different levels: (a) elastic (1.7 kN/m), (b) peak lateral force (14.3 kN/m), (c) peak lateral displacement (6.9 kN/m).

Figure 3-13 shows three vector diagrams of the fastener forces from Model 2 for three different stages in the analysis—in the elastic range, at peak lateral force and at peak lateral displacement. The total lateral force applied to the wall is 1.7 kN/m, 14.3 kN/m and 6.9 kN/m for each of the three cases, respectively. Within each diagram, the vectors are plotted to a common force scale. For an individual fastener, non-linear response begins at 980 N and the strength of an individual fastener is 2050 N. The vector plots show that the fastener forces are vertical throughout most of the height of the chord studs, but near the panel corners the forces are oriented in a diagonal direction.

In the elastic case (Figure 3-13a), the fasteners at the lower corners carry the greatest forces, although the magnitudes of all the fastener forces remain small compared to the onset of non-linear response or strength. There are very small fastener forces along the central field stud and in the upper sheathing panel, indicating that the relative

displacement between the sheathing and framing at these locations is small. In Model 2, the presence of the stiff ledger track, which has the same overall dimensions as the upper sheathing panel, limits the relative displacements and fastener forces there.

At the peak lateral force (Figure 3-13b), the fastener forces along the chord studs still are primarily in the vertical direction. Near the panel corners, the fastener forces are large and oriented diagonally. In physical testing, the fasteners often tear off the corners of the OSB sheathing in a manner consistent with magnitude and direction of the forces observed in these computational analyses [21]. At the peak lateral force the magnitudes of the fastener forces in the chord studs and tracks are more uniform in magnitude as compared to the elastic case, due to the softening force-deformation response of the individual fastener elements. The fasteners near the lower edge of the upper sheathing panel and the fasteners near the top and bottom of the center field stud do carry significant forces, indicating increased relative displacement between the sheathing and framing members in these areas.

Finally at the peak lateral displacement (Figure 3-13c), all of the fasteners in the lower region of the wall have failed. The fasteners near the bottom of the wall fail first, at the occurrence of lateral strength. The fastener failures progress up the studs with little or no additional displacement, creating the large drop in lateral force that appears in the force displacement plots of Figures 3-5 and 3-6. For example, in Model 2 the force decreases from 14.3 kN/m to 7.2 kN/m at a drift of approximately 1.8% (Figure 3-8, 100% cycle). The residual strength of the wall is associated with the resisting moment created by the

fasteners in the upper half of the wall, which remain able to transfer force between the sheathing and framing. In all of the computational models, the failure of the shear wall as a whole was associated with failure of the fasteners beginning at the bottom and progressing vertically up the studs. In the physical tests, several different failure patterns were observed and failure did not always initiate at the bottom of the wall [21].

3.5.7 Effects of Specific Construction Details on Response

Models 4 and 14 represent the baseline wall configurations that include typical construction details and only those components (CFS members, fasteners, sheathing) that are directly accounted for in determining the lateral strength by specificaiton. The remaining wall specimens and corresponding models investigate the effects of various construction practices such as ledger track, gypsum board and seam locations. The experimental program described in Liu et al. [10, 21] discusses the effects of various construction details on the lateral behavior and overall the computational analyses confirm those observations.

Adding the ledger in Models 2 and 12 increases the strength slightly and decreases the drift at failure. Including the gypsum in Models 3 and 13, increases the initial stiffness and the strength, but has essentially no effect on the drift, as the gypsum will have failed at small drift levels. Comparing Models 2 and 5 (with ledger) or Models 4 and 6 (no ledger) shows that moving the horizontal seam down by 0.31 m has virtually no effect on the behavior. This assumes that the seam strap remains effective and does not fail.

Models 7 to 10 (compared to Model 4) explore the effect of vertical seam locations and additional gravity framing members. Model 7 has a substantially lower lateral strength

and displacement at failure, although in the physical tests these effects were not as significant. Model 8 has a smaller lateral strength in the positive direction, but nearly the same strength in the negative direction. Models 9 and 10 were able to sustain substantially larger drift levels, not failing until the 200% displacement cycle. The experimental data also showed that vertical seams in the middle of the wall (Models 8 to 10) did not result in significantly reduced strength and actually increased the ductility. Smaller sheathing panels may result in smaller relative displacements between sheathing and framing members, thus reducing the fastener displacement demand at a given force level. Model 15 explores the effect of lighter (0.84 mm) field studs in 2.44 m wide walls. In the computational analyses, the behavior is very similar, although the experimental data showed that the lighter field studs decreased strength and displacement at failure.

3.6 Further Application of Fastener-Based Models

The development of performance-based seismic design methods for CFS structures requires advanced non-linear modeling capabilities at a range of scales. Fastener-based models fill a computational need between detailed finite element models and simplified frame-type models. Fastener-based models allow the study of many more shear wall configurations than would be possible with full-scale testing alone and also allow for more detailed study of shear wall components. The detailed hysteretic load-displacement behavior output from fastener-based models can be used to help develop and calibrate single spring element representations for CFS shear walls. Fastener-based models could be extended beyond a single shear wall to include multiple shear walls, combinations of shear walls and gravity walls, or multi-story shear walls.

Future development could include modeling the shear flexibility of the sheathing material or incorporating non-linear behavior and other failure states within the framing members. Fastener-based based models provide a potential tool to assess the interaction of gravity and lateral load systems when subjected to seismic excitation. Fastener-based models could also be used to study the behavior of floor diaphragms and to capture realistic deformations rather than assume fully flexible or rigid behavior. Finally, the incorporation of the fastener-based methodology within a general purpose structural analysis software allows for incorporation of other analysis capabilities, such as application of gravity loads prior to lateral loads or earthquake excitation.

3.7 Conclusions

An efficient computational model for the lateral behavior of CFS shear walls was developed in OpenSees and validated against full-scale test results for thirteen different shear walls. The shear wall models included 1.22 m and 2.44 m wide walls with OSB sheathing and other varied construction details related to the ledger track, addition of gypsum board sheathing, horizontal and vertical seam locations, and field stud thickness and location. The modeling approach focuses on accurately capturing the non-linear behavior that occurs at the interface between the sheathing material and each fastener. The only experimentally derived input to the computational model are the parameters of the *Pinching4* material model for the fastener elements. These parameters were based on the results of physical testing of small-scale stud-sheathing-fastener assemblies. The current limitations of the model include the assumption of rigid diaphragms for the sheathing panels with no edge interaction, and CFS member elements that do not capture buckling effects.

The fastener-based computational model was able to reasonably reproduce key characteristics of the force-displacement hysteretic response of the physical tests. The average ratio of predicted lateral strength from the computational model to the experimental lateral force, measured in the same displacement cycle and at the same displacement, was 1.03. The average ratio of computational to experimental lateral displacements, measured at peak lateral force, was 0.70. In nine of the thirteen walls, the physical specimens were able to sustain one additional primary target displacement cycle beyond that predicted by the computational models. Compared to the specification-based strengths, the computational models predicted strengths 14% greater and drifts at failure 33% greater. The computational models were found to provide more reliable predictors of the experimental peak response than the values determined by current specification equations. Computational and experimental results were also compared using stiffness at low-force levels and energy dissipation.

The fastener-based models allowed for detailed study of the components of the shear wall. For example, member force diagrams indicate the transfer of force at each fastener to the studs. Vector fastener force diagrams allow for quantification and visualization of the magnitude and direction of the force imposed on the sheathing at every fastener location, providing confirmation and insight into failures observed during physical testing. Fastener-based models have many capabilities than can be enhanced to provide a more detailed understanding of the lateral response of wood-sheathed CFS shear walls.

3.8 Acknowledgements

This research was conducted as part of the U.S. National Science Foundation sponsored project "NEESR-CR: Enabling Performance-Based Seismic Design of Multi-Story Cold-Formed Steel Structures (CFS-NEES)" (NSF-CMMI-1041578). The project also received supplementary support and funding from the American Iron and Steel Institute and the Bucknell University Program for Undergraduate Research. Project updates are available at www.ce.jhu.edu/cfsnees. Any opinions, findings, and conclusions or recommendations expressed in this publication are those of the author(s) and do not necessarily reflect the views of the National Science Foundation or the American Iron and Steel Institute.

3.9 Reference

[1] AISI-S213-07. North American standard for cold-formed steel framing—lateral design. Washington, D.C.: American Iron and Steel Institute; 2007.

[2] Serrette R, Chau K. Estimating the response of cold-formed steel frame shear walls. AISI Research Report RP03-7; 2003, revised 2006.

[3] McKenna F. OpenSees: The Open System for Earthquake Engineering Simulation. http://opensees.berkeley.edu; 2014

[4] Folz B, Filiatrault A. Cyclic analysis of wood shear walls. J Struct Eng ASCE 2001; 127(4): 433-41.

[5] Xu J, Dolan JD. Development of nailed wood joint element in ABAQUS. J Struct Eng ASCE; 127(8): 968-76.

[6] Dubina D. Behavior and performance of cold-formed steel-framed houses under seismic action. J Constr Steel Research; 2008; 64: 896–913.

[7] Nithyadharan M, Kalyanaraman V. Modelling hysteretic behaviour of cold-formed steel wall panels. Eng Struct 2013; 46: 643–52.

[8] Peterman KD, Schafer BW. Hysteretic shear response of fasteners connecting sheathing to cold-formed steel studs. CFS-NEES RR04; 2013. http://www.ce.jhu.edu/cfsnees/publications.php.

[9] Fiorino L, Della Corte L, Landolfo R. Experimental tests on typical screw connections for cold-formed steel housing. Eng Struct 2007; 29:1761-73.

[10] Liu P, Peterman KD, Schafer BW. Impact of construction details on OSB-sheathed cold-formed steel framed shear walls, J Constr Steel Research 2014; 101: 114-23.

[11] Buonopane SG, Tun TH, Schafer BW. Fastener-based computational models for prediction of seismic behavior of CFS shear walls. Proceedings of the 10th National Conference in Earthquake Engineering, EERI 2014; [Anchorage, AK].

[12] Leng J, Schafer BW, Buonopane, SG. Modeling the seismic response of cold-formed steel framed buildings: model development for the CFS-NEES building. Proceedings of the Annual Stability Conference, SSRC 2013; [St. Louis, MO USA].

[13] Fülöp LA, Dubina D. Performance of wall-stud cold-formed shear panels under monotonic and cyclic loading. Part II: Numerical modelling and performance analysis. Thin-Walled Struct 2004; 42: 339-49.

[14] Martínez-Martínez J, Xu L. Simplified nonlinear finite element analysis of buildings with CFS shear wall panels. J Constr Steel Research 2011; 67(4): 565-75.

[15] Xuhong Z, Yu S, Tianhua Z, Yongjian L, Jin D. Study on shear resistance of cold-formed steel stud walls in residential structure. Advances in Engineering Structures, Mechanics & Construction 2006; 423-35 [Waterloo, Ontario, Canada].

[16] Chen CY. Testing and performance of steel frame/wood panel shear walls. Department of Civil Engineering and Applied Mechanics, McGill University, Montreal, Canada; 2004.

[17] Folz B, Filiatrault A. Seismic analysis of woodframe structures. I: model formulation. II: model implementation and verification. J Struct Eng ASCE 2004; 130(9): 1353-70.

[18] Pei S, van de Lindt, JW. SAPWood for Windows seismic analysis package for woodframe structures, version 2.0. Colorado State Univ; 2010. https://nees.org/resources/818.

[19] Fiorino L, Della Corte L, Landolfo R. Lateral response of sheathed cold-formed shear walls: an analytical approach. Eighteenth International Specialty Conference on Cold-Formed Steel Structures 2006; 603-19 [Orlando, FL, USA].

[20] Xu L, Martínez J. Strength and stiffness determination of shear wall panels in cold-formed steel framing. Thin-Walled Struct 2006; 44: 1084-95.

[21] Liu P, Peterman KD, Schafer BW. Test report on cold-formed steel shear walls. research report, CFS-NEES RR03; 2012. http://www.ce.jhu.edu/cfsnees/publications.php.

[22] Vieira LCM, Schafer BW. Lateral stiffness and strength of sheathing braced cold-formed steel stud walls. Eng Struct, 2012; 37, 205-13.

[23] Lowes L, Mitra N, Altoontash A. A beam–column joint model for simulating the earthquake response of reinforced concrete frames. PEER report 2003/10; 2004.

[24] Peterman KD, Nakata N, Schafer BW. Hysteretic characterization of cold-formed steel stud-to-sheathing connections. J Constr Steel Research, 2014; 101, 254-64.

[25] Krawinkler H, Parisi F, Ibarra L, Ayoub A, Medina R. Development of a testing protocol for woodframe structures. Report W-02, CUREE/Caltech woodframe project; 2000.

[26] LaBoube R. Design of end posts for diaphragm shear walls: a perspective. Cold-Formed Steel Engineers Institute, technical tote L300-09; 2009.

CHAPTER 4

OPENSEES MODELING OF WOOD SHEATHED COLD-FORMED STEEL FRAMED SHEAR WALLS CONSIDERING CHORD STUD FAILURE

4.1 Abstract

The objective of this chapter is to present an efficient spring-element and frame-element based finite element model of an OSB sheathed cold-formed steel framed shear wall that includes nonlinear hysteretic behavior from damage at the stud-to-sheathing connectors and the potential for buckling of the chord studs. The model is developed in OpenSees and has the potential to be an important building block tool towards modeling full structures framed from cold-formed steel. The authors have recently shown that OpenSees models that include nonlinear stud-to-sheathing fasteners, calibrated only to fastener-level tests, are capable of predicting full shear wall hysteretic performance as long as chord stud buckling or other limit states do not occur. Further, in other work, the authors have experimentally characterized the hysteretic performance of chord studs and developed phenomenological models appropriate for the frame-element in OpenSees. In this work, the two models are brought together to provide a highly adept shear wall model capable of capturing both fastener-based and member-based limit states in the shear wall. The model provides a means to explore the role of gravity load in the shear wall performance, and to study sensitivity of shear walls to these two competing limit states. Thus, the model provides practical design advantages and also provides a means to explore reliability of the shear wall as a system. The long-term goals of the work are to

create advanced analysis tools for cold-formed steel seismic design and system reliability knowledge that supports the use of those tools in models and designs of complete buildings.

4.2 Introduction

Cold-formed steel (CFS) structural systems continue to grow in use for low and mid-rise construction. Shear walls, combined with the floor and roof diaphragms, often constitute the lateral force resisting system for such cold-formed steel framed buildings. Wood sheathing, such as oriented strand board (OSB), is screw-fastened to cold-formed studs and tracks to develop shear stiffness as well as strength in the wall system. AISI S213 allows only specific shear wall configurations based on type and thickness of sheathing, aspect ratio, fastener spacing, stud and track thickness, and screw size. The configurations available in AISI S213 were largely established based on testing (e.g., Branston et al. 2006; Shamim and Rogers 2012). Methods for establishing shear wall capacities based on robust, but simple, models have been successfully advanced and implemented for wood framed shear walls (Folz and Filiatrault 2001).

Shear wall response is typically dominated by the local behavior at each steel-fastener-sheathing connection. As part of the NSF-funded CFS-NEES effort, a series of cyclic OSB-sheathed CFS-framed shear wall tests were conducted that form benchmark results for shear walls (Liu et al. 2012). In addition, cyclic steel-fastener-sheathing "fastener" tests covering the details employed in the shear wall tests were also completed (Peterman and Schafer 2013). Finally, and most recently, an OpenSees model of the benchmark shear wall tests that employed the cyclic "fastener" results to characterize a nonlinear

cyclic phenomenological model at the fastener locations demonstrated that the basic elastic and full non-linear cyclic response of the shear walls could be predicted based on the fastener-based results (Buonopane et al. 2014; Bian et al. 2014).

In seismic design CFS studs in shear walls carry axial force and bending moment from the lateral demands, and from gravity loads (dead, live, etc.). In current designs and experiments shear wall lateral resistance is typically dominated by fastener capacity. This is, in part, because low-rise buildings have more modest gravity demands, and because seismic design requires the studs to be designed for Ωo force levels (e.g. in OSB sheathed shear walls $\Omega o=3$ per current ASCE 7 provisions, thus the chord studs are designed with considerable reserve). However, as CFS framing is utilized for higher numbers of stories the gravity loads increase, in addition as capacity-based design methods and system reliability become more sophisticated Ωo is likely to be reduced. As a result, understanding the potential nonlinear role of the studs in the shear wall response is growing in importance.

As a companion to the CFS-NEES effort testing on the cyclic response of cold-formed steel axial and bending members was recently completed (Padilla-Llano et al. 2013). Specimens were selected such that their predicted monotonic capacity in compression was governed either by local, distortional or global buckling limit states as predicted by the Direct Strength Method in AISI-S100. Cyclic tests were then conducted to develop the full nonlinear hysteretic response including reduced stiffness, buckling, and post-buckling in compression, and yielding and eventually fracture in tension. Non-

dimensional parameters were utilized to develop general phenomenological models for members dominated by local, distortional, or global buckling limit states in compression and were implemented using the Pinching04 material in OpenSees (Padilla-Llano et al. 2013).

In this chapter, we bring together the fastener-based shear wall model and the nonlinear (stud) frame element model to provide a model capable of capturing both fastener-based and member-based limit states in a wood-sheathed CFS-framed shear wall. Monotonic and cyclic response of the shear walls are predicted from the developed OpenSees models so that the performance of these models with different limit states can be fully evaluated. The model provides a means to explore the role of gravity load in the shear wall performance, and to study sensitivity of shear walls to these two competing limit states. Thus, the model provides practical design advantages and a means to potentially explore reliability of the shear wall as a system.

4.3 Description of Numerical Models in OpenSees

The model developed in this work is implemented in OpenSees (i.e., the Open System for Earthquake Engineering Simulation, (Mazzoni et al. 2003)). OpenSees provides efficient solvers for earthquake building simulation and is widely used in seismic simulations. OpenSees derives much of its efficiency from primarily being a frame element based code, and providing an extensive library of phenomenological based models. The models developed herein are implemented in OpenSees and take advantage of its strengths. Other more general purpose finite element software, e.g. ABAQUS (Simulia 2012), provides more extensive libraries of elements and material models, but is not as efficient or

purpose-built as OpenSees. This section provides the details for the OpenSees-based shear wall mode developed here.

A typical OSB-sheathed, CFS-framed shear wall from Liu et al.'s (2012) testing is selected as a benchmark (see Figure 4-1a). The selected specimen is designated as specimen test-2 in Liu et al. (2012) (Liu et al. 2014; Liu et al. 2012). The primary dimensions of the shear wall are 1.22 m [4 ft.] wide by 2.74 m [9 ft.] high. The shear wall is framed with 600S162-54 studs, 11.11 mm [7/16 in.] OSB on one face, using #8 fasteners at 152.4 mm [6 in.] spacing in the perimeter and 304.8 mm [12 in.] spacing in the field connecting the OSB to the CFS framing. A 1200T200-97 ledger was fastened to the back side of the frame at the top of the shear wall. At the base Simpson S/HDU6 hold downs are connected to the chord studs, and 15.88 mm [5/8 in.] diameter bolts through the bottom track to the base. At the top, #10 38.1 mm [1 ½ in.] self-drilling screws spaced at 76.2 mm [3 in.] connect through the top track to the loading beam.

4.3.1 Material and Element in OpenSees

The CFS framing members, including the stud and tracks, are subdivided into 20 and 8 beam-column displacement elements respectively, with nodes at each fastener location. Linear elastic material and beam-column elements were used to model the field stud and tracks. To provide for stiffness reduction, buckling, and post-buckling of the chord studs they were modeled with a purpose-built implementation of the Pinching04 material as detailed in Section 3.2.2.

Rotational springs were used to connect the studs and top/bottom tracks (See Figure 4-1b). Stiffness for the rotational spring is set at 113 KN-m/rad [100 kip-in./rad] based on approximations from the measured lateral stiffness of bare CFS frame tests (Liu et al. 2012). Each individual sheathing board was modeled as a rigid diaphragm with slave nodes at each fastener location and a master node at the center of the sheathing board.

The ledger was modeled with a beam-column displacement element with fixed degrees of freedom at the ledger-stud connections. This rigid offset transferred deflection from the studs to the ledger. At seams between OSB sheets a strap was used. Displacement beam-column elements were used to model the strap with its actual cross sectional properties. The rotational stiffness for the strap-to-stud connection was the same as that for stud-to-track connection. The seam introduces two separated (top and bottom) rigid diaphragms (one for each board). For simplification, interference between the individual diaphragms through edge bearing is ignored.

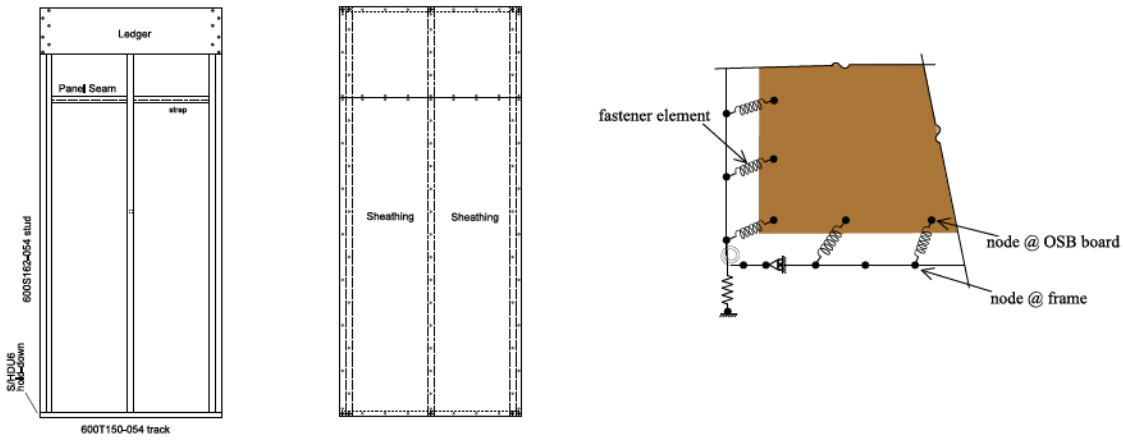

(a) benchmark CFS-framed shear wall (b) corner modeling detail in OpenSees

Figure 4-1. Shear wall model details in OpenSees

We used two reference nodes with fixed degrees of freedom as the foundation. Zero-length elements connecting foundation nodes and two nodes at the chord studs were modeled as hold-downs. Based on Simpson Strong-Tie published values of tension strength and displacement, tension stiffness for the hold-down of 9.9 KN/mm [56.7 kips/in] was selected while the compression stiffness of the hold down was modeled as 1000 times larger to simulate bearing against a rigid foundation. The translational degrees of freedom at two bottom-track nodes were fixed to simulate the shear anchors at these locations (See Figure 4-1b).

At fastener locations, the nodes of the frame members and the sheathing coincide. As shown in Figure 4-1b, these nodes are connected using zero-length springs. Pinching04 (Lowes et al. 2003) was assigned as the material model for the zero-length fastener elements. The parameters required to define the Pinching04 uniaxial material in OpenSees, which includes the backbone curve, degradation factors, and other force and displacement relation parameters, are estimated from separate physical testing of the fasteners as reported by Peterman and Schafer (2013) (Peterman et al. 2014). Table 4-1a and b provide the parameters used in cyclic loading to define the Pinching04 material for the zero-length fastener springs. Fastener backbone curves for monotonic and cyclic differ because of the cumulative damage in cyclic loading. The backbone curves of fasteners for monotonic and cyclic loading for two different thickness studs are compared in Figure 4-2.

Table 4-1. Cyclic Pinching04 parameters in shear wall model (model is symmetric)

(a) Backbone curve

steel thickness mm	loading	*ePd1* mm	*ePd2* mm	*ePd3* mm	*ePd4* mm	*ePf1* kN	*ePf2* kN	*ePf3* kN	*ePf4* kN
0.84	Monotonic	0.87	3.70	7.70	10.00	0.76	1.50	1.90	1.50
	Cyclic	0.51	2.10	6.50	12.00	0.71	1.30	1.70	0.12
1.40	Monotonic	0.56	3.10	6.70	8.60	0.86	1.70	2.10	1.70
	Cyclic	0.51	2.00	6.30	10.00	0.98	1.50	2.00	0.22

(b) Unloading and reloading parameters

steel thickness mm	Unloading and reloading Pinching4 Parameters					
	rDispP	*rForceP*	*uForceP*	*rDispN*	*rForceN*	*uForceN*
0.84	0.41	0.01	0.001	0.41	0.01	0.001
1.40	0.42	0.01	0.001	0.42	0.01	0.001

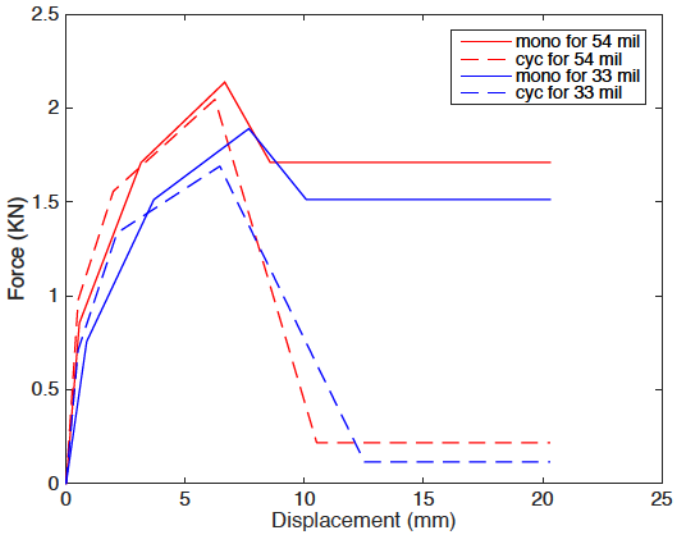

Figure 4-2. Backbone definition for fasteners in different chord stud thickness

4.3.2 Development of Chord Stud Model in OpenSees

Modeling the hysteretic behavior, including the effect of buckling deformations in CFS axial and flexural members using nonlinear-beam column elements, has been recently

explored in Padilla-Llano et al. (2013, and 2015). In this chapter, the nonlinear behavior in the axial direction was modeled using the Pinching04 material, and elastic stiffness was assumed for flexure. The modeling strategy consists of hysteretic behavior at the cross-section level using a nonlinear beam-column element with distributed nonlinear axial load-strain (P-ε) section behavior (see Figure 4-3b). The underlying behavior model is depicted in Figure 4-3c and is based on the formulation of the Pinching04 material model, as currently implemented in OpenSees.

Three components of the behavior model are needed: backbone curve, unloading-reloading paths that account for pinching, and a damage model for strength and stiffness degradation. The parameters that define these three parts can be obtained from the general expressions for modeling steel columns including local buckling developed by Padilla-Llano et al. (2015). Backbone curves, and parameters for strength degradation, stiffness degradation and pinching were calculated as a function of the local cross-section slenderness $\lambda\ell$. The distributed nonlinearity approach allows flexible modeling of thin-walled steel members subjected to different axial loading conditions, e.g. non-uniform axial load resulting from the contributions of individual fasteners attached to a chord stud in a shear wall. The parameters used in the examples presented in this chapter are summarized below.

Pinching04 parameters	600S162-33	600S162-54
gF2	0.43	0.43
gF4	0.57	0.57
gD2	0.46	0.51
gD4	0.08	0.13
rDispP	0.42	0.42
rForceP	0.46	0.46
uForceP	-0.02	-0.02
rDispN	0.38	0.38
rForceN	0.89	0.89
uForceN	0.21	0.21
gE	1.57	2.38

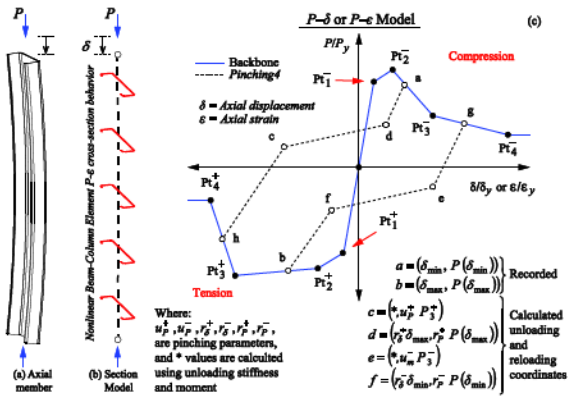

Figure 4-3. Axial hysteretic model for CFS axial members experiencing local buckling (Padilla-Llano et al. 2015)

4.4 Finite Element Results and Discussion

This section explores the impact of loading (monotonic vs. cyclic), gravity load, and chord stud thickness on the predicted response of a CFS-framed shear wall based on the developed OpenSees models. In addition to providing comparison to benchmark shear wall testing, a brief comparison is also provided to a more high fidelity model using shell elements in ABAQUS.

4.4.1 Fastener-Based Modeling Result in OpenSees

The model developed in Section 3.2 is implemented and compared with the benchmark testing from Liu et al. (2012) in Figure 4-4. The only differences between this model and earlier fastener-based OpenSees models (Buonopane et al. 2014; Bian et al. 2014) are the inclusion of the nonlinear chord stud response, and a slight modification to the location of the hold downs in the model. Previously, the hold downs had been modeled with a small offset, but this lead to numerical difficulties and was simplified here to align directly with the stud. The results for the new model are nearly identical to before and indicate that the model developed in Section 3.2 can provide a reasonable approximation of shear wall

response, and further, that the introduction of the nonlinear chord stud modeling does not influence the results at low levels of axial load.

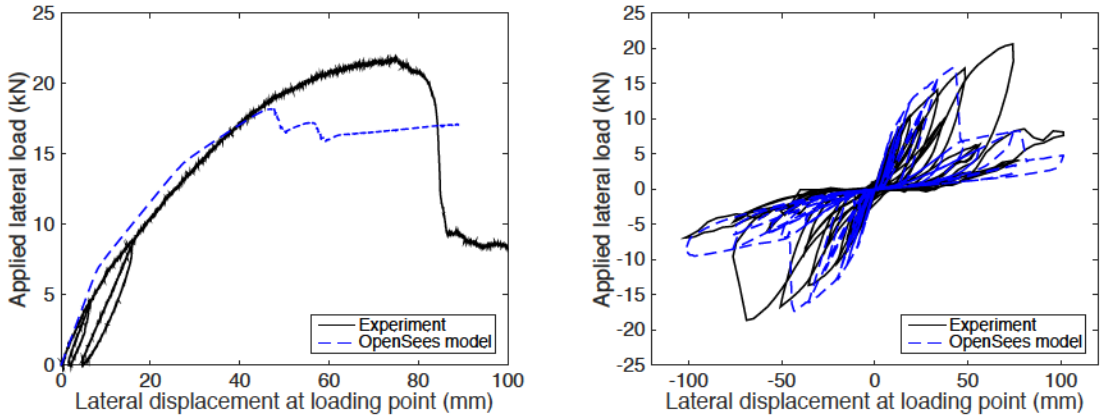

(a) monotonic (b) cyclic

Figure 4-4. Comparison of shear wall force – deformation response

4.4.2 Shear Wall Behavior at Different Gravity Levels

To demonstrate the impact of gravity load on the predicted performance of the shear wall we gradually increased the superimposed gravity load in the OpenSees model and examined the monotonic and cyclic response as a function of gravity load. For reference, the axial load capacity of the individual studs considered, P_{nl}, is provided in the final column of Table 4-2. Consistent with experimental observation it is assumed that the sheathing restricts distortional and global buckling and thus the stub column capacity converges to the fully braced local buckling result. The inputs for the Direct Strength Method of AISI S100 in the determination of P_{nl} are also provided in Table 4-2.

Table 4-2. Yielding and buckling strength for different cross sections

Cross section	F_y (MPa)	P_y (kN)	P_{crl} (kN)	P_{nl} (kN)
600S162-33	340.0	51.0	8.2	23.0
600S162-54	340.0	130.0	35.0	68.0

The shear wall lateral response under monotonic loading at different levels of superimposed gravity is provided in Figure 4-5a. The gravity load was added at the top of the chord studs only at the values of $1/4P_{nl}$, $1/3P_{nl}$, $1/2P_{nl}$, $2/3P_{nl}$ and $3/4P_{nl}$. The initial stiffness and peak load and displacement are provided in Table 4-3. As the gravity load increases, the peak strength and its corresponding displacement decrease. However, the decrease is minimal until somewhere between $2/3P_{nl}$ and $3/4P_{nl}$ when the failure mode switches from the fastener to the chord stud. The presence of this limit state near $2/3P_{nl}$ is no accident since the chord studs are capacity protected with an Ω_o of 3. This Ω_o force level is exhausted when the superimposed dead load is 2/3 of the axial capacity (P_{nl}). It is interesting to note that the model predicts a significant increase in initial stiffness for the shear walls. This is due to the superimposed gravity load allowing both chord studs to remain in compression (and thus the higher bearing stiffness as opposed to the lower stiffness based on the hold down in tension) under moderate applied loads.

Table 4-3. Monotonic lateral loading result

Gravity load level	Peak load (kN)	Disp. @ peak load (mm)	Initial stiffness (kN/mm)	Failure Location
P = 0	18.17	45.54	0.86	Fastener
P = $1/4P_{nl}$	17.04	38.21	1.61	Fastener
P = $1/3P_{nl}$	16.72	36.23	1.56	Fastener
P = $1/2P_{nl}$	15.95	35.88	1.42	Fastener
P = $2/3P_{nl}$	15.08	35.49	1.3	Stud
P = $3/4P_{nl}$	12.06	17.92	1.25	Stud

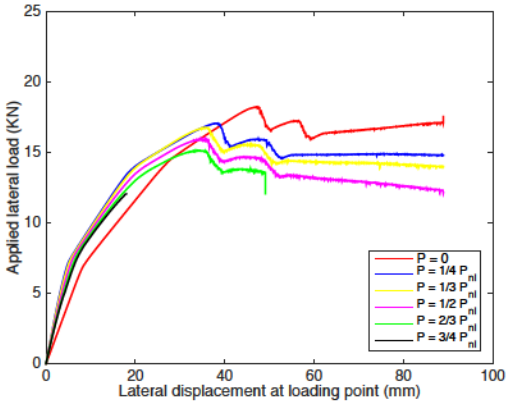

(a) shear wall monotonic response

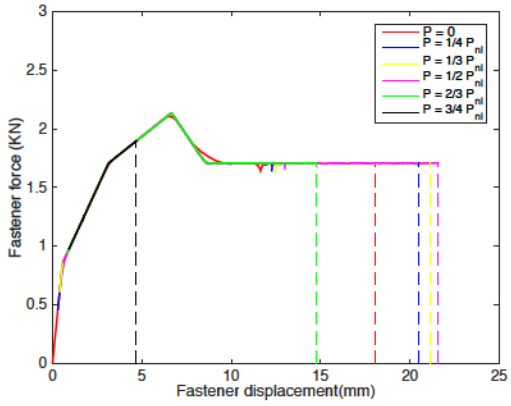

(b) worst case fastener response under loading

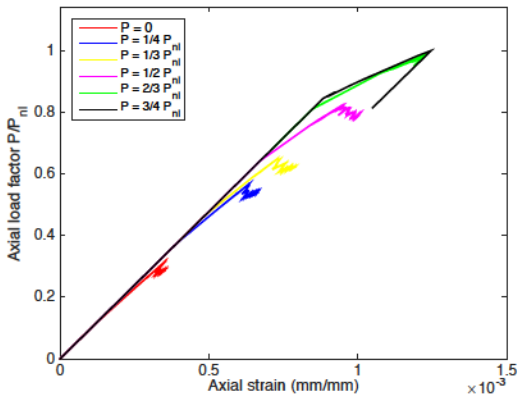

(c) chord stud axial force – strain response

Figure 4-5. Shear wall behavior under monotonic lateral loading

The fastener displacement-force curve during the monotonic loading is provided in Figure 4-5b. The selected fastener is in the bottom right corner of the shear wall, which has the largest deformation of all the fasteners. Under compression the chord stud is deformed; however the OSB board is modeled as a rigid body and thus cannot be compressed. As a result a small initial incompatibility between the framing and the OSB board exists creating an initial fastener load. All the fasteners follow the same backbone response, but the displacement at failure is demonstrably a function of gravity load. For the highest superimposed gravity load ($3/4P_{nl}$) the fastener does not reach its peak

capacity – as the chord stud failure controls the response.

The normalized axial load vs. axial strain for the chord studs is provided in Figure 4-5c for monotonic loading. When the gravity load is at $2/3P_{nl}$ or larger the axial force in chord stud gets to P_{nl} and then buckles, following the Pinching04 response defined in Section 2.2. The results indicate that the model is capable of capturing both fastener-based and member-based limit states and that at high enough gravity load this may be important.

Figure 4-6 provides the results of the shear wall response under cyclic (CUREE protocol) loading. The basic monotonic results as gravity load is increased hold true in the cyclic response: there is an increased stiffness at low force levels, the peak force and displacement decrease modestly until chord stud failure occurs, chord stud failure at high superimposed axial loads significantly limits the response. New phenomena also emerge: the response moves into the 2nd and 4th quadrant even though the model is fully pinched at no axial load, and numerical convergence under high axial load becomes challenging. Additional study is needed to explore these new observations and challenges.

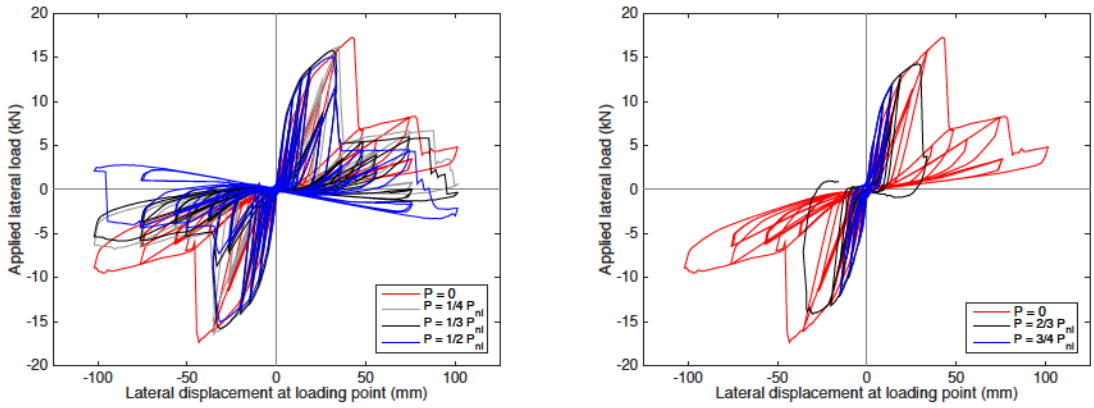

(a) response for low superimposed axial load

(b) response for high axial load

Figure 4-6. Shear wall behavior under cyclic lateral loading

4.4.3 Shear Wall Behavior with Different Thickness Chord Studs

In the preceding study we considered the superposition of a large gravity load and commented on the fact that at high enough gravity load the seismic design using Ω_o=3 is eventually exhausted. Another option considered for exploring the impact of the chord studs on the response is to begin with a chord stud that has 1/3 the initial capacity. As Table 4-2 indicates the stud nominal strength P_{nl} decreases by almost exactly a factor of 3 as the stud thickness is reduced from 1.37 mm [54mil] to 0.84 mm [33mil]. However, when the stud thickness is changed the sheathing fastener response also changes, since it is a function of the thickness of steel it is anchored into, and thus the change is not as simple as decreasing only the stud capacity and response.

The monotonic shear wall response with 1.37 mm [54mil] and 0.84 mm [33mil] chord studs and fastener properties is provided in Figure 4-7a. For comparison an additional analysis was conducted where the 0.84 mm [33mil] fastener properties were employed,

but still the 1.37 mm [54mil] chord stud properties were employed. This results is essentially coincident with the case when the fastener and chord stud are modified, indicating that the change in the fastener response, not the change in the axial stud response, dominates. In the studied case the thinner chord stud influences the response, but only through the fastener, not because it has a reduced axial response. This is borne out in the Figure 4-7b cyclic response as well. Further examination under superimposed gravity load is possible and desirable, but has been conducted at this time.

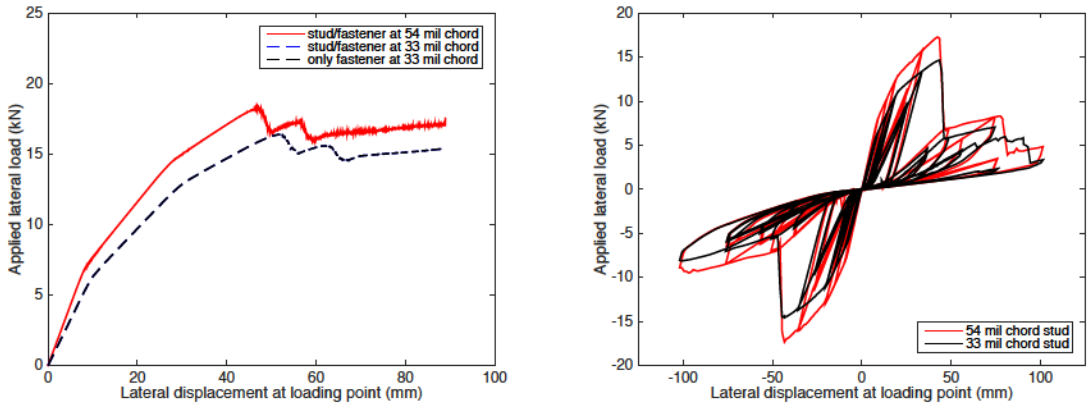

Figure 4-7. Shear wall behavior with different stud thickness under: (a) monotonic loading; (b) cyclic loading

4.4.4 Discussion on Failure Mode in ABAQUS Model

In addition to pursuing efficient fastener-based models in OpenSees we have also been pursuing high fidelity simulations in ABAQUS. In OpenSees the cold-formed steel framing (stud, ledger or track) is modeled using displacement-based beam-column elements. Such elements assume rigid cross-sections and do not allow for localized plate flexibility in the cold-formed steel framing. In addition, in the benchmark shear wall testing the OSB sheathing is attached to one face of the studs and the ledger track to the

opposite face. These eccentricities are not included in the OpenSees model. To explore these effects a primarily shell element based shear wall model was developed in ABAQUS.

The model was developed based on the previous work (Ngo 2014; Bian et al. 2014). The CFS framing members and sheathing are modeled as four-node shell finite elements (S4R in ABAQUS). A relatively coarse mesh is used for the oriented strand board (OSB) sheathing, which is modeled as elastic but stiff (currently with E=207,000 MPa [30,000 ksi] and μ=0.3) to minimize diaphragm deformations. The CFS frame (steel-to-steel) connections are modeled as pinned by means of MPC constraints in ABAQUS. The steel-to-sheathing connections are modeled as Spring-A elements with the same backbone curve as used in OpenSees. The final result is a model that is similar to the OpenSees model in many ways, but which includes a full and accurate three-dimensional treatment of the framing.

Figure 4-8a and b provide the comparison of load-displacement result between OpenSees and ABAQUS for 0.838 mm [33mil] and 1.371 mm [54mil] thickness chord stud. The result shows that the OpenSees and ABAQUS results agree well with one another.

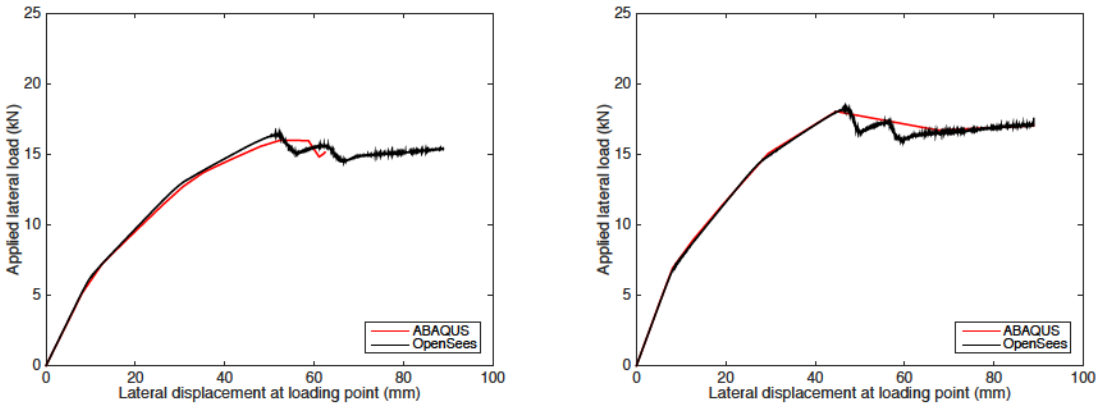

(a) 0.84 mm [33mil] chord stud models (b) 1.37 mm [54mil] chord stud models

Figure 4-8. Shear wall modeling result in ABAQUS compared with OpenSees

Figure 4-9a and b provide the deformation of the shear wall under monotonic loading. The deformation indicates a modest amount of torsion in the studs, although it does not decrease the shear wall lateral resistance capacity significantly in the studied case.

(a) (b)

Figure 4-9. Shear wall deformation in ABAUS

4.5 Discussion and Future Work

The work presented herein provides an efficient model implemented in OpenSees with two potential nonlinear limit states for wood sheathed CFS-framed shear walls: damage at fastener locations, or local buckling of chord studs. Results are provided where at high

levels of superimposed dead load the dominant failure changes from fastener damage to chord stud buckling; however the model has convergence issues that require additional investigation. In addition, initial models using a weaker (0.84 mm [33mil]) chord stud for the shear walls need to be completed at different absolute levels of superimposed dead load to demonstrate the impact of gravity load on weaker chord studs. Formal shear wall design utilizes Ω_o to capacity protect the chord studs – evaluation of archetypical shear wall designs at different levels of Ω_o using the developed OpenSees model would provide a beneficial means to understand the impact of this assumption in seismic design. Addition of superimposed gravity load to the higher fidelity ABAQUS model such that chord stud buckling is initiated and comparison between the two models would be useful. Incorporation of other limit states (hold downs, shear anchors, etc.) would also be beneficial. Monte Carlo simulation utilizing the OpenSees model for reliability simulation would potentially better show the power of including multiple limit states within the model itself and help to develop more rational resistance factors for these systems. Incorporation of gravity walls in the OpenSees model has the potential to efficiently provide insights on the large overstrength often realized in these systems and additionally provides a direct path to robust, accurate, and efficient full-scale building modeling – the long-term goal of this research.

4.6 Conclusion

Wood sheathed cold-formed steel framed shear walls may be efficiently modeled in OpenSees and provide full nonlinear hysteretic response based on damage at stud-to-sheathing connectors or due to chord stud buckling. This provides engineers with an efficient solution that can predict the shear-deformation response of these shear walls

under a multitude of different details and incorporating the two most important limit states. The provided model is an extension of previous work that focused on nonlinearity at the stud-to-sheathing connectors. Here nonlinearity is extended to the chord studs and shear wall models are provided that demonstrate the impact of this inclusion. In particular, the impact of the switch of limit states in a shear wall from fastener-based damage to chord stud buckling at very high levels of superimposed dead load is demonstrated. Verification of the developed model is provided by comparison with experiments and a higher fidelity shell element based model; however, additional verification is needed. Significant additional work remains to utilize the model more formally in seismic shear wall design, to better understand system reliability, and in full building models. Nonetheless, the model represents a significant advancement for efficient computational modeling of cold-formed steel framed shear walls and has wide potential application.

4.7 Acknowledgement

This research was conducted as part of the U.S. National Science Foundation sponsored project "GOALI/Collaborative Research: Advancing System Reliability with Application to Light-Framed Structures" (NSF-CMMI-1300484). This project is in collaboration with the American Iron and Steel Institute. Any opinions, findings, and conclusions or recommendations expressed in this publication are those of the author(s) and do not necessarily reflect the views of the National Science Foundation or the American Iron and Steel Institute.

4.8 References

[1] AISI-S100-12. (2012). "North American Specification for the Design of Cold-Formed Steel Structural Members" American Iron and Steel Institute, Washington (DC).

[2] AISI-S213-07. (2007). "AISI North American Standard For Cold-Formed Steel Framing - Lateral Design." American Iron and Steel Institute.

[3] Bian, G., Buonopane, S., Ngo, H., and Schafer, B. (2014). "Fastener-Based Computational Models with Application to Cold-Formed Steel Shear Walls." *Proceedings of the 22nd International Specialty Conference on Cold-Formed Steel Structures.,* St. Louis, Missouri, USA, 825-840.

[4] Branston, A., Boudreault, F., Chen, C., and Rogers, C. (2006). "Light-gauge steel-frame wood structural panel shear wall design method." *Canadian Journal of Civil Engineering,* 33(7), 872-889.

[5] Buonopane, S., Tun, T., and Schafer, B. (2014). "Fastener-based computational models for prediction of seismic behavior of CFS shear walls." *Proceedings of the 10th National Conference in Earthquake Engineering,* .

[6] Folz, B., and Filiatrault, A. (2001). "Cyclic analysis of wood shear walls." *J.Struct.Eng.,* 127(4), 433-441.

[7] Liu, P., Peterman, K., and Schafer, B. (2014). "Impact of construction details on OSB-sheathed cold-formed steel framed shear walls." *Journal of Constructional Steel Research,* 101 114-123.

[8] Liu, P., Peterman, K. D., and Schafer, B. W. (2012). "Test Report on Cold-Formed Steel Shear Walls." *Rep. No. RR03,* CFS-NEES, .

[9] Lowes, L. N., Mitra, N., and Altoontash, A. (2003). *A beam-column joint model for simulating the earthquake response of reinforced concrete frames.* Pacific Earthquake Engineering Research Center, College of Engineering, University of California, .

[10] Mazzoni, S., McKenna, F., Scott, M. H., and Fenves, G. L. (2003). "Open System for Earthquake Engineering Simulation User Command-Language Manual." Berkeley, California.

[11] Ngo, H. (2014). "Numerical and experimental studies of wood sheathed cold-formed steel framed shear walls." M. Eng. Thesis, Department of Civil Engineering, John Hopkins University, Baltimore, MD, USA, 2014.

[12] Padilla-Llano, D., Moen, C., and Eatherton, M. (2015). "OpenSees simulation of steel column axial cyclic response including local buckling." *Proceedings of 2015 SSRC Annual Stability Conference,* SSRC 2015, Nashville, Tennessee.

[13] Padilla-Llano, D. A., Moen, C. D., and Eatherton, M. R. (2013). "Energy Dissipation of Thin-walled Cold-formed Steel members." *Rep. No. CE/VPI-ST-13/06,* VIRGINIA POLYTECHNIC INSTITUTE AND STATE UNIVERSITY.

[14] Peterman, K. D., and Schafer, B. W. (2013). "Hysteretic shear response of fasteners connecting sheathing to cold-formed steel studs." *Rep. No. RR04,* CFS-NEES, .

[15] Peterman, K., Nakata, N., and Schafer, B. (2014). "Hysteretic characterization of cold-formed steel stud-to-sheathing connections." *Journal of Constructional Steel Research,* 101 254-264.

[16] Shamim, I., and Rogers, C. (2012). "Numerical Modeling and Calibration of CFS framed shear walls under dynamic loading." *Proceedings of the 21st International Specialty Conference on Cold-Formed Steel Structures,* 24-25.

[17] Simulia. (2012). " ABAQUS/CAE User's Manual " 6.12.

CHAPTER 5

OPENSEES MODELING OF COLD-FORMED STEEL FRAMED GRAVITY WALL

5.1 Abstract

The objective of this chapter is to present and explore an efficient spring-element-based finite element model of a wood sheathed cold-formed steel framed wall system. The model is developed in OpenSees and has the potential to be an important building block tool for modeling full structures framed with cold-formed steel. The lateral stiffness of the gravity wall is currently ignored in both the design and modeling of multi-story cold-formed steel (CFS) framed building. However, full-scale experimental work on a two-story cold-formed steel (CFS) framed buildings, as part of the CFS-NEES effort, shows that gravity walls can provide a contribution to the lateral response and potentially should be considered in the design of lateral force resisting systems. Recently an engineering model implemented in OpenSees employing fastener-based characterization as the essential nonlinearity in a CFS framed shear wall has shown that OpenSees models are capable of predicting full shear wall hysteretic performance. In the work presented here, the fastener-based shear wall model is extended to provide a model capable of capturing coupled shear wall and gravity wall behavior in a wall system. The contribution of gravity walls on lateral resistance is explored by comparing the wall system behavior with and without gravity walls. The model provides practical design advantages and also a means to model the lateral system resistance in CFS framed buildings.

5.2 Introduction

Cold-formed steel (CFS) structures are commonly used for low and mid-rise construction. Often wood sheathing, such as oriented strand board, is screw-fastened to the cold-formed stud and track framing to develop shear stiffness as well as strength in the wall system. The North American Standard for Cold-formed Steel Framing – Lateral Design (AISI S213-07) provides CFS-framed specific shear wall strength based on the type and thickness of sheathing, aspect ratio, fastener spacing, stud and track thickness, and screw size.

In AISI S213-07, shear walls are classified either as those with hold downs installed at the end of each wall segment (type I), or those with detailing for force transfer around openings (type II). Type I shear walls are laterally decoupled, rocking back and forth as individual walls under a lateral load. Type II shear walls are laterally coupled and thus behave as one whole wall. In line with the shear walls are the gravity walls, another important component of a CFS structure that is designed to carry vertical load from the upper levels of the building. The fastener spacing, stud type and connection to foundation are the main differences between shear walls and gravity walls. Hold downs are only installed at the bottom of the shear wall chord studs (see Figure 5-1a). There is no direct connection between gravity studs and the foundation. The bottom track for both shear walls and gravity walls are restrained horizontally at the floor by simple connectors to the foundation such as low velocity fasteners (see Figure 5-1c). In ledger framing, a ledger or carrier track is used to carry the floor joists and in turn connects together all wall

segments (as it is fastened to the wall studs) and acts as a collector between the shear walls (see Figure 5-1b).

Figure 5-1. Cold-formed steel wall details

In current cold-formed steel building design, only the shear wall is designed to carry lateral load, and lateral resistance for the gravity wall is neglected. As part of the NSF-funded CFS-NEES effort, testing of two full-scale cold-formed steel framed buildings under seismic excitation at the University at Buffalo Structural Engineering Earthquake Simulation Lab was performed in the summer of 2013. From the observations of the test (Peterman 2014), gravity elements such as window headers and framing could transfer lateral forces between shear walls. Furthermore walls designed as type I shear walls were observed to perform as type II shear walls. The test also showed that as nonstructural components were added to the test specimen, the natural period decreased significantly. The result of 3D simulation of the CFS-NEES building (Leng et al. 2013) concurred, and

models without gravity walls and non-structural components had significantly larger natural period than the models with them.

Buonopane et al. (2014) developed a series of OpenSees models that employed fastener test data from Peterman et al (2013) and demonstrated that the basic elastic and full non-linear cyclic response of the shear walls could be predicted utilizing fastener-based models. In this chapter, the fastener-based shear wall model was extended to a wall system including both a shear wall and gravity wall. For this series of models, results such as base shear and hold down force distribution are explored, and their stiffness and strength are compared.

5.3 Description of Numerical Models in OpenSees

The model developed in this work is implemented in OpenSees (i.e., the Open System for Earthquake Engineering Simulation (Mazzoni et al. 2003)). OpenSees provides efficient solvers for earthquake building simulation and is widely used in seismic simulations. OpenSees derives much of its efficiency from primarily being a frame element based code, and provides an extensive library of phenomenological based models. This section provides the details for the OpenSees-based wall modeling developed in this chapter.

5.3.1 Material and Element for Single Shear Wall Model

A typical OSB-sheathed, CFS-framed shear wall from the testing of Liu et al. (2014) is selected as the benchmark shear wall model in this chapter (see Figure 5-2). The shear wall is combined with different configurations of gravity walls to comprise different wall systems. The primary dimensions of the shear wall are 1.22 m [4 ft.] wide by 2.74 m [9 ft.] high. The shear wall is framed with 600S162-54 studs, 11.11 mm [7/16 in.] OSB on

one face, using #8 fasteners at 152.4 mm [6 in.] spacing in the perimeter and 304.8 mm [12 in.] spacing in the field connecting the OSB to the CFS framing. A 1200T200-97 ledger was fastened to the back side of the frame at the top of the shear wall. At the base, Simpson S/HDU6 hold-downs are connected to the chord studs, and 15.88 mm [5/8 in.] diameter bolts through the bottom track to the foundation (HSS section) . At the top, #10 38.1 mm [1 ½ in.] self-drilling screws spaced at 76.2 mm [3 in.] connect through the top track to the loading beam.

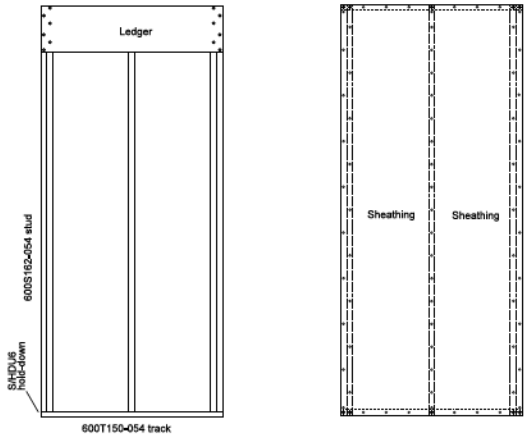

Figure 5-2. Benchmarked CFS shear wall

The CFS framing members, including the stud and tracks, are subdivided into 20 and 8 displacement based beam-column elements respectively, with nodes at each fastener location. Linear elastic material and beam-column elements were used to model the stud and tracks. Rotational springs were used to connect the studs and top/bottom tracks (See Figure 5-3). Stiffness for the rotational spring is set as 113 KN-m/rad [100 kip-in./rad] based on approximations from the measured lateral stiffness of bare CFS frame tests (Buonopane et al. 2014). The sheathing board was modeled as a rigid diaphragm with

slave nodes at each fastener location and a master node at the center of the sheathing board.

The ledger was modeled with a displacement based beam-column element with fixed degrees of freedom at the ledger-stud connections. This rigid offset transferred deflection from the studs to the ledger. For simplification, the sheathing is modeled as single rigid diaphragm, neglecting the horizontal seam that is presented in the physical tests.

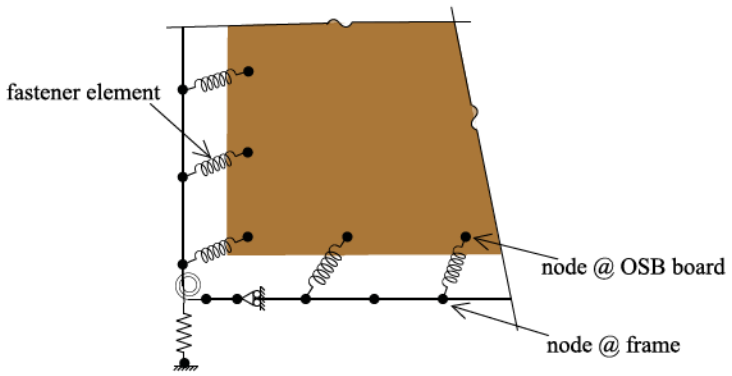

Figure 5-3. CFS shear wall model in OpenSees

Two nodes with fixed degrees of freedom were used as the foundation. Zero-length elements connecting foundation nodes and two bottom nodes at the chord studs were modeled as hold-downs. Based on Simpson Strong-Tie published values of tensile strength and displacement, tensile stiffness for the hold-down of 9.9 kN/mm [56.7 kips/in] was selected while the compressive stiffness of the hold down was modeled as 1000 times larger to simulate bearing against a rigid foundation. The translational degrees of freedom of the shear wall at two bottom-track nodes were fixed to simulate the shear anchors at these locations (See Figure 5-3).

At fastener locations, the nodes of the frame members and the sheathing coincide. As shown in Figure 5-3, these nodes are connected using zero-length springs. Pinching04 was assigned as the material model for the zero-length fastener elements. The parameters required to define the Pinching04 uniaxial material in OpenSees, which includes the backbone curve, degradation factors, and other force and displacement relation parameters, are estimated from separate physical testing of the fasteners as reported by Peterman and Schafer (2013).

5.3.2 Modeling of Gravity Wall and Wall System

There are different possible combinations of gravity wall and shear wall in CFS wall system. In this chapter five different wall combination scenarios were modeled, as shown in Table 5-1. The shear wall and gravity wall configurations are provided in Figure 5-4. The sheathing material of the shear wall is either OSB (in scenarios 1, 2 and 3) or OSB and gypsum (in scenario 4). The gravity wall consists of bare frame, frame + OSB, or frame + gypsum (scenarios 1, 2 and 3, respectively), or a combination frame + OSB + gypsum (scenario 4). Wall scenario 0 represents the isolated OSB sheathed shear wall model without the gravity wall.

Table 5-1. Model matrix for CFS wall system

Wall Scenario	Shear wall		Gravity wall		
	OSB	Gypsum	Bare frame	OSB	Gypsum
0	×				
1	×		×		
2	×		×	×	
3	×		×		×
4	×	×	×	×	×

The gravity wall is composed of OSB and/or gypsum board fastened to cold-formed steel framing, but with twice the fastener spacing as in the shear wall. There is no hold down at the bottom of the gravity wall studs so the tensile stiffness for the connection between studs in gravity wall and foundation is small. A similar fastener-based model was utilized for modeling gravity walls. Number eight (#8) fasteners at 304.8 mm [12 in.] spacing in the perimeter were used in gravity walls. Different fastener models were selected for gypsum and OSB connections according to separated fastener test (Peterman et al. 2014). For simplicity, contact between the sheathing panels within the shear wall and gravity walls were not considered.

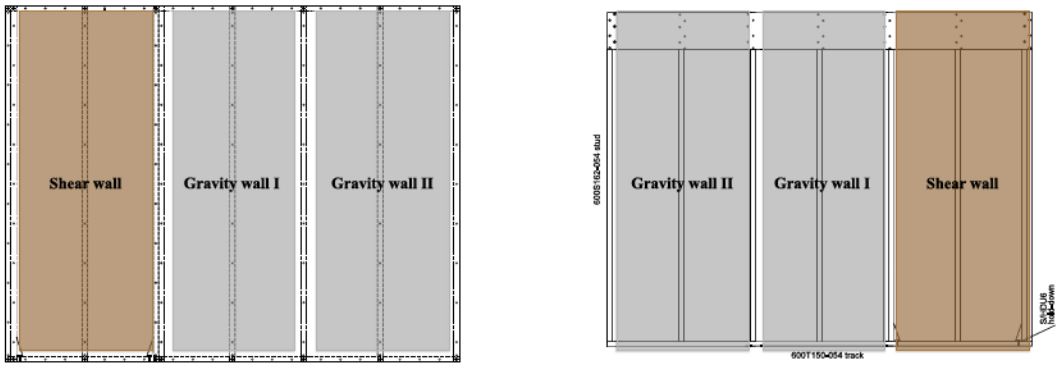

(a) (b)

Figure 5-4. Wall system configuration: (a) exterior side; (b) interior side

The wall system was assumed horizontally restrained at the bottom track by low velocity fasteners as in the CFS-NEES building. For the gravity wall, large compressive stiffness, analogous to the hold down in the shear wall, was assigned for the stud bottom to model the bearing between gravity wall and foundation. Since the flexural stiffness of the bottom track between two low velocity fasteners is small, tensile stiffness for the connection between studs and foundation was defined as the flexural stiffness of the bottom track between two low velocity fasteners, given by

$$k = \frac{48EI}{b(3L^2 - 4b^2)} \tag{5-1}$$

where I is the moment of inertia about weak axis bending for bottom track; b is distance between the stud and LVF at one side and L is the distance between two low velocity fasteners. The distance between two LVFs is 609.6 mm [24 inches] and 1219.2 mm [48 inches] and twice the LVF distance is used to account for the high probability that at least one LVF is inadequate in tension. Under these assumptions the tensile stiffness at a bottom of a gravity wall stud is 1.1 kN/mm [6.28 kip/in] or 1/10th the hold down stiffness.

5.4 Modeling results and discussion

In this section shear-deformation responses were obtained for different wall models. Based on the results, peak load and stiffness were compared for different wall system scenarios. Furthermore, base shear and hold down force distribution at shear wall and gravity walls were explored.

5.4.1 Load-Displacement Curve for Wall Systems

Figure 5-5 provides the shear load-displacement curve for different wall systems. The stiffness and peak load capacity increase significantly when gravity walls, especially those with OSB and/or gypsum board, were added to the shear wall. Although the tensile stiffness for the connection between a gravity wall stud and the foundation was small, the direction of the shear deformation (left vs. right) is not observed to have a significant difference in terms of lateral stiffness.

Stiffness and peak lateral load capacity for the different wall models are provided in Table 5-2. Stiffness was obtained as the secant stiffness at the peak load and its relative displacement. The single OSB shear wall can carry 20 kN lateral load while the combination of shear wall and gravity wall with both OSB and gypsum is 65 kN. The lateral resistance for gravity walls with OSB is significantly larger than that with gypsum board since the fastener behavior differs significantly for these different materials.

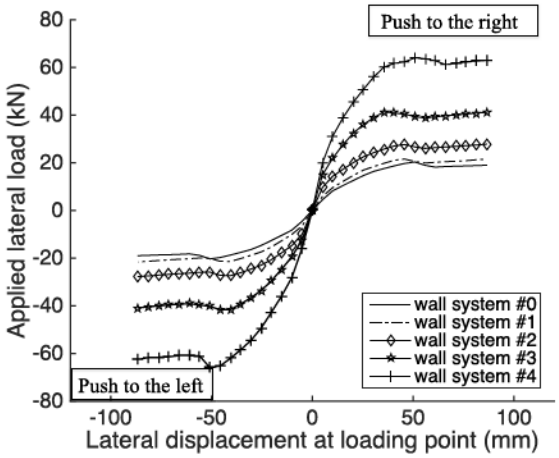

Figure 5-5. Lateral load-displacement curve for wall models

Models were created of the shear wall (SW) alone, gravity wall (GW) alone, and the SW+GW in series similar to Figure 5-4. The lateral capacity for the combination of shear wall and gravity wall is almost equal to the addition of their separate peak load, which means that the model produces walls essentially as a parallel system for strength, i.e., summing the shear wall and gravity wall resistance. The secant stiffness at peak shear of the coupled wall model (SW+GW) can also be approximated by adding shear wall and gravity wall stiffness.

5.4.2 Reaction Force for Wall System

An external lateral force on the wall generates base shear at the bottom track and tension/ compression force at hold downs and the bottom of studs The moment from the shear force at the track and from the axial force at the stud ends are balanced in equilibrium in the wall system.

Table 5-2. Peak load and stiffness for wall system models

lateral loading to right									
	P_{max} (kN)			$\delta@P_{max}$ (mm)			Stiffness K		
	SW+GW	SW	GW	SW+GW	SW	GW	K_{all}	K_{SW}	K_{GW}
Wall system #1	21.70	20.35	1.69	44.79	50.91	44.79	0.48	0.40	0.04
Wall system #2	41.88	20.35	22.02	37.97	50.91	54.06	1.10	0.40	0.41
Wall system #3	27.70	20.35	7.02	44.44	50.91	43.68	0.62	0.40	0.16
Wall system #4	64.53	25.19	27.22	53.56	55.07	59.77	1.20	0.46	0.46

lateral loading to left									
	P_{max} (kN)			$\delta@P_{max}$ (mm)			Stiffness K		
	SW+GW	SW	GW	SW+GW	SW	GW	K_{all}	K_{SW}	K_{GW}
Wall system #1	21.72	20.35	1.62	42.91	50.75	42.91	0.51	0.40	0.04
Wall system #2	42.13	20.35	22.02	43.26	50.75	53.43	0.97	0.40	0.41
Wall system #3	27.70	20.35	7.02	43.68	50.75	43.68	0.63	0.40	0.16
Wall system #4	66.55	25.19	27.22	49.66	55.07	59.77	1.34	0.46	0.46

Wall model #3 (SW with OSB + GW with Gypsum) was selected as a representative case to provide the reaction force information. Figure 5-6 provides wall deformation, axial force at the bottom of the studs and base shear for this model. When the wall was sheared to the left, only the left hold down experienced compression force. The gravity wall carries small tensile forces along its length, the largest of which is at the shared chord stud of the shear wall, which provides the larger tension stiffness of the hold down. When the wall was sheared to the right, hold downs in the shear walls experienced tension at the bottom of the studs while the gravity wall was under compression (i.e. the classic Type II shear wall behavior even though the only hold downs are at the shear wall). The force value at the bottom of each stud is provided in Table 5-3. The hold down forces are always the greatest but the forces in the other locations are consequential. The shear wall

and gravity walls deform together, to the same direction, and with very similar magnitude.

Table 5-3. Hold down force in wall model #3

		shear wall		gravity wall				
		stud1	stud2	stud3	stud4	stud5	stud6	stud7
Right lateral loading	value at peak load (kN)	36.51	1.93	1.41	-5.78	-4.92	-5.58	-23.57
	tension/compression	tension	tension	tension	compression	compression	compression	compression
Left lateral loading	value at peak load (kN)	-52.57	0.73	18.72	3.93	6.27	9.40	13.52
	tension/compression	compression	tension	tension	tension	tension	tension	tension

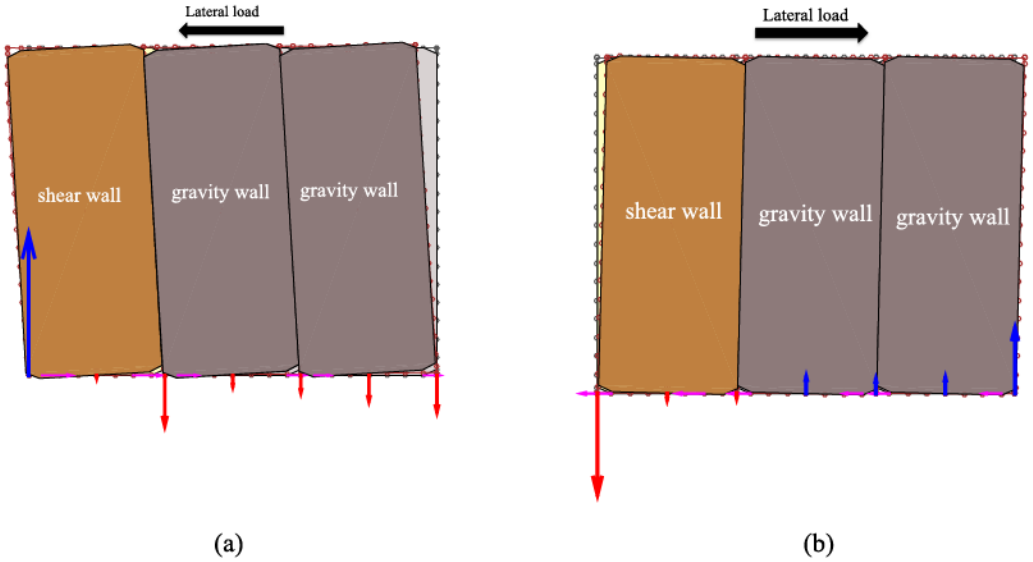

(a) (b)

Figure 5-6. Deformed shape and reaction force for the shear wall with OSB gravity wall: (a) left side push; (b) right side push

Base shear at the bottom track is provided in Table 5-4 for model 3. There are two low velocity fasteners in the shear wall segment and four in the gravity walls. Although there is no hold down in the gravity wall studs and the stud ends have only 1/10th the tensile stiffness, the gravity wall does have twice the length and the large number of fastener locations make the gravity wall carry most of the base shear. The sum of the last four base shear columns, which is the base shear carried by gravity wall, is over half of the total force.

Table 5-4. Base shear at bottom track in wall model #3

		shear wall		gravity wall			
		LVF1	LVF2	LVF3	LVF4	LVF5	LVF6
Right lateral loading	value at peak load (kN)	-9.68	-8.75	-6.38	-5.72	-5.63	-5.66
	Percentage	23.1%	20.9%	15.3%	13.7%	13.5%	13.5%
Left lateral loading	value at peak load (kN)	9.88	9.33	6.43	5.66	5.27	5.46
	Percentage	23.5%	22.2%	15.3%	13.5%	12.5%	13.0%

5.5 Discussion and Future Work

The work presented herein provides an efficient model implemented in OpenSees for wood sheathed CFS-framed wall combination. Results are provided for different configurations of shear walls and gravity walls. There are many other kinds of wall configurations in CFS buildings that may be obtained by changing the relative location of shear wall and gravity wall and other details including openings. Work remains to explore different configurations for the wall models. In a previous work, the authors utilized an element with Pinching04 material for shear wall chord studs, which can estimate the stud buckling failure. Addition of superimposed gravity load to the wall model such that the chord stud buckling is initiated in this model could also be useful. Using the fastener-based wall model to calibrate simplified truss element-based shear panel models may also be beneficial. For modeling complex 3D CFS buildings, incorporation of wall models-based on truss elements has the potential to efficiently provide a direct path to robust, accurate and efficient full-scale building modeling.

5.6 Conclusions

Wood sheathed cold-formed steel framed wall systems may be efficiently modeled utilizing a fastener-based model in OpenSees. This provides engineers with an efficient solution that can predict the shear-deformation response for different shear wall and gravity wall combinations. The provided model in this chapter is an extension of previous

work that focused on shear walls alone. Here the extended wall model demonstrates the impact of gravity walls on the lateral wall system performance. In the studied example the gravity wall can carry as much as half of the lateral force, although it is not accounted for in the design process. Significant additional work remains to extend the model to more wall configurations and utilize the model more formally in seismic shear wall design, to better understand system reliability, and in full building models. Nonetheless, the model represents a significant advancement for efficient computational modeling of cold-formed steel framed walls and has wide potential application.

5.7 Reference

[1] AISI-S213-07. (2007). "AISI North American Standard For Cold-Formed Steel Framing - Lateral Design." American Iron and Steel Institute.

[2] Peterman, K. D. (2014). "Behaviour of full scale cold-formed steel buildings under seismic excitations." Ph.D. thesis. Johns Hopkins University.

[3] Leng, J., Schafer, B., and Buonopane, S. (2013). "Modeling the seismic response of cold-formed steel framed buildings: model development for the CFS-NEES building." Proceedings of the Annual Stability Conference - Structural Stability Research Council, St. Louis, Missouri.

[4] Buonopane, S., Tun, T., and Schafer, B. (2014). "Fastener-based computational models for prediction of seismic behavior of CFS shear walls." Proceedings of the 10th National Conference in Earthquake Engineering.

[5] Bian, G., Buonopane, S., Ngo, H., and Schafer, B. (2014). "Fastener-Based Computational Models with Application to Cold-Formed Steel Shear Walls." Proceedings of the 22nd International Specialty Conference on Cold-Formed Steel Structures. St. Louis, Missouri, USA, 825-840.

[6] Mazzoni, S., McKenna, F., Scott, M. H., and Fenves, G. L. (2003). "Open System for Earthquake Engineering Simulation User Command-Language Manual." Berkeley, California.

[7] Liu, P., Peterman, K., and Schafer, B. (2014). "Impact of construction details on OSB-sheathed cold-formed steel framed shear walls." Journal of Constructional Steel Research, 101 114-123.

[8] Peterman, K., Nakata, N., and Schafer, B. (2014). "Hysteretic characterization of cold-formed steel stud-to-sheathing connections." Journal of Constructional Steel Research, 101 254-264.

CHAPTER 6

RELIABILITY OF COLD-FORMED STEEL FRAMED SHEAR WALLS AS IMPACTED BY VARIABILITY IN FASTENER RESPONSE

6.1 Abstract

The objective of this chapter is to examine the reliability of cold-formed steel framed shear walls with a particular emphasis on walls sheathed with wood structural panels. A sheathed cold-formed steel framed shear wall is a system consisting of studs, tracks, and sheathing often with bridging and/or blocking, connected with steel-to-steel and sheathing-to-steel fasteners. The shear walls may be integrally connected to foundations, floors, or other shear walls through a variety of means including hold downs, straps, diaphragm chords and collectors. Shear wall lateral resistance in cold-formed steel framed buildings varies because of the randomness in the components and connections that comprise the wall. The interaction between fasteners and sheathing is particularly important because (1) sheathing-to-steel fastener response is the main source of shear wall nonlinearity (2) there is high variability in this fastener response. Although the nominal strengths for different shear wall configurations are stated in current design specifications (e.g., AISI S400), variability of shear walls has not been explicitly considered. Existing resistance factors are extrapolations from steel diaphragm testing. To explore the impact of fastener response variability on shear wall reliability, Monte Carlo simulation of typical cold-formed steel framed wood sheathed shear walls with random fastener input was conducted. Variability in fasteners was determined based on

existing physical fastener tests. Statistical properties of shear wall strength, demand capacity ratio of key fasteners, as well as relations between fastener strength and shear wall strength are all explored. Reliability evaluation is provided for four different design methods. The results indicate that shear wall strength benefits from a system effect whereby variability in fastener response is reduced through redistribution resulting in reduced variability in overall shear wall strength. Concomitant with this is a slight decrease, approximately 3%, in the mean system strength that also must be considered.

6.2 Introduction

Cold-formed steel (CFS) structural systems are commonly used for low and mid-rise construction. In the design of CFS-framed buildings, shear walls are typically used to provide lateral resistance for seismic or wind load (e.g., see Figure 6-1). Commonly, wood sheathing, such as oriented strand board (OSB), is screw-fastened to CFS studs and tracks to develop lateral shear stiffness and strength (e.g., see Figure 6-2).

Figure 6-1. CFS-NEES building and shear wall in it

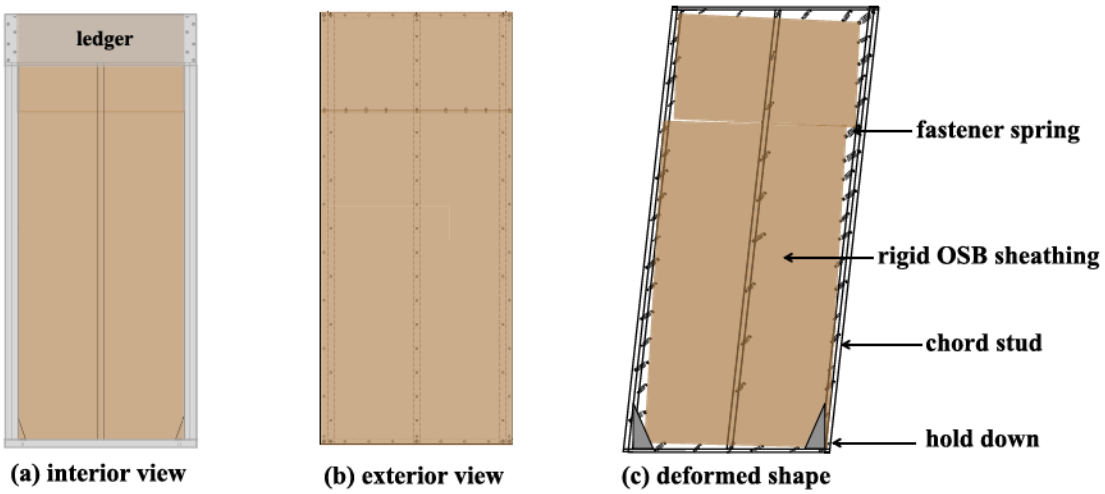

Figure 6-2. Typical cold-formed steel framed shear wall in a ledger-framed building

As the wall is sheared an incompatibility exists between the CFS framing, which is largely deforming as a parallelogram, and the wood sheathing that remains nearly rectangular and primarily undergoes rigid body translation and rotation because of its large in-plane rigidity. The incompatibility between the deformed frame and sheathing causes a relative displacement that must be accommodated at the fasteners. This displacement causes tilting and bending of the fastener, as well as deformation and damage to the steel and wood sheathing material around the fastener. This damage is the source of yielding and energy dissipation in these systems [1,2]. The resulting overall CFS-framed wood-sheathed shear wall cyclic response exhibits significant hysteresis, degradation, and pinching, as shown in Figure 6-3.

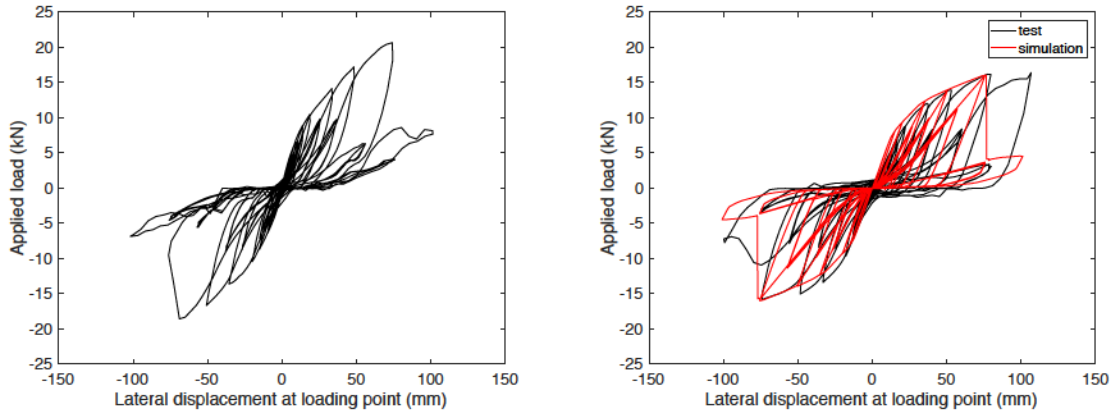

a. typical experimental response (adapted from [1])

b. comparison between experiment and determinate simulation (adapted from [2])

Figure 6-3. CFS-framed wood sheathed shear wall cyclic response

CFS-framed wood-sheathed shear walls have been tested extensively. In North America AISI S400-15 [3] (previously AISI S213-07 and -12 [4]) provides nominal shear wall strength for different types of sheathing, fastener spacing, and stud and track thickness based on the available testing (e.g., see [5,6]). The shear wall strengths in AISI S400 are based directly on tested capacities, and a ϕ=0.6 is used for the resistance factor in design. This value was selected initially based on typical ϕ value for steel deck diaphragms (which is based on a connector failure limit state and a target reliability, β, of 3.5) and has remain unchanged as additional entries to the tables in the standard have been included.

CFS-framed shear walls may be viewed as a small structural system – and system reliability for steel structures in general [7] and CFS structures in particular [9] has been studied recently. Monte Carlo (MC) simulation of models of steel frames have been used to assess component vs. system reliabilities and explore system-level resistance (ϕ) factors based on target system reliabilities as opposed to component reliability [8] . It has

been shown that the system reliability of typical CFS framing under gravity demands far exceeds the individual component reliabilities [9]. Also, the reserve strength of CFS CFS-framed floor diaphragms when considered as a system has been calculated [10]. .

Recognizing the central role that the nonlinear response of the steel-fastener-sheathing connection has on the overall shear wall response Buonopane et al. developed and validated an OpenSees simulation that adequately predicts CFS-framed wood-sheathed shear wall cyclic response [11]. This model provides the potential to conduct MC simulation of CFS-framed shear walls and explore the variability and reliability of their response. This has the potential to provide improvements to the current reliability assessment in AISI S400 [3] , which is essentially based on engineering judgment alone.

The work herein employs the validated shear wall model of Buonopane et al. [11] , the shear wall tests of Liu et al. [1], and steel-fastener-sheathing connection tests of Peterman et al. [12] to perform MC simulations on a series of CFS-framed shear walls and assess the predicted reliability of the studied shear walls. The fastener testing is characterized in terms of a random variable and used to drive MC simulation of the selected shear walls. The simulation results are summarized and explored to provide insight on the importance of load redistribution, fastener location, and the resulting variability of shear wall strength. Next, the reliability of the peak strength based on the MC simulations is determined. Finally four potential shear wall design methods are considered and the reliability of these methods assessed against the available data both with and without consideration of the system effect as discerned from the MC simulation. The chapter

concludes with discussion of needed future work and the potential for further incorporating system reliability into CFS-framing design.

6.3 Selected CFS-Framed OSB-Sheathed Shear Walls

As part of an overall research effort to improve CFS-framed seismic design, known as the CFS-NEES effort (see [13]) Liu et al. conducted a series of monotonic and cyclic CFS-framed, OSB-sheathed shear wall experiments [1]. The effect of construction details on shear wall behavior, including dimension, thickness of studs, and seam location, etc., were explored in the experiments. Typical shear wall configurations for 1.22 m and 2.44 m wide walls are provided in Figure 6-4 and complete details are provided in [1]. These experiments are independent from the testing used to formulate AISI S400 and since they were conducted under the purview of this same research team all details were available for the simulations performed herein.

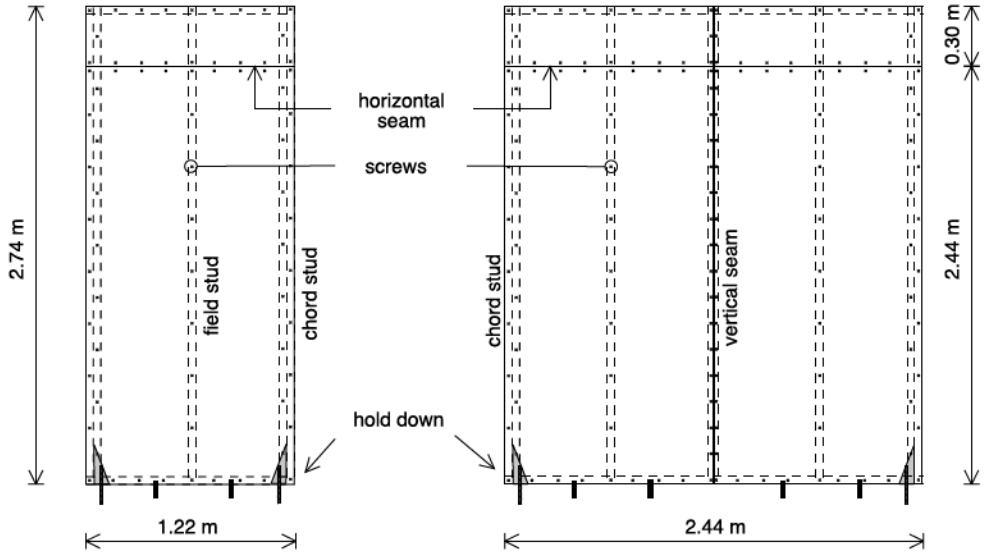

Figure 6-4. Two shear wall configurations of Liu et al. CFS shear wall tests: 1.22 m width and 2.44 m width

Twelve shear wall configurations, as summarized in Table 6-1, from Liu's test series were selected to conduct reliability evaluation of CFS-framed shear walls. These same walls were considered deterministically in Buonopane et al. [11] where a model for predicting the strength based on local nonlinear fastener response was developed.

Table 6-1. Selected shear walls from Liu et al. [1] test

Test or Model Number	Size (mxm)	OSB sheathing	Gypsum sheathing	Ledger	Horizontal seam (mm)	Vertical seam (mm)	Tested strength (kN)
1	1.22×2.74	✔	-	✔	2438 up	-	21.82
2	1.22×2.74	✔	✔	✔	2438 up	-	22.43
3	1.22×2.74	✔	-	-	2438 up	-	18.65
4	1.22×2.74	✔	-	✔	2133 up	-	18.17
5	1.22×2.74	✔	-	-	2133 up	-	21.95
6	1.22×2.74	✔	-	-	2133 up	305 over	15.61
7*	1.22×2.74	✔	-	-	2438 up	610 over	18.41
8	1.22×2.74	✔	-	-	2438 up	610 over	16.34
9	1.22×2.74	✔	-	-	1372 up	610 over	16.95
10	2.44×2.74	✔	-	✔	2438 up	-	38.77
11	2.44×2.74	✔	✔	✔	2438 up	-	47.30
12	2.44×2.74	✔	-	-	2438 up	-	37.55

*Note: in test 7, there is additional one field stud 0.3 m over from side. Details see Liu et al.[1]

6.4 Fastener-Based Modeling of CFS-Framed Shear Walls

Buonopane et al. [11] developed and validated a structural model for CFS-framed wood-sheathed shear walls in OpenSees[14] . The model consists of elastic beam-column elements for all steel framing, rigid diaphragm elements for each individual sheathing board, linear springs for steel-to-steel connections such as the stud to track, and nonlinear springs for all steel-fastener-sheathing connections (Table 6-2 summarizes and [11] provides all further details). The model was able to reproduce key characteristics of the force–displacement hysteretic response of shear wall tests without calibration. The model reasonably predicted peak strength, and displacement at peak strength, as well as per cycle and total energy dissipation. The model does not capture failure modes outside of

the fasteners – i.e. in the chord studs, track, or hold-down, and ignores torsion effects from one-sided sheathing applications. The provided model is only valid insofar as failure is precipitated at the fasteners.

In this model essentially all nonlinearity in response is derived from the connection model and is thus referred to as a fastener-based model for a shear wall. The model has a direct legacy in work on wood–framed shear walls (e.g., see [11]) and has been used to characterize the response of CFS-framed shear walls for larger whole building models [15,16]. The model may include or exclude the performance of shear wall hold-downs depending on the measurements being compared against and the objective of the model. If included the nonlinearity of the hold-downs and the potential for bearing-based load transfer of the field and chord studs has been shown to be important [15,16].

Table 6-2. Summary of materials and elements used in OpenSees models

Component	Engineering designation	Element type	Element in OpenSees	Material in OpenSees
stud	600S162-54	Euler-Bernoulli beam	DispBeamColumn	linear elastic
track	600T150-54	Euler-Bernoulli beam	DispBeamColumn	linear elastic
strap	1 1/2 in.×54 mil	Euler-Bernoulli beam	DispBeamColumn	linear elastic
ledger track	1200T200-97	Euler-Bernoulli beam	DispBeamColumn	linear elastic
sheathing	Oriented Strand Board	Multi-Point constraint	RigidDiaphragm	-
sheathing fastener (wood-to-steel)	#8 or #10 flathead screw	Spring element	CoupledZeroLength	Pinching04
hold-down	Simpson S/HDU6	Spring element	Zero-length element	linear elastic
steel fastener (stud-to-track)	#10 flathead screw	Spring element	Rotational spring	Rotational stiffness at 11.3 kN-m/rad

The steel studs are modeled with displacement-based beam column elements and actual cross section properties are assigned to the element. The studs are connected to the top and bottom tracks with rotational spring elements. The rotational stiffness for the spring element was estimated to be 11.3 kN-m/rad based on the bare CFS frames test [1] . The hold-downs are modeled as uniaxial spring elements in the vertical direction. A tension stiffness of 9.9 kN/mm [8] was assigned to the hold-down elements, and a compression stiffness 1000 times as large as tension to simulate a rigid foundation. The KrylovNewton algorithm is used as the solver in OpenSees.

The steel-fastener-sheathing connection is modeled using the Pinching04 material [17] in OpenSees and zero-length radial springs in the fastener-based model. Pinching04 is a one dimensional hysteretic material model which employs 4 linear segments for its monotonic backbone response. The material also allows for defining unloading and reloading parameters that enable the user to define any level of pinching and stiffness degradation. Damage parameters for additional stiffness degradation are also available, but not used in this work. The Pinching04 parameters were estimated based on testing by Peterman and Schafer [12] and applied in a deterministic fashion in Buonopane et al. [11]. The extension of this model from deterministic to random is the subject of the following section.

6.5 Characterization of Fastener Properties as Random Variables

The nonlinear shear response of a fastener connected through sheathing to steel can be determined in isolated testing. Motivated from work in sheathing braced design of studs [18] a small test rig was modified by Peterman et al. [12] and used to generate monotonic

and cyclic response of steel-fastener-sheathing combinations consistent with the shear wall testing in [1] .The testing rig consists of installing two standard studs in a universal uniaxial testing machine, attaching the studs with sheathing, and finally cycling the resulting specimen. For symmetry two fasteners are placed between the sheathing and the stud and both faces of the stud are sheathed. Focusing on a single fastener, before and after testing, the results for a typical test are provided in Figure 6-5.

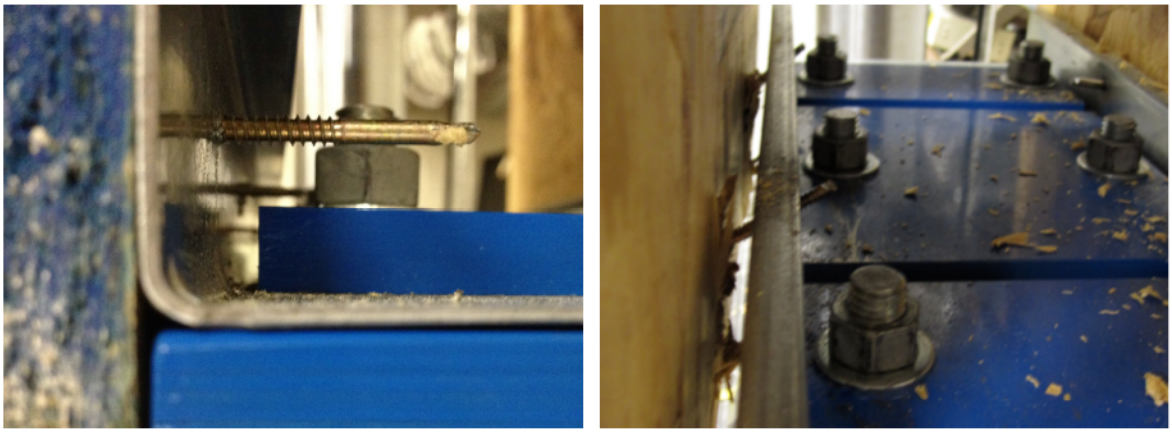

(a) prior to testing (b) after failure

Figure 6-5. Local view of small scale sheathing-fastener-stud testing for shear response (Peterman et al. [12])

6.5.1 Fastener Test Data and Backbone Curve Assumption

Considering the subset of testing relevant for the analyses performed herein, the monotonic tests on #8 fasteners drilled through 11.1 mm [7/16 in.] OSB sheathing and anchored in 1.4 mm [54 mil = 0.054 in.] steel are provided in Figure 6-6a.

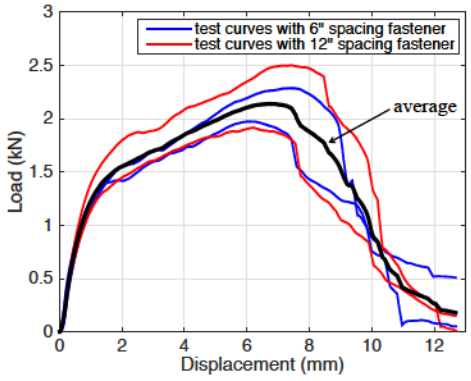

(a) example of fastener test curves

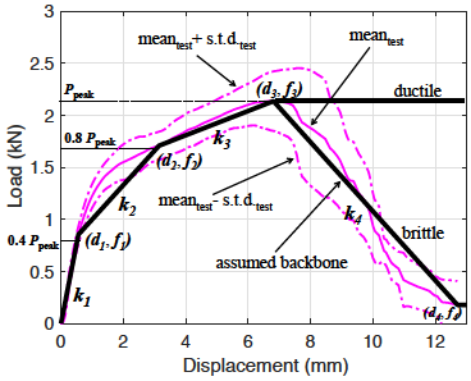

(b) conceptual Pinching04 fit to test data

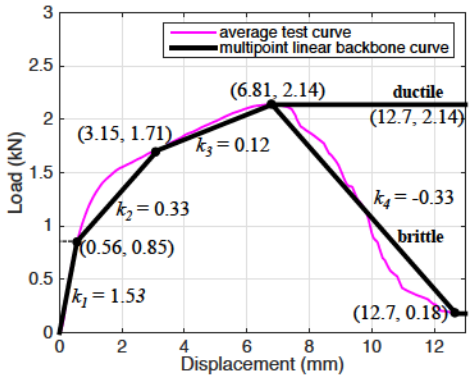

(c) selected average fit from test data for 11.1 mm OSB sheathing and #8 screws to 54 mil steel

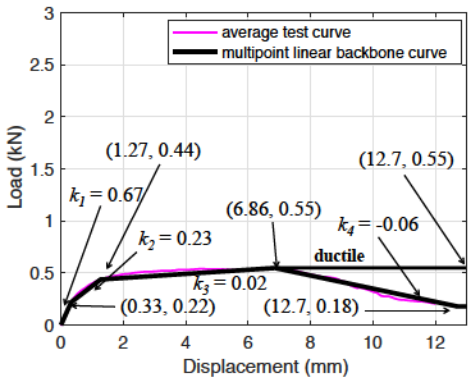

(d) selected average fit from test data for Gypsum board and #6 screws to 54 mil steel

Figure 6-6. Sheathing-fastener-steel connection shear backbone response models

Results are included for both tested fastener spacings: 152.4 mm (6 in.) and 304.8 mm (12 in.), since Peterman et al. showed that fastener spacing did not influence the local shear response[12] . The Pinching04 material model provides 4 linear segments that may be employed in approximating the backbone response. Consistent with past work, the backbone was constructed by utilizing the response at 40% peak load, 80% peak load, peak load, and mean load at largest tested displacement as illustrated in Figure 6-6b. The post-peak model was considered in one of two ways: (a) brittle – following the average post-peak response or (b) idealized-ductile – following the ideal ductile post-peak

response. These two variants are used later in the simulations to understand the impact of the post-peak fastener behavior on the variability of the shear wall response.

6.5.2 Generation of Random Fastener Backbones

For development of simulations fastener peak strength f_3 was chosen as the only independent random variable. All other backbone parameters are generated as dependent on peak strength, i.e. are perfectly correlated with f_3. From the test data for a #8 fastener in 11.1 mm OSB sheathing and 1.4 mm steel the mean (μ_{f3}) and standard deviation (σ_{f3}) of the fastener strength is 2.14 kN and 0.28 kN respectively. Therefore, the coefficient of variation (C.O.V.) of the peak fastener strength (V_{f3})=0.28/2.14=13%.

The authors have conducted a large number of fastener tests with similar (fasteners through sheathing anchored in steel sheet and exercised in shear) but not identical details (steel thickness, fastener type, sheathing thickness) to those used here [10]. These fastener peak strengths were log-transformed and then a Lilliefors test was applied to the transformed data. The resulting P-value is 0.4278, which is well above the typical threshold e.g. 0.05 for normality. Therefore, we assumed f_3 as lognormal and defined 40%f_3 and 80%f_3 as equal to f_1 and f_2 respectively. For the brittle fastener backbone f_4 is set to 0.18 kN and in the ductile model f_4 equals f_3. (The final plateau strength established by f_4 generally is used to improve numerical stability of the models. In the subsequent simulations for shear walls none of the fastener model response is in this final plateau regime at peak shear wall strength, although it is common to be in the descending branch). All secant stiffness for different branches in the random fastener backbone are the same as in the deterministic multipoint linear backbone curve. With these

assumptions we can define displacement as $d_1 = f_1/k_1$, $d_2 = d_1+(f_2-f_1)/k_2$, $d_3 = d_2+(f_3-f_2)/k_3$, and $d_4 = d_3+(d_4-d_3)/k_4$ for the brittle fastener and d_4=20 mm for the ductile fastener case. After 20 mm for the ductile case, the ductile plateau goes to infinity.

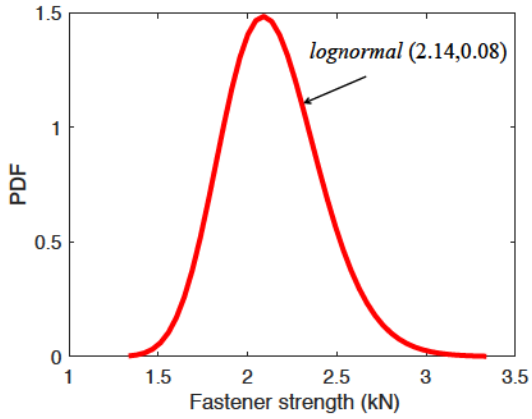

(a) probability density function of lognormal dist.

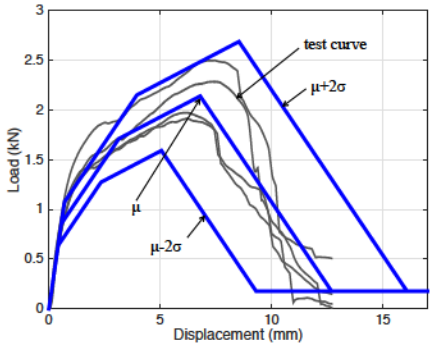

(b) fastener strength and fastener test curve

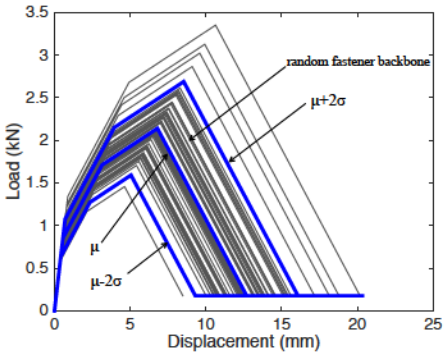

(c) brittle random fastener backbone model

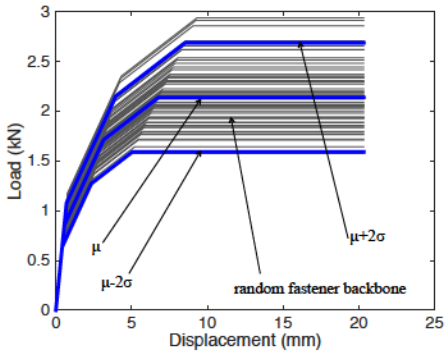

(d) ductile random fastener backbone model

Figure 6-7. Distribution and random fastener backbones for brittle and ductile model

The resulting process for generation of random backbones is illustrated in Figure 6-7. Peak strength is simulated as a lognormal random variable and both brittle and idealized ductile fastener backbone curves can be automatically generated. The process is relatively straightforward – having only a single random variable and resulting in realizations that never cross in force-displacement space. However, it does capture the behavior observed in testing and provides a wide scatter of potential fastener response. The generated brittle

and ductile fastener backbones are used in next section for MC simulations of the shear wall response. Different random backbones were generated for different fasteners in the shear walls and assumed fasteners were uncorrelated in the shear walls.

6.6 Monte Carlo simulation of shear wall pushover response

MC simulation is a brute force technique for studying the stochastic response of a system. A series of deterministic models are generated based on assumptions about the randomness in the system. For a large enough number of samples the assumption is that the statistics of the response of the system converge towards the actual probabilistic response. For the simulations performed here the first two moments of the peak strength of the shear wall (i.e. mean and variance of the shear wall strength) are of particular interest and convergence occurs within 1000 simulations.

6.6.1 Monte Carlo Simulation of Shear Wall with Brittle Fastener Model

A typical shear wall test specimen (test 1c in[1]) was selected to conduct MC Simulation. The dimension and configuration details are provided in Table 6-1. For this study, 1000 pushover simulations were conducted with the fastener-based shear wall model, each with 70 independent identical distributed (i.i.d.) random (brittle) fastener backbone models. Effectively one draw in the MC simulation of the wall includes the 70 i.i.d. fasteners, and then a pushover analysis is conducted and the response recorded. The second draw includes a new 70 i.i.d. fasteners, and this continues for 1000 total draws such that statistics of the pushover simulation itself can be estimated.

The lateral load displacement curves and histogram of peak strength are shown in Figure 6-8(a) and (b), respectively. Note, the underlying assumption of the fastener-based

models, that the initial stiffness is constant, results in all 1000 simulations beginning with the same deterministic stiffness. To provide a comparison three additional deterministic models were run: (a) all fasteners were given the mean (μ) backbone response, (b) all fasteners were given the μ + 1 standard deviation (σ) backbone response, and (c) all fasteners were given the μ – σ fastener backbone response. Interestingly, the response of the shear wall is well within these bounds. In fact, even though the CoV of the fastener strength is 13% the CoV of the shear wall peak strength is less than 3%. This reduction in variability is beneficial and suggests useful redistribution of load across fasteners within the shear wall under load; however, it is worth noting that the mean shear wall strength is 16.9 kN compared with 17.2 kN for the deterministic model based on average properties, indicating not all system effects are beneficial. Thus, a design that uses mean fastener properties to predict the mean strength of the shear wall will modestly over-estimate the mean shear wall strength.

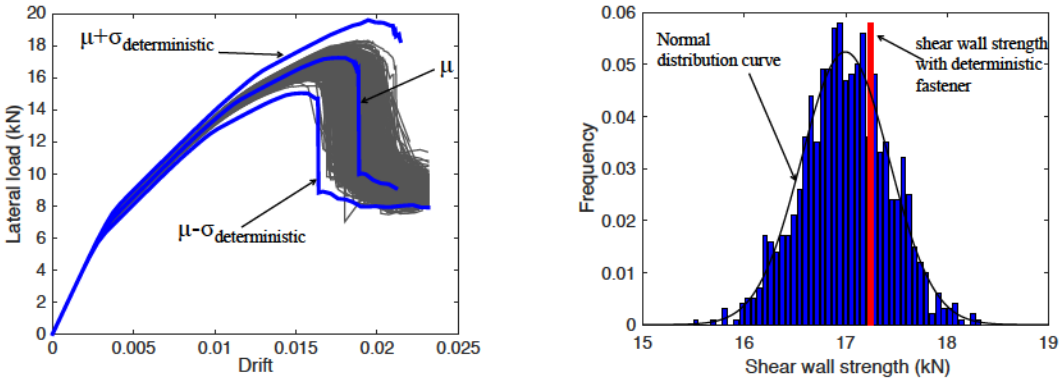

(a) (b)

Figure 6-8. Shear wall load-drift curve with 1000 realizations and its histogram with brittle fastener model

The utilization of the fasteners within the shear wall may be measured by their demand-to-capacity (DC) ratio. For each fastener in the shear wall, the DC ratio was defined as

the ratio of the fastener force at shear wall peak strength to the fastener capacity of the individually sampled fastener strength (i.e. each individual realization of f_3). The average DC ratio for each fastener based on 1000 MC simulations at 1.5% wall drift and at shear wall peak strength are provided in Figure 6-9 (a) and (b), respectively.

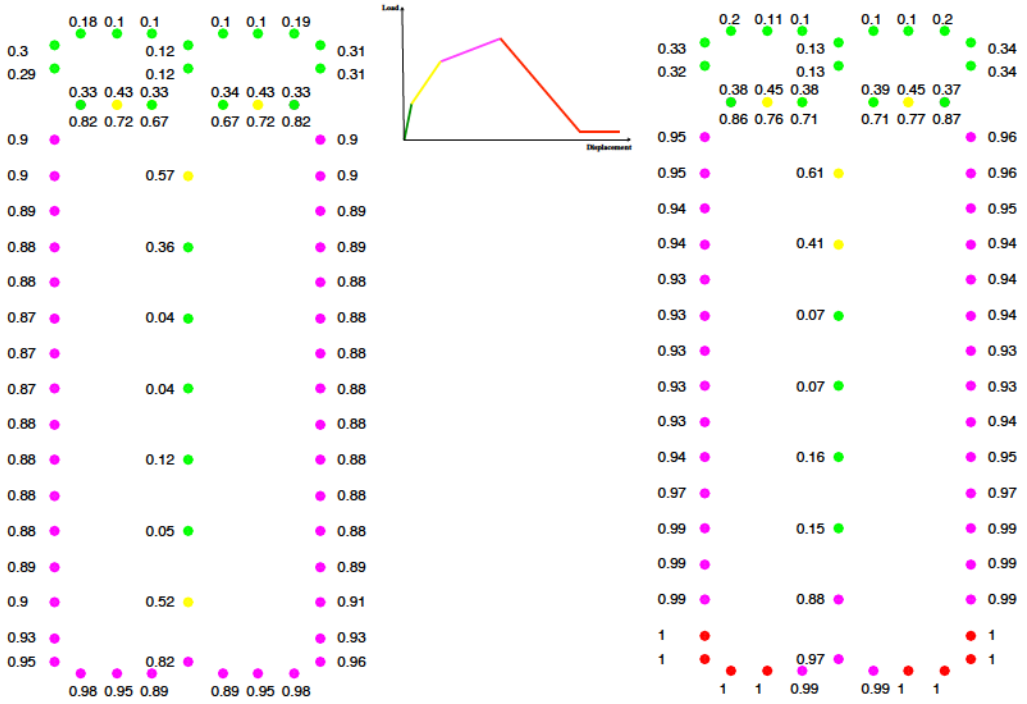

(a) at 1.5% shear wall drift

(b) at shear wall peak strength

Figure 6-9. Average shear wall fastener demand-to-capacity ratios

Fasteners in the bottom corners have the highest DC ratios, at or approaching 1.0 even well before the wall has reached peak strength. At peak strength, multiple fasteners in the bottom are in the post-peak response range. Fasteners in the upper portion of the shear wall are not highly utilized because the ledger framing at the top of the shear wall provides substantial frame bending resistance in addition to the fastener-based resistance.

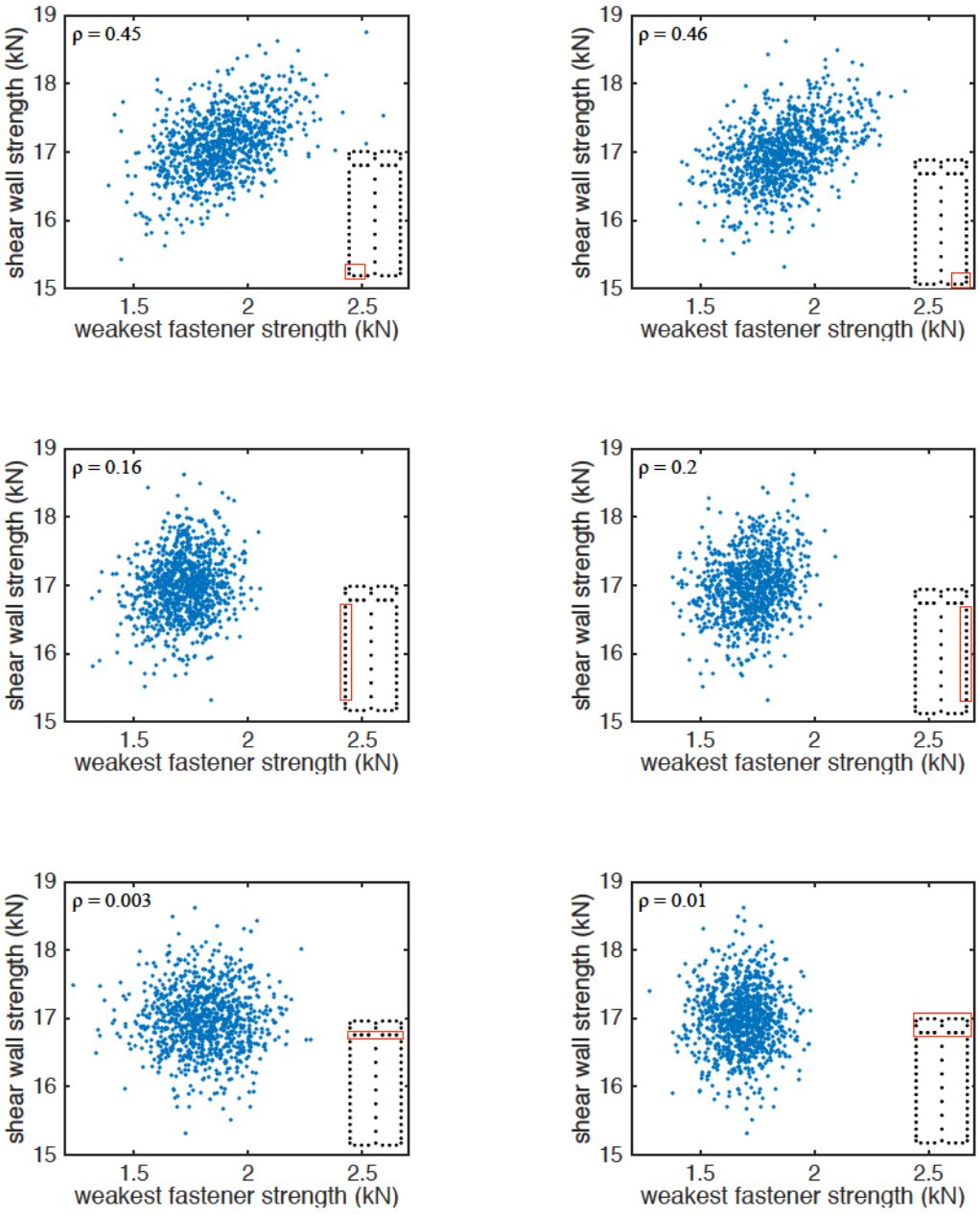

Figure 6-10. Correlation coefficient between shear wall strength and fastener groups at peak strength for brittle shear wall models

In shear walls, fasteners work as groups. Fastener failure, or degradation in fastener stiffness, is mitigated by closely spaced neighboring fasteners that can carry additional force. To explore these fastener group effects all fasteners were divided into groups, and

compared the correlation coefficient for the weakest fastener strength and shear wall strength. Fasteners at the same location, and with similar DC ratios were divided into the same fastener group. Figure 6-10 (a) - (f) illustrate the correlation coefficient for the six selected fastener groups. In the bottom corner of the shear wall the correlation coefficient is 0.45 while it is only 0.003 for the fastener group at the horizontal seam location. The failure of a single fastener does not equate to failure of the shear wall, but the failure of fastener in the bottom is more important than in other locations. Figure 6-10 provides a means to understand the relative importance of fastener location in a typical shear wall.

6.6.2 Monte Carlo Simulation of Shear Wall with Ductile Fastener Model

Ideally, fasteners would have fully ductile response and thus allow for weaker fasteners to always redistribute to stronger fasteners. To understand the impact of this ideal case MC simulation employing the idealized ductile fastener model was also conducted. 1000 simulations were conducted for shear wall 1 and the results are summarized here. Unlike the brittle fastener simulations, peak load is only reached when every fastener has yielded and this leads to unrealistic wall drifts, therefore a maximum 101.6 mm [4 in.] or 3.7% drift was allowed. This drift is consistent with maximum drift observed in related testing (see, e.g. [1]). Shear force-displacement response and a histogram of "peak" strength at 3.7% drift are provided in Figure 6-11. The deterministic models with fastener inputs at μ and $\mu+/-\sigma$ are also provided again for comparison. As before the shear wall peak strength variability (CoV of 3%) is far less than the input variability on the peak fastener strength (CoV of 13%). However, this time, in the fully ductile model the average wall strength is equal to a deterministic model based on average fastener strength. As expected, no

detrimental system effects are observed in the case of idealized, fully ductile, fastener response.

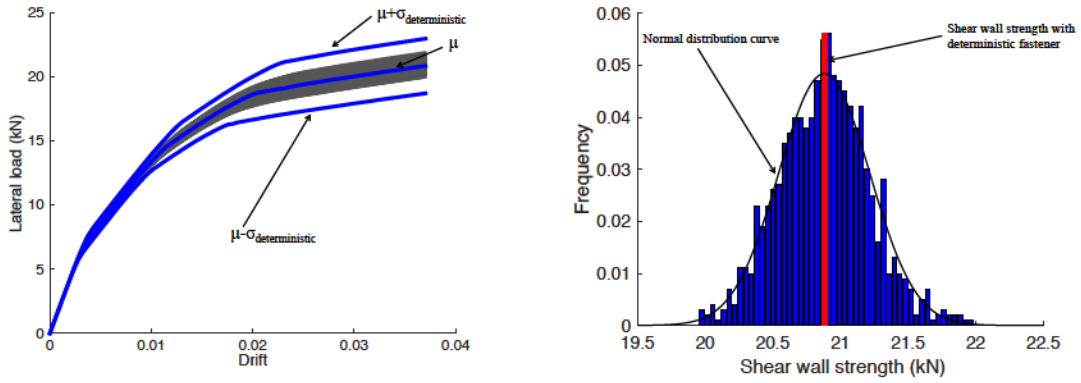

(a) (b)

Figure 6-11. Shear wall load-drift curve with 1000 realizations and its histogram with ductile fastener model

Correlation between the weakest fastener in a selected group and the shear wall peak strength are provided for the ductile model in Figure 6-12. Compared with the brittle model results, the ductile model shows lower correlation for those fasteners that initially have high DC ratios. This is consistent with the complete redistribution that is allowed in the idealized ductile fastener case. Since the fastener has ductile behavior, even the weak fasteners can indefinitely carry force, and allow load redistribution. This redistribution results in fastener location having even less correlation to shear wall strength.

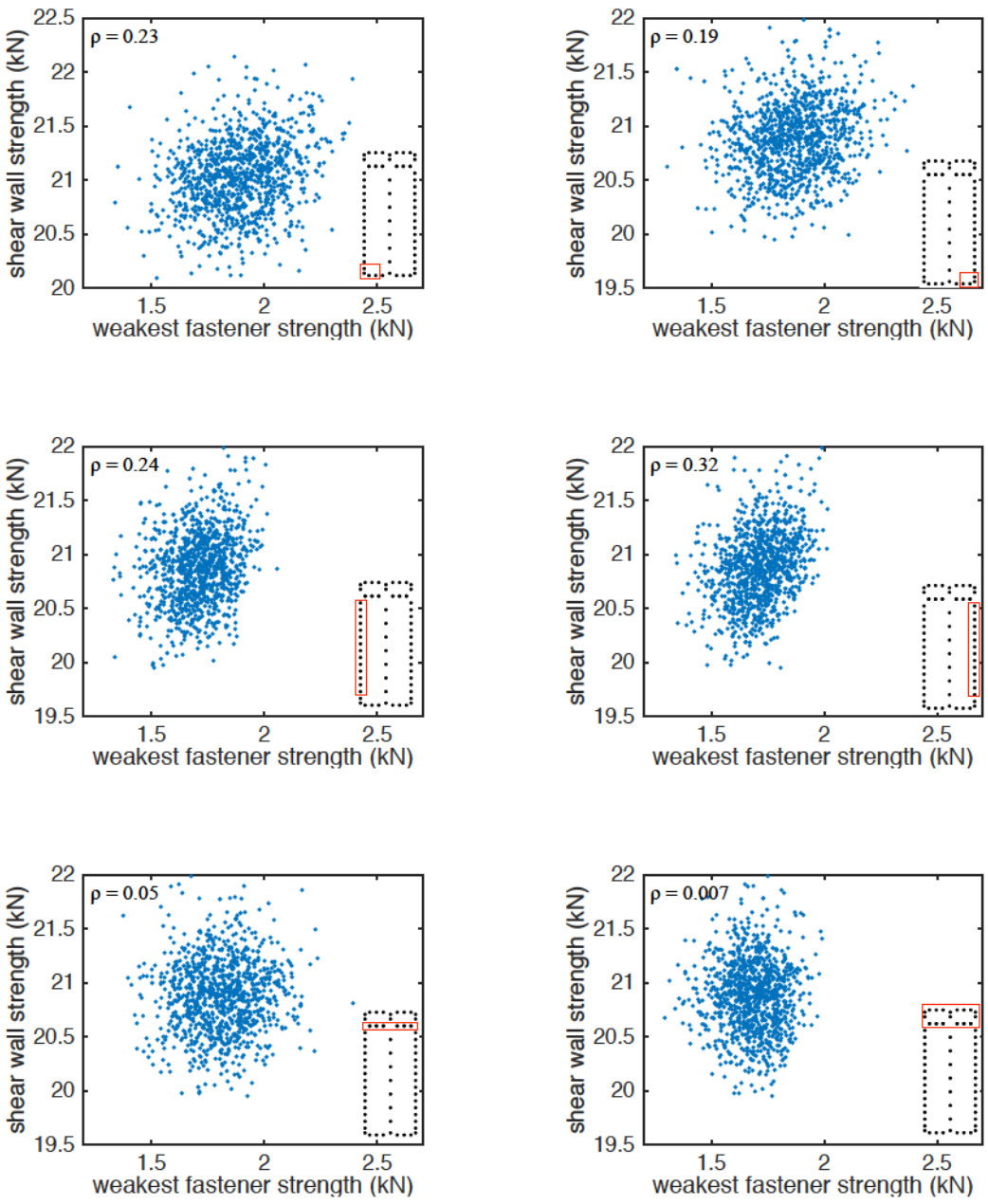

Figure 6-12. Correlation coefficient between shear wall strength and fastener groups at peak strength for ductile shear wall models

The simulations indicate that variability in response increases with drift (e.g. Figure 6-8a). To examine this histograms of the shear wall strength were provided at 0.5, 1.0, and 1.5% wall drift in Figure 6-13. The standard deviation in strength increases from less than

1% to almost 2% over the studied drift range and the brittle fastener model has slightly higher variability. However, the absolute magnitude of the variability is small (variance is 0.04 kN^2 at the maximum).

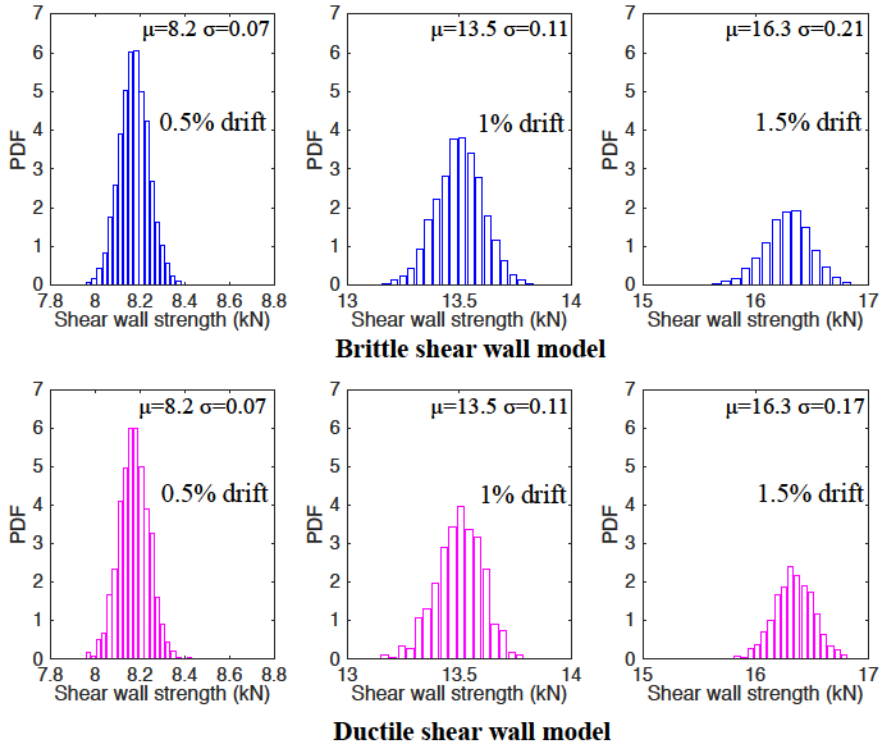

Figure 6-13. Shear wall strength histogram under different drift

This research was conducted as part of the U.S. National Science Foundation sponsored project "NEESR-CR: Enabling Performance-Based Seismic Design of Multi-Story Cold-Formed Steel Structures (CFS-NEES)" (NSF-CMMI-1041578). The project also received supplementary support and funding from the American Iron and Steel Institute and the Bucknell University Program for Undergraduate Research. Project updates are available at www.ce.jhu.edu/cfsnees. Any opinions, findings, and conclusions or recommendations expressed in this publication are those of the author(s) and do not necessarily reflect the views of the National Science Foundation or the American Iron and Steel Institute.

6.6.3 Statistical Results for Studied Shear Wall Configurations

The testing detailed in Section 2 (Figure 6-4 and Table 6-1) covers a range of shear wall construction spanning the conditions employed in a prototype two-story cold-formed steel framed building (see Schafer et al. [13]). In this section MC simulation was extended to all twelve shear wall configurations reported in Section 2. Shear wall model with brittle connections was used in all simulations.

For each shear wall configuration Monte Carlo simulations were performed. The mean (μ_{MC}), standard deviation (σ_{MC}) and CoV (V_{MC}) for the peak strength from the simulations is reported in Table 6-3. In addition the mean peak strength from the MC simulation is compared to the peak strength based on a single deterministic pushover analysis using average fastener properties (F_{Det}) in Table 6-3. Tested shear wall strength is also listed in the table and compared with MC mean strength. Across all configurations $\mu_{MC} < F_{Det}$ indicating the mean system strength is slightly lower than the expected strength based on the mean component strength. This is indicative of a series system; however, the ratio is only slightly less than 1.0 (average is 0.97) so the system effect on the mean strength is only modestly negative. Shear wall strength from the simulations is generally similar to the tested strength – walls with more conservative simulation prediction generally have larger numbers of sheathing boards and seams and contact between the boards is not included in the developed model; see [11] for further discussion.

The dispersion in results across the 12 studied tests is depicted in the box and whisker plots of Figure 6-14. Results are again normalized by F_{Det}. Mean values are slightly less than 1.0 and dispersion is consistently small. The average CoV in peak shear wall strength for the studied shear walls is 2.3% and the maximum CoV is 3.0% - considerably less than that CoV of the peak fastener strength which is 13%. With respect to variability, the system effect in a shear wall is highly beneficial.

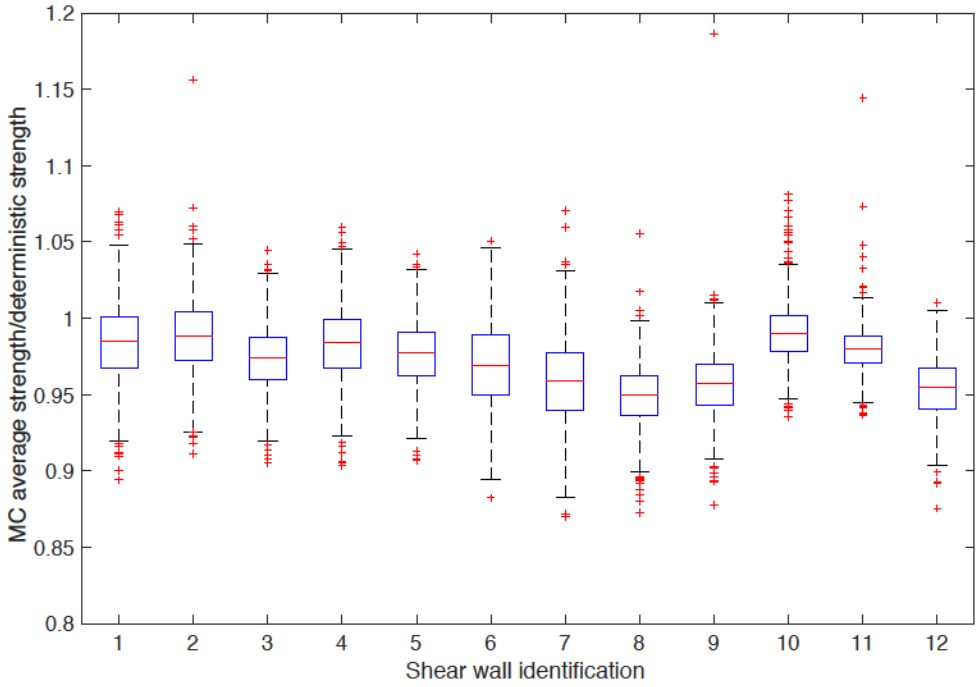

Figure 6-14. Box-and-whisker plot of shear wall Monte Carlo Simulation strength/deterministic shear wall strength ratio

6.7 Reliability of Simulated Shear Wall

The first order second moment reliability index may be expressed as:

$$\beta = \frac{\ln(R_m / Q_m)}{\sqrt{V_R^2 + V_Q^2}} \tag{6-1}$$

Table 6-3. Predicted peak strength for all selected shear wall configurations

	MC Simulation			Deterministic		Experiment	
Model No.	μ_{MC} (kN)	σ_{MC} (kN)	V_{MC} (σ/μ)	F_{Det} (kN)	μ_{MC} / F_{Det}	F_{test} (kN)	μ_{MC} / F_{test}
1	17.22	0.456	2.65%	17.49	0.98	21.82	0.79
2	22.05	0.516	2.34%	22.31	0.99	22.43	0.98
3	16.55	0.369	2.23%	16.99	0.97	18.65	0.89
4	17.55	0.425	2.42%	17.84	0.98	18.17	0.97
5	16.78	0.364	2.17%	17.18	0.98	21.95	0.76
6	12.65	0.364	2.88%	13.05	0.97	15.61	0.81
7	15.11	0.449	2.97%	15.76	0.96	18.41	0.82
8	15.90	0.347	2.18%	16.76	0.95	16.34	0.97
9	16.62	0.377	2.27%	17.37	0.96	16.95	0.98
10	37.20	0.710	1.91%	37.56	0.99	38.77	0.96
11	45.81	0.725	1.58%	46.78	0.98	47.30	0.97
12	33.24	0.681	2.05%	34.84	0.95	37.55	0.89
		average:	2.30%		0.97		0.90

where R_m is the mean resistance, V_R the Coefficient of Variation (CoV) of the resistance, Q_m is the mean demand, and V_Q the CoV of the demand. AISI standards for cold-formed steel design, including the standard that governs cold-formed steel framed shear walls (AISI S400-15) utilize Load and Resistance Factor Design (LRFD) as implemented and detailed in the commentary to AISI S100-16. For LRFD the design strength (ϕR_n) must be greater than any load combinations considered ($\Sigma \gamma_i Q_i$) where i is a summation across various loading types (dead, live, wind, etc.).

$$\phi R_n \geq \sum \gamma_i Q_i \tag{6-2}$$

As detailed in[19] the substitution of Eq. (6-2) into (6-1) provides different estimates for β depending on the load combination selected and on the ratio of the various loads (Q_i's)

to one another. However, despite this complexity AISI S100-16 has adopted a single load combination and ratio of loads for its LRFD calibration – this results in consistent approximations across different limit states, although it has conceptual limitations as fully discussed in [19]. If we assume the nominal resistance, R_n, is set equal to the mean resistance from the MC simulations R_m, and employ the load combinations and load ratios implicit in AISI S100, then the reliability index simplifies to:

$$\beta = \frac{\ln(1.521/\phi)}{\sqrt{V_R^2 + 0.21^2}} \tag{6-3}$$

or, for a known β, the resistance factor may be found as:

$$\phi = 1.521 e^{-\beta\sqrt{V_R^2+0.21^2}} \tag{6-4}$$

(Note the pre-factor 1.521 may be observed in AISI S100-16 Eq.C-B3.2.2-14[20]). For this scenario, the CoV in the resistance drives the reliability assessment. The CoV in Table 6-3 provides V_R for the 12 simulated walls (V_{MC}). Currently, AISI S400-15 utilizes a ϕ=0.6, the β implied by this assumption is provided in Table 6-4. In addition – the target β for AISI standards is 2.5 for members and 3.5 for connections. The ϕ that results from these target β are also provided in Table 6-4.

Based on the simulated shear walls the reliability achieved in a design utilizing mean MC simulation results for the nominal strength and the AISI S400-15 ϕ factor for shear walls

is significantly in excess of target reliabilities (mean β=4.4). If traditional target reliabilities are enforced (2.5 or 3.5) higher ϕ factors could be employed. These results cover a limited scope and focus on direct use of the simulation results. In design, simpler methods are usually employed – the following section introduces several potential design methods for CFS-framed OSB-sheathed shear walls, and then assesses their reliability across the 12 selected tests.

Table 6-4. Reliability index and resistance factor of simulated shear walls

Model No.	β when ϕ=0.6	ϕ when β = 2.5	ϕ when β =3.5
1	4.39	0.896	0.725
2	4.40	0.897	0.726
3	4.40	0.897	0.726
4	4.40	0.897	0.726
5	4.41	0.897	0.726
6	4.39	0.895	0.724
7	4.39	0.895	0.724
8	4.41	0.897	0.726
9	4.40	0.897	0.726
10	4.41	0.898	0.727
11	4.42	0.898	0.728
12	4.41	0.898	0.727
mean	4.40	0.90	0.73

6.8 Design Methods for OSB-Sheathed Shear Walls

Based on the current design specification and our simulation method, four design methods are proposed below for examination of cold-formed steel shear wall resistance.

Method 1: Current Specification method. In AISI S400-15 (previously AISI S213-12) CFS-framed shear wall strength, with different sheathing types applied, is provided. The method is based on direct experiments (independent from the ones being used here for reliability evaluation) and primarily considers thickness of steel framing, thickness and type of sheathing, and fastener spacing. Wall aspect ratio is also considered for narrow

shear walls. Wall strength per unit length of the wall is found directly from a table in AISI S400-15 and multiplied times the actual wall length to arrive at the shear capacity.

Method 2: (Elastic) First fastener failure method. In most structural systems the procedure for conventional design is to perform linear elastic analysis and then scale the results (axial, shear, and moment demands) to the first member and/or connector failure to establish the system strength. Using the fastener-based models developed by Buonoapane et al. [11] and utilized herein, this approach can readily be performed. A linear elastic model of the shear wall is completed, and the results are linearly scaled until the peak fastener demand equals the mean fastener capacity and this is used to establish the full shear wall strength. The simulation is linear and deterministic, and provides a simple approach consistent with conventional structural design.

Method 3: Deterministic simulation method. If identical properties based on mean fastener backbone response are used for all fasteners, then a nonlinear static pushover analysis can be completed with the fastener-based shear wall model. The resulting model allows for re-distribution but ignores system effects (beneficial or detrimental) due to variation in the fastener capacity. The simulations are nonlinear, but deterministic, and provide a realistic approximation of a computational tool that engineers could employ.

Method 4: Monte Carlo simulation method. If the approach of this chapter is followed and the fastener backbone response is characterized by a random variable, then simulations of the random variable can be used to generate random fastener response, that

is then employed for the various fasteners in the shear wall simulation. These MC simulations allow for redistribution and for stochastic variation in the system response. This approach is the most robust approach for a design method considered here, but requires a large number of analyses to be generated and analyzed by the engineer, and is thus unlikely to be used in current design.

6.9 Reliability of Design Methods against Selected Tests

In a traditional LRFD reliability formulation the mean resistance (R_m) is connected to the nominal predicted resistance (R_n) per the following:

$$R_m = P_m M_m F_m R_n \tag{6-5}$$

where P, M, and F are uncorrelated random variables representing bias in the prediction method (i.e., the professional factor, P, which is populated by test-to-predicted ratios) as well as bias due to the material properties (M) and fabrication of the structure or connection being considered (F). The subscript m refers to the mean values of P, M, and F. The CoV of the resistance, V_R, is approximated by [20] :

$$V_R = \sqrt{V_M^2 + V_F^2 + V_P^2} \tag{6-6}$$

Where V_M, V_F, V_P are the CoV of the material, fabrication, and professional factor, respectively. Substituting Eq.'s (6-2), (6-5) and (6-6) into Eq. (6-1) and again using the load combinations and load ratios implicit in the AISI S100 LRFD calibration, the reliability index may be expressed as:

$$\beta = \frac{\ln(1.521 P_m M_m F_m / \phi)}{\sqrt{V_M^2 + V_F^2 + V_P^2 + 0.21^2}} \tag{6-7}$$

The four design methods considered establish four predictions for P, i.e. four different mean (P_m) and CoV's (V_P) of test-to-predicted ratios. The remaining random variables M and F are considered in two different ways: (a) per the guidance in AISI S100-16 Chapter K, and (b) informed from the MC simulation performed herein. Therefore, for (a) per AISI S100-16 and assuming connections to wood control the strength: M_m=1.0, V_M=0.15, F_m=1.0, and V_F=0.15.

In general, the variation in M and F is intended to reflect the inherent variation in material and fabrication quality, independent from the variation in the prediction method. For a CFS-framed OSB-sheathed shear wall this variation is controlled by the OSB-to-steel connection limit state. The MC simulations performed here provide an estimation of the shear wall system variation and per Table 6-3 the average V_{MC}=2.3%. Note, the input variability of the peak connector strength has a CoV of 13%; however, this fastener variability does not result in a high system variability as significant redistribution of load amongst the fasteners occurs. Therefore, for (b) we assume M_m=1.0, F_m=1.0 per[20] , and $(V_{MC})^2 = (V_M)^2 + (V_F)^2$. The MC simulation provides an estimate of system variability, which in this case is far less than the connection variability – and this will influence the reliability prediction.

The reliability index, β, at the current AISI S400-15 ϕ value for shear walls, and the resulting ϕ based on target reliabilities of 2.5 (members) and 3.5 (connections) are

provided in Table 6-5 for the four considered design methods across the two assumptions of system variability.

Table 6-5. Reliability index and resistance factor across shear wall tests

(a) V_M and V_F per AISI S100-16 connection to wood case

Design Method	V_R	β when ϕ=0.6	ϕ when β = 2.5	ϕ when β =3.5
AISI S400-15	0.24	3.60	0.86	0.62
First Fastener Failure	0.25	4.84	1.29	0.93
Det. Simulation	0.23	3.24	0.76	0.55
MC Simulation	0.23	3.33	0.78	0.57

(b) V_M and V_F based on MC simulation

Design Method	V_R	β when ϕ=0.6	ϕ when β = 2.5	ϕ when β =3.5
AISI S400-15	0.12	4.79	1.04	0.82
First Fastener Failure	0.14	6.32	1.57	1.22
Det. Simulation	0.10	4.37	0.93	0.73
MC Simulation	0.10	4.50	0.95	0.76

The current specification prediction AISI S400-15 is shown to provide a target reliability aligned with a connection limit state (near 3.5) under the typical assumptions for variability (Table 6-5a). However, if system variability is considered as estimated from the MC simulation, then the connection variability is dampened, and per Table 6-5b current design is conservative and the ϕ factor could be increased from 0.6 to 0.82 and still meet the connection target reliability of 3.5. The system effect, in this case, reduces the variability considerably and improves the predicted reliability.

If the fastener-based shear wall model was used to replace the tabled solutions in AISI-S400 the reliability would depend on how the model was employed. Traditional engineering design using an elastic model and first predicted fastener failure is unduly conservative under any set of assumptions and has limited use in a modern design context. The reliability indices reported in Table 6-5 indicate deterministic simulation, essentially a shear wall pushover analysis, is adequate – and full MC simulation is not

needed. The modest decrease in the mean predicted strength that occurs in the MC simulation is offset by a large and beneficial decrease in variability. This beneficial system effect dominates the reliability calculation.

If deterministic shear wall simulation using the fastener-based model was implemented for design and the beneficial system effect ignored, i.e. Table 6-5a results, then a ϕ=0.6, as used in current design, will meet a target reliability of 3.5. If the reduced variability of the shear wall system is accounted for then ϕ could be increased to 0.73 for a target reliability of 3.5 or as high as 0.93 for the member target reliability of 2.5. Analysis across a wider series of tests is needed before drawing final conclusions, but this work indicates that the fastener-based simulations can provide comparable reliability to current experimentally-based design methods – and that if system effects on variability are incorporated then ϕ factors may be increased above the current value of 0.6.

6.10 Discussion

Reliability evaluation, as provided in this research, is based on twelve shear wall tests. Analysis of additional shear walls, even within CFS-framed OSB-sheathed configurations, need to be completed before final recommendations for design can be made. Recent fastener testing of Moen et al. [21] provides much needed data on the steel-fastener-sheathing shear response for a broader range of conditions and will be needed for any such analyses.

Improvements in the random fastener characterization and in the fastener-based shear wall model also provide avenues for improvement. The random model for the fastener

does not consider the potential for differing initial stiffness, this would potentially provide additional system variability and is worth pursuing. The fastener-based shear wall model excludes failures in the studs, tracks, and hold-downs and in the sheathing material outside of the fastener locations. Further, the role of the shear stiffness of the sheathing outside of its impact on the local fastener bearing stiffness is not captured. In addition, sheet-to-sheet edge contact is not considered in the developed models. All of these refinements could further enrich the discussion of the shear wall response and its reliability across multiple potential limit states.

Assessing the reliability for seismic load cases is particularly problematic. For one, the cyclic response of the shear walls must be considered in the reliability analysis. In addition the reliability formulation must be re-considered. Here the issue is avoided by using the reliability formulation utilized in AISI S100 and by considering only the fastener limit state. Meimand and Schafer in [19] provide insight on the impact of seismic load cases on the AISI S100 LRFD calibration (particularly V_Q and the pre-factor based on the load combination coefficient and bias). The variations are high and resulting reliability indices are lower than generally assumed for all structural systems. Limit states outside of fastener-based damage (e.g. local-global buckling of the chord stud) are possible, but their probability of failure is significantly reduced through the use of capacity-based design principles. Nonetheless, these other limit states are not currently included in the fastener-based simulation, nor in the MC simulations that rely on this model and could be incorporated in the future.

The current state of the art for assessing seismic response is the application of incremental dynamic analysis (IDA). The fastener-based model provided here has been used for driving a series of IDA models of a CFS-framed building ([15,16]). In the FEMA P695 methodology variability in response is assessed by IDA analysis against different earthquake records – but the models are always deterministic. While the assumption that seismic demand variation is much greater than any variation in capacity is generally believed to be true, MC shear wall simulation using IDA could be used to examine the impact of capacity separately from demand. Further, the impact of brittle fastener response may be different in a dynamic analysis than in the nonlinear static analysis and is worth further study.

6.11 Conclusion

Lateral performance of cold-formed steel framed, wood-sheathed, shear walls are dominated by the local response of the sheathing-to-steel connections. This response derives from a complex interaction between the fastener and the sheathing and steel sheet that are connected together and is considered highly variable. A typical shear wall may rely on 100 or more of these connections. Monte Carlo simulations developed and conducted herein indicate that although the connection strength is highly variable sufficient redistribution occurs in shear walls to mitigate this variability and final system shear wall strength is not highly variable. In the cases studied herein the coefficient of variation for individual fastener strength is 13%, while for the system strength the coefficient of variation is predicted to be less than 3%. There are limits to the redistribution amongst the fasteners as mean shear wall strength is modestly reduced (approximately 3%) below deterministic predictions. In addition, correlation coefficients

are used to quantify fastener locations (e.g. near the corners) that are more important than others for determining wall strength. Examination of existing and proposed shear wall design methods indicate that the predicted reduction in variability is a major system benefit when considering reliability. Based on the analysis provided herein the current resistance factor used in the American Iron and Steel Institute standard for cold-formed steel framed shear walls (AISI S400-15) may be excessively conservative. The predicted shear wall reliability index, β, in this study is 4.8, against a target of 3.5. Additional analyses are recommended and complications related to seismic reliability discussed, all with a goal of advancing reliability and design for cold-formed steel framed shear walls.

6.12 Acknowledgement

This research is supported by National Science Foundation through grants CMMI-1300484, 1301033 and 1301001. The authors would also like to acknowledge the American Iron and Steel Institute for their support. Any opinions, findings, and conclusions or recommendations expressed in this material are those of the authors and do not necessarily reflect the views of the National Science Foundation or American Iron and Steel Institute.

6.13 Reference

[1] Liu P, Peterman K, Schafer B. Impact of construction details on OSB-sheathed cold-formed steel framed shear walls. Journal of Constructional Steel Research 2014;101:114-23.

[2] Filiatrault A, Folz B. Performance-based seismic design of wood framed buildings. J.Struct.Eng. 2002;128(1):39-47.

[3] AISI-S400-15. North American Standard for Seismic Design of Cold-Formed Steel Structural Systems, 2015.

[4] AISI-S213-07. North American Standard For Cold-Formed Steel Framing – Lateral Design, 2007.

[5] Serrette R, Encalada J, Juadines M, Nguyen H. Static Racking Behavior of Plywood, OSB, Gypsum, and FiberBond Walls with Metal Framing. Journal of Structural Engineering 1997;123(8).

[6] Branston A, Boudreault F, Chen C, Rogers C. Light-gauge steel-frame wood structural panel shear wall design method. Canadian Journal of Civil Engineering 2006;33(7):872-89.

[7] Zhang H, Rasmussena K, Ellingwood B. Reliability assessment of steel scaffold shoring structures for concrete formwork. Engineering Structures 2012;36.

[8] Buonopane S, and Schafer B. Reliability of Steel Frames Designed with Advanced Analysis. Journal of Structural Engineering 2006;132(2).

[9] Smith BH, Arwade SR, Schafer BW, Moen CD. Design component and system reliability in a low-rise cold formed steel framed commercial building. Engineering Structures 2016;127:434-46.

[10] Chatterjee A, Xiang Y, Moen CD, Arwade SR, Schafer BW. Towards Quantifying Beneficial System Effects In Cold-Formed Steel Wood-Sheathed Floor Diaphragms 22nd International specialty conference on cold-formed steel structures; November; St Louis, Missouri; 2014.

[11] Buonopane SG, Bian G, Tun TH, Schafer BW. Computationally efficient fastener-based models of cold-formed steel shear walls with wood sheathing. Journal of Constructional Steel Research 2015 7;110(0):137-48.

[12] Peterman K, Nakata N, Schafer B. Hysteretic characterization of cold-formed steel stud-to-sheathing connections. Journal of Constructional Steel Research 2014;101:254-64.

[13] Mazzoni S, McKenna F, Scott MH, Fenves GL. Open System for Earthquake Engineering Simulation User Command-Language Manual. 2003;

[14] Mazzoni S, McKenna F, Scott MH, Fenves GL. Open System for Earthquake Engineering Simulation User Command-Language Manual. 2003;.

[15] Leng J, Peterman KD, Bian G, Buonopane GB, Schafer BW. Modeling Seismic Response of a Full-Scale Cold-formed Steel-Framed Building. Engineering Structures Submitted.

[16] Leng, Jiazhen. Simulation of cold-formed steel structures. Diss. Johns Hopkins University, 2015.

[17] Lowes LN, Mitra N, Altoontash A. A beam-column joint model for simulating the earthquake response of reinforced concrete frames. : Pacific Earthquake Engineering Research Center, College of Engineering, University of California; 2003.

[18] Vieira LC, Schafer BW. Lateral stiffness and strength of sheathing braced cold-formed steel stud walls. Eng.Struct. 2012;37:205-13.

[19] Meimand V, Schafer B. Impact of load combinations on structural reliability determined from testing cold-formed steel components. Struct.Saf. 2014;48:25-32.

[20] AISI S100-16. North American Specification for the Design of Cold-Formed Steel Structural Members, 2016

[21] Moen CD, Tao F, Cole R. Monotonic and cyclic backbone response of single shear cold-formed steel screw-fastened connections. The International Colloquium on Stability and Ductility of Steel Structures; 2016.

CHAPTER 7

REDUCED ORDER MODELS FOR PROFILED STEEL DIAPHRAGM PANELS

7.1 Abstract

The objective of this chapter is to provide progress on development and validation of reduced order models for the in plane strength and stiffness of profiled steel panels appropriate for use in structural models of an entire building. Profiled steel panels, i.e, metal deck, often serve as a key distribution element in building lateral force resisting systems. Acting largely as an in-plane shear diaphragm, metal deck as employed in walls, roofs, and floors plays a key role in creating and driving three-dimensional building response. As structural modeling evolves from two-dimensional frameworks to fully three-dimensional buildings, accurate and computationally efficient models of profiled steel panels are needed. Three-dimensional building response is increasingly required by ever-evolving structural standards, particularly in seismic design, and structural efficiency demands that the benefits of three-dimensional response be leveraged in design. Equivalent orthotropic plate models provide a potential reduced order model for profiled steel panels that is investigated in this chapter. A recent proposal for the rigidities in such a model are assessed against shell finite element models of profiled steel panels. In addition, the impact of discrete connections and discrete panels, as occurs in an actual roof system, are assessed when applying these reduced order models. Extension of equivalent orthotropic plate models to elastic buckling and strength, in addition to stiffness, both represent work in progress, but initial results are provided. Examples show

that equivalent orthotropic plate models must be used with care to yield useful results. This effort is an initial step in developing efficient whole building models that accurately incorporate the behavior of profiled steel panels as diaphragms.

7.2 Introduction

Profiled steel panels, i.e., metal deck, are roll-formed from thin steel sheet and can result in simple corrugated shapes or relatively complex longitudinal profiles with additional transverse features such as embossments. These panels serve as the walls and roof in many metal buildings, see Figure 7-1, and form an integral component of common floor systems in a wide variety of buildings. Under lateral loads the panels play a particularly important role as a distribution element, one in which the in-plane shear behavior of the panel is paramount. A typical profiled steel panel roof is illustrated in Figure 7-1. When distributing lateral load this system acts as a diaphragm, with all elements in the system contributing: panel, panel inter-connections, joists, joist-to-panel connections, primary framing, and framing-to-panel connections.

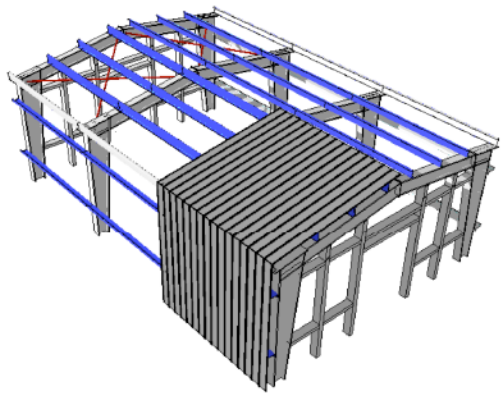

Figure 7-1. Typical metal building with bare profiled steel panel diaphragms

Traditionally, the lateral (e.g., seismic) behavior of buildings has been engineered by examining the two-dimensional (2D) behavior of the lateral force resisting systems in the

primary frames of a building. Increasingly, this is becoming inadequate as (a) experimental evidence mounts that response is largely three-dimensional (3D), (b) efficiencies demand the full 3D response be understood, (c) more complex building geometries are being pursued, and (d) advances in idealizing loads creates more precise 3D demands to be considered. In addition, due to advancements in Building Information Modeling it is now more common to have 3D building models. As a result, it is highly desirable for the engineer to develop 3D structural models; however, while such models can now be more readily created and their need is real, with all details included such models can be prohibitively costly to run, particularly given the myriad of load cases. Thus, we seek the advancement of accurate reduced order models that can be employed in 3D structural models, for modeling diaphragms with profiled steel panels. The focus of this chapter is on the reduced order modeling of the panel itself with additional examination of the panel connections. Future work intends to extend the effort to the complete system of Figure 7-1.

7.3 In-plane Elastic Behavior of Profiled Steel Panels

The in-plane behavior of profiled steel panels is critical for its action as a diaphragm. Even in the linear elastic range the mechanics involved in the in-plane deformations are interesting. Consider a trapezoidal corrugated panel under in-plane actions as illustrated in Figure 7-2, (a) perpendicular to the corrugations significant bending occurs and the panel is quite weak with little Poisson effect, (b) parallel to the corrugations the deformations are largely axial with some Poisson effect, (c) under in-plane shear edge (warping) conditions of the panel become important and bending of the corrugations occur.

(a) axial action parallel to the corrugations

(b) axial action perpendicular to the corrugation

(c) in-plane shear

Figure 7-2. In-plane loading and FE predicted elastic deformations for profiled steel panel

Engineering models of a profiled steel panel typically cannot include the details of the corrugation and instead must resort to an equivalent flat plate. Due to the strongly different stiffness parallel and perpendicular to the corrugations a natural choice is an equivalent orthotropic flat plate as detailed in the following section.

7.4 Equivalent Orthotropic Flat Plate for Corrugated Steel Panel

The notion of employing an equivalent orthotropic flat plate to simulate a corrugated plate has long been used in engineering. Typically, out-of-plane bending behavior is of primary interest as opposed to in-plane behavior and early work such as Easley and Mcfarland (1969) investigated equivalent flexural rigidities. More recently Samanta and Mukhopadhyay (1999) re-examined the problem and developed closed-form expressions

for the orthotropic plate rigidities for both out-of-plane (flexure) and in-plane (extension and shear). This was followed by Xia et al. (2012), who expanded on the earlier work including correcting some assumptions, and derived a set of plate rigidities for equivalent orthotropic plates to model the elastic stiffness of a corrugated plate.

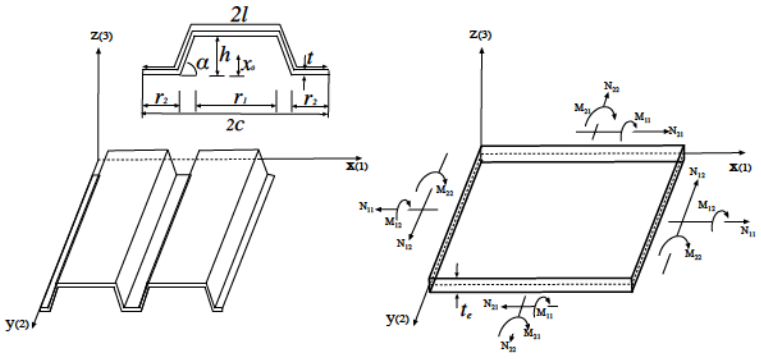

(a) profiled steel panel (b) equivalent orthotropic plate

Figure 7-3. Coordinates and basic dimensions

Central to the work of Xia et al. (2012) and studied here is the conversion of a corrugated plate such as Figure 7-3(a) into that of an equivalent orthotropic flat plate Figure 7-3(b). The rigidities that define the equivalent flat plate connect forces and moments on the equivalent plate to strains and curvatures, via:

$$\begin{Bmatrix} \overline{N_x} \\ \overline{N_y} \\ \overline{N_{xy}} \\ \overline{M_x} \\ \overline{M_y} \\ \overline{M_{xy}} \end{Bmatrix} = \begin{bmatrix} \overline{A_{11}} & \overline{A_{12}} & 0 & 0 & 0 & 0 \\ \overline{A_{12}} & \overline{A_{22}} & 0 & 0 & 0 & 0 \\ 0 & 0 & \overline{A_{66}} & 0 & 0 & 0 \\ 0 & 0 & 0 & \overline{D_{11}} & \overline{D_{12}} & 0 \\ 0 & 0 & 0 & \overline{D_{12}} & \overline{D_{22}} & 0 \\ 0 & 0 & 0 & 0 & 0 & \overline{D_{66}} \end{bmatrix} \begin{Bmatrix} \overline{\varepsilon_x} \\ \overline{\varepsilon_y} \\ \overline{\gamma_{xy}} \\ \overline{\kappa_x} \\ \overline{\kappa_y} \\ \overline{\kappa_{xy}} \end{Bmatrix} \tag{7-1}$$

where the overbars in Eq. (6-1) indicate they are for the equivalent plate not the original corrugated plate.

Table 7-1: Plate Rigidities

	uniform flat plate		direct definition
Rigidity	isotropic[a]	orthotropic[b] (eng. constants)	orthotropic[c] (Xia et al. 2012)
$\overline{A_{11}}$	$\frac{Et}{1-\nu^2}$	$\frac{E_1 t_e}{1-\nu_{12}\nu_{21}}$	$\frac{2c}{\frac{I_1(1-n^2)}{Et}+\frac{12I_2(1-n^2)}{Et^3}}$
$\overline{A_{22}}$	$\frac{Et}{1-\nu^2}$	$\theta_x=\theta_y=\theta_z;u_z=0$	$\nu\overline{A_{12}}+\frac{l}{c}(\nu-\nu^2)\frac{Et}{1-\nu^2}$
$\overline{A_{12}}$	$\nu\frac{Et}{1-\nu^2}$	$\nu_{12}\frac{E_2 t_e}{1-\nu_{12}\nu_{21}}$	$\nu\frac{2c}{\frac{I_1(1-\nu^2)}{Et}+\frac{12I_2(1-\nu^2)}{Et^3}}$
$\overline{A_{66}}$	Gt	$G_{12}t_e$	$\frac{l}{c}Gt$
$\overline{D_{11}}$	$\frac{Et^3}{12(1-\nu^2)}$	$\frac{E_1 t_e^3}{12(1-\nu_{12}\nu_{21})}$	$\frac{c}{l}\frac{Et^3}{12(1-\nu^2)}$
$\overline{D_{22}}$	$\frac{Et^3}{12(1-\nu^2)}$	$\frac{E_2 t_e^3}{12(1-\nu_{12}\nu_{21})}$	$\frac{1}{2c}\left[I_2\frac{Et}{1-\nu^2}+I_1\frac{Et^3}{12(1-\nu^2)}\right.$
$\overline{D_{12}}$	$\nu\frac{Et^3}{12(1-\nu^2)}$	$\nu_{12}\frac{E_2 t_e^3}{12(1-\nu_{12}\nu_{21})}$	$\nu\frac{c}{l}\frac{Et^3}{12(1-\nu^2)}$
$\overline{D_{66}}$	$\frac{Gt^3}{12}$	$\frac{G_{12}t_e^3}{12}$	$\frac{l}{c}\frac{Gt^3}{12}$
	$G=E/2(1+\nu)$	$\nu_{12}E_2=\nu_{21}E_1$	

a. uniform plate, thickness t, material properties E and ν, note $G=E/2(1+\nu)$.

b. uniform orthotropic plate, thickness t_e, properties $E_1,E_2,\nu_{12},\nu_{21},G_{12}$, note $\nu_{12}E_2=\nu_{21}E_1$

c. E, ν, G, t properties of original corrugated plate, c and l properties of section per Figure 2, $I_1=\int_0^{2l}\left(\frac{dx}{ds}\right)^2 ds$ and $I_2=\int_0^{2l} z^2 ds$. Explicit expressions provided for common cases below.

In addition, membrane-bending coupling has been ignored. Xia et al (2012) completed a series of energy solutions that exercise unit strains on the corrugated plate and developed the plate rigidities directly based on the geometry and traditional beam mechanics for the in-plane terms and Kirchoff plate theory for the flexural terms. The developed expressions are provided in Table 7-1 along with additional relevant plate rigidities.

An equivalent isotropic flat plate can only match two rigidities of the actual plate, and is therefore of limited use. Interestingly, an equivalent orthotropic flat plate, with uniform thickness, cannot match all of the 8 directly defined rigidities from Xi et al. (2012) either. While multi-purpose finite element software such as ABAQUS (2012) allows the plate rigidities of Eq. 6-1 to be defined directly most commercial structural engineering software does not, and at best allows the orthotropic engineering constants: E1, E2, ν12, ν21, G12 and an equivalent thickness, te, to be defined. Therefore, in addition to the Xia et al. (2012) expressions, the engineering constants that provide best agreement are also useful. The selection is not unique and depends on what quantities the engineer/analyst desires to match. For diaphragms the in-plane quantities are of the greatest prominence, therefore one set of solutions is to match the Xia et al. 2012 in-plane rigidities to an explicitly defined flat plate with orthotropic material one as follows:

$$E_2 = E \text{ decided a priori} \tag{7-2}$$

$$\frac{E_1}{E_2} = \frac{\overline{Xia\, A_{11}}}{\overline{Xia\, A_{22}}} \rightarrow E_1 = \frac{\overline{Xia\, A_{11}}}{\overline{Xia\, A_{22}}} E_2 \tag{7-3}$$

$$\nu_{12}E_2 = \nu_{21}E_1 \rightarrow \nu_{21} = \nu_{12}E_2 / E_1 \text{ to maintain 12=21 terms} \tag{7-4}$$

$$\frac{E_1 t_e}{1-\nu_{12}\nu_{21}} = \overline{Xia\, A_{11}} \rightarrow t_e = \overline{Xia\, A_{11}} \frac{1-\nu_{12}\nu_{21}}{E_1} \tag{7-5}$$

$$\nu_{12}\frac{E_2 t_e}{1-\nu_{12}\nu_{21}} = \overline{Xia\, A_{12}} \rightarrow t_e = \overline{Xia\, A_{12}} \frac{1-\nu_{12}\nu_{21}}{\nu_{12}E_2} \tag{7-6}$$

$$\overline{Xia\, A_{11}} \frac{1-\nu_{12}\nu_{21}}{E_1} = \overline{Xia\, A_{12}} \frac{1-\nu_{12}\nu_{21}}{\nu_{12}E_2} \rightarrow \nu_{12} = \frac{\overline{Xia\, A_{12}}}{\overline{Xia\, A_{11}}} \frac{E_1}{E_2} \tag{7-7}$$

$$G_{12}t_e = \overline{Xia\, A_{66}} \rightarrow G_{12} = \overline{Xia\, A_{66}} / t_e \tag{7-8}$$

Note the Xia et al. 2012 expressions include the integrals I_1 and I_2 defined in the footnote to Table 7-1. For geometries common to steel panels, explicit form of these integrals are:

$$I_1 = 2c - 2h\frac{\cos\alpha(1-\cos\alpha)}{\sin\alpha} \tag{7-9}$$

$$I_2 = \frac{2((h-x_0)^3 + x_0^3)}{3\sin\alpha} + r_1(h-x_0)^2 + 2r_2x_0^2 \tag{7-10}$$

7.5 Validation of Equivalent in-plane Stiffness for Corrugated Panels

To validate the in-plane equivalent orthotropic plate rigidities of Xia et al. (2012) and address an ambiguity in the edge boundary conditions a series of shell finite element models of square (1016 mm × 1016 mm) corrugated plates (c=50.8 mm, r=25.4 mm, l=61.3 mm, t=6.35 mm, E=210000N/mm2, α=45o) were developed in ABAQUS using S4R elements. The models were exercised with in-plane actions consistent with Figure 7-2: ε_x=constant, ε_y=constant, and γ_{xy}=constant applied as perimeter displacements. These actions define u_x and u_y for the perimeter, but u_z, θ_x, θ_y, and θ_z are undefined and four cases from supported-clamped through out-of-plane free as illustrated in Figure 7-4 are considered. The stiffness predicted by Xia et al. (2012) is compared with the shell FE model in Table 7-2.

From Table 7-2 it is observed that under the right boundary conditions the expressions of Xia et al. (2012) are in excellent agreement with the full corrugated plate shell FE model. The rigidity aligned with the corrugations (A_{22}) is not sensitive to the boundary conditions; however, the rigidity perpendicular to the corrugations (A_{11}, A_{12}) is sensitive.

The source of this sensitivity is the eccentricity between the centroid in the transverse direction and the location where transverse displacements are applied, i.e. the bottom of the corrugation as illustrated in Figure 7-5. The Xia et al (2012) solution agrees best with the assumption of no out-of-plane support (Case 4), thus the engineer must understand that this eccentricity is embedded in the expressions and not account for it a second time in their modeling. Interestingly, the in-plane shear rigidity expressions (A_{66}) agrees best with cases 1 and 3, where the entire perimeter is supported out-of-plane. If this out-of-plane support is removed then the eccentricity effect is activated and the shear stiffness reduces; however Xia et al. (2012) does not account for this effect in shear. Thus, the engineer must be aware that the Xia et al. (2012) expressions may modestly overestimate shear stiffness of the panel.

Table 7-2. Comparison between FEM results and equivalent stiffness

		Corrugated plate shell FE model / $\overline{A_{ij}}$			
	Xia et al. (2012) / Table 1 (N/mm)	Case I Supported-Clamped edge	Case 2 Clamped edge	Case 3 Supported edge	Case 4 "Free" edge
$\overline{A_{22}}$	163910	0.99	0.98	0.99	0.98
$\overline{A_{11}}$	4051	1.38	1.11	1.21	0.97
$\overline{A_{12}}$	1215	1.57	1.29	1.19	0.98
$\overline{A_{66}}$	42489	1.00	0.96	1.00	0.92

Note: if direct rigidities cannot be modeled Eq. (2)-(8) provide E_1=161 MPa, E_2=203500 MPa, ν_{12}=0.00024, ν_{21}=0.3, G_{12}=91170 MPa, t_e=0.286 mm and have been validated to match Xia et al (2012) in the model

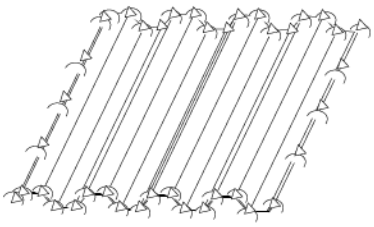

Case 1: Perimeter supported out-of-plane (u_z=0) and clamped (θ_x=θ_y=θ_z=0)

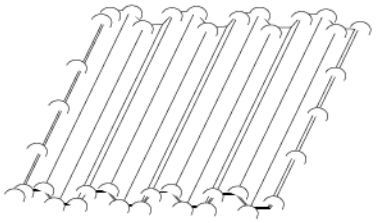

Case 2: Perimeter free out-of-plane but clamped (q_x=q_y=q_z=0)

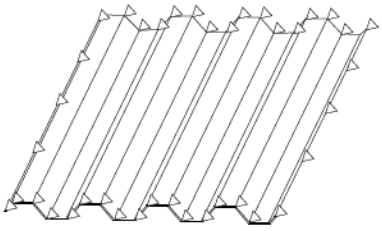

Case 3: Perimeter *supported* out-of-plane (u_z=0) but free to rotate

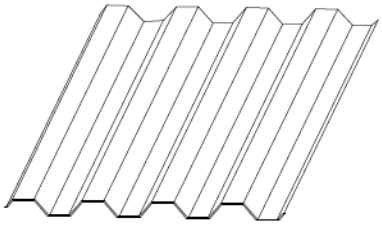

Case 4: Perimeter free, only in-plane applied DOF applied

Figure 7-4. Boundary conditions for corrugated plate with applied in-plane actions

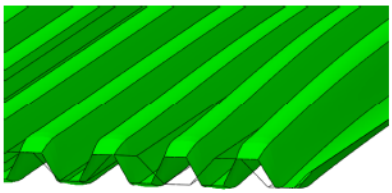

Case 1: Perimeter *supported* out-of-plane (u_z=0) and *clamped* (θ_x=θ_y=θ_z=0)

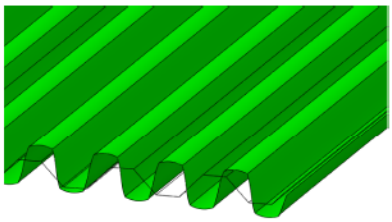

Case 4: Perimeter free, only in-plane applied DOF applied

Figure 7-5. Deformation in FE model under transverse strain

7.6 Impact of Discrete Connection Points and Panels on Diaphragm Stiffness

The previous section validates the in-plane equivalent orthotropic model for an isolated panel under idealized boundary conditions. Actual diaphragms are composed of multiple discrete panels that are connected to one another and to joists and perimeter framing. This

section examines the impact of these details on the realized diaphragm stiffness and the accuracy of the equivalent orthotropic plate model.

Recent testing by Tremblay and Rogers (2004) motivated the geometry studied here. Specifically, an example diaphragm ~ 6 m x 3m in plan employing the P-3615 Canam profile as illustrated in Figure 7-6 is studied. The models in this section do not include the stiffness of fasteners connecting panels or connecting to the frame, but rather treats these locations as discrete constraint points. Thus, the impact of localized forces on the panels is introduced, but the impact of the fastener stiffness is isolated from these effects. This provides an upperbound approximation of the stiffness and one that focuses entirely on the accuracy of the panel modeling. Unlike Figure 7-2, shear in this model is applied in the same manner as in testing with the boundary conditions as illustrated in Figure 7-6(c).

The results, provided in Table 7-3, indicate that only under idealized edge boundary conditions is the equivalent orthotropic plate model adequate. With discrete connection points even though the global deformation is shear the extremely weak stiffness in the transverse corrugation direction (A11 rigidity direction) creates significant local deformations that greatly decrease the overall stiffness. Localized forces (connection points) that are parallel to the corrugation (A22 rigidity direction) do not show similar sensitivity, so the sidelap connections of the model with four discrete panels are not problematic (locally they engage A22 rigidity), rather the perimeter connections that are transverse to the corrugations (in the short direction of the model) create the difficulties Therefore, engineers must be careful when using equivalent orthotropic plate models and

recognize that the derived values do not apply directly to panels with discrete connections transverse to the corrugations, a significant limitation.

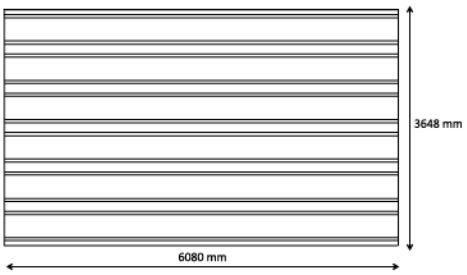

(a) Overall panel dimension

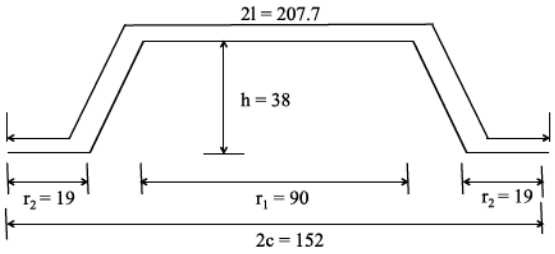

(b) Cross-section dimensions (mm)

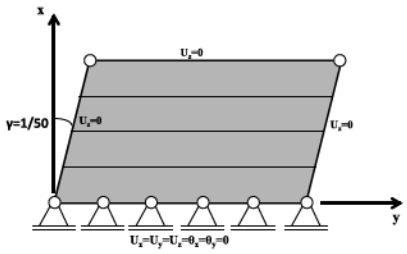

(c) boundary conditions and loading

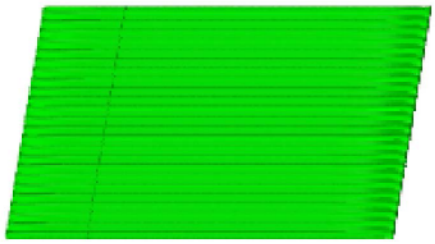

(d) typical response for one large panel

Figure 7-6. Geometry of studied diaphragm

Table 7-3. Elastic shear stiffness for different panels, connection points, and plate models

		FE model (1) corrugations in model	FE model (2) ortho. plate Xia et al.	FE model (3) ortho. plate E_1, E_2, etc.
Panels	Perimeter conn.	S_{FE1} (N/mm)	S_{FE2}/S_{FE1}	S_{FE2}/S_{FE1}
One large panel	Every node	52224	1.0	1.0
One large panel	304 mm o.c.	16676	0.2	0.2
Four discrete panels[a]	Every node	37119	1.1	1.1
Four discrete panels[a]	304 mm o.c.	14687	0.2	0.2

[a] modeling of discrete panels also includes three interior connection lines

7.7 Accuracy of Elastic Buckling Solutions with Orthotropic Plate Models

The elastic buckling response of profiled steel panels is an important consideration in their design. For geometric nonlinear analysis of buildings, as is often pursued for predicting ultimate response, the elastic buckling of the panels is indicative of the potential large deformations the panel may undergo. Elastic shear buckling is known to be sensitive to the details of the profile, here we investigate to what extent an equivalent orthotropic plate can still capture these geometric nonlinearities by investigating the eigenbuckling modes of the panel from the previous section (i.e., Figure 7-6) with explicit FE models of the corrugations compared with equivalent orthotropic plate models.

Selected elastic shear buckling loads and corresponding mode shapes for the three studied models are provided in Table 7-4 and Figure 7-7. The elastic buckling results indicate that panel shear buckling is the lowest buckling mode, but the equivalent orthotropic plate models are inadequate for accurate prediction. The model based on the direct rigidities (including D_{ij}) from Xia et al. (2012) is slightly better than the model based on the use of general engineering parameters (E_1, E_2, etc.) that were fit to the in-plane rigidities (A_{ij}). However, the error is so large that the engineer must use the equivalent plate model with great care for nonlinear analysis. It is interesting to note that in the actual profiles (FE model 1) the buckling mode is not influenced by local edge conditions until the 13th mode, fully 1.5 times higher than the lowest (first) mode.

Table 7-4. First six elastic buckling modes for panel of Figure 7-6 modeled as 4 separate discrete panels connected every 300 mm o.c. at the perimeter and between panels

	FE model (1) corrugations in model		FE model (2) ortho. plate Xia et al.		FE model (3) ortho. plate E_1, E_2, etc.	
mode	V_{cr1} (kN)	notes	V_{cr2} (kN)	notes	V_{cr3} (kN)	notes
1	99	Panel[(a)]	32	Panel[(c)]	26	Panel
3	100	Panel	33	Panel	26	Panel
13	147	Panel	46	Panel	39	Panel
15	148	Panel+Edge[(b)]	50	Panel	41	Panel
21	152	Edge	73	Panel	58	Panel

Note: (a), (b), (c), see Figure 7 for corresponding buckling modes.

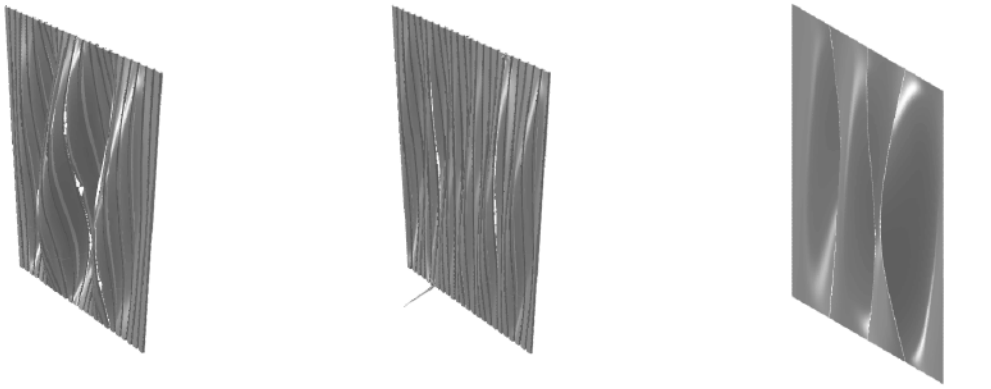

(a) mode 1, FE model 1 (b) mode 15, FE model 1 (c) mode 1, FE model 2

Figure 7-7. Selected elastic buckling modes in shear from models

7.8 Impact of Panel Yielding on Diaphragm Stiffness and Strength

Finite element collapse analyses of four different shell finite element models with explicitly modeled profiles were conducted to study the impact of having discrete panels with discrete connections on their collapse behavior. We employed von Mises yield criteria with isotropic hardening and an elastic perfectly plastic stress-strain curve with F_y=345 MPa and E=203,500 MPa. Loading is the same as Figure 7-6. Four cases are studied (a) the panel is modeled as a single continuous corrugated panel and the perimeter is fully connected, (b) the panel is modeled as 4 discrete panels and the perimeter is fully

connected, (c) the panel is modeled as a single panel and the perimeter is connected at 304 mm o.c., and (d) the panel is modeled as 4 discrete panels and the perimeter is connected at 304 mm o.c. Basic shear deformation-force results are provided in Figure 7-8 and indicate that in the idealized case the perimeter connection has a stronger influence on decreasing the stiffness and strength than the introduction of discrete panels. Additional study is needed including comparison to equivalent orthotropic plate models, but the shell finite element models are able to capture significant variations in the stiffness and strength as a function of expected details and results vary by as much as a factor of five indicating the importance of practical details above and beyond the basic panel properties.

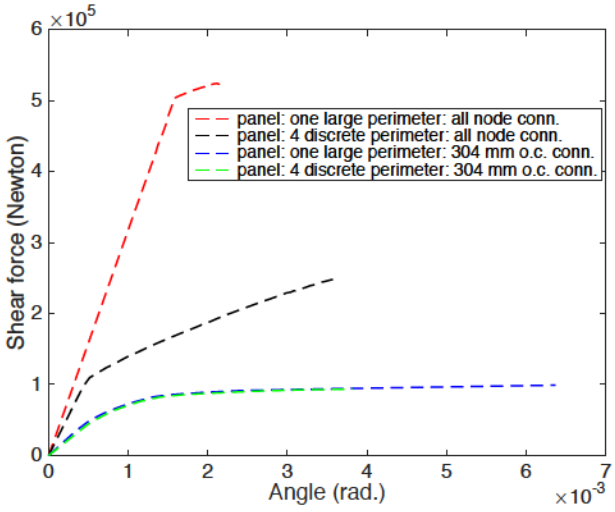

Figure 7-8. Nonlinear load-displacement curves in shear for studied models

7.9 Discussion

The design and behavior of profiled steel panels is complex and includes a number of issues not addressed in this work. Interested readers are referred to AISI S310 (2013) for

design standards, SDI DDM-04 (2015) for examples and additional information related to commonly available panels and connectors.

Reduced order models increase computational efficiency by reducing the degrees of freedom. Completed successfully, all important features are maintained and no compromise is required. The equivalent orthotropic plate reduced order model pursued here can accurately reproduce a variety of complex global stiffness behavior under idealized conditions, and with the explicit expressions of Xia et al. (2012) are relatively easy to implement. However, local features of the model are lost, and when applied in non-idealized conditions these features become important to the response and the accuracy of the model degrades. The application of equivalent orthotropic plate models must be done with care or the results can be overly conservative.

The need to create efficient building structural models is real, and the equivalent orthotropic plates studied herein have some potential, but may still represent too much computational overhead in some situations. Completely phenomenological models with as little as one degree of freedom are also needed and should be pursued in a manner consistent with codified design (strength and stiffness and post-peak response based on standards).

7.10 Conclusions

This chapter examines the application of equivalent orthotropic plate models for profiled steel panels. Two methods for model implementation are explored: direct input of stiffness matrix rigidities, and equivalent thickness and material (E1, E2, etc.) properties.

Under idealized boundary conditions the in-plane stiffness of both implementations of the equivalent orthotropic plate model are shown to have excellent agreement with shell finite element models of profiled steel panels. Relatively complex Poisson effects and bending effects are captured in the equivalent models under idealized conditions. However, under realistic conditions: discrete perimeter fastener spacing, or discrete numbers of panels the equivalent orthotropic plate model fails to capture the global in-plane shear response accurately. Global shear rigidity decreases when discrete fastening is introduced, but local rigidities in the equivalent orthotropic plate model, particularly transverse to the profiles, causes artificially large flexibility and results in stiffness that can be as little as 20% of the actual stiffness. Elastic buckling analysis further highlights this problem for equivalent orthotropic plate models. Reduced order models for profiled steel panels are needed for whole building analysis, equivalent orthotropic plate models provide one possible solution, but the analysis herein shows they must be used with care when exercised in realistic models of buildings.

7.11 Acknowledgement

Partial funding for this work was provided by the Steel Diaphragm Innovation Initiative (SDII) managed by the Cold-Formed Steel Research Consortium headquartered at Johns Hopkins University. SDII receives contributions from the American Institute of Steel Construction, the American Iron and Steel Institute, the Steel Deck Institute, the Steel Joist Institute, and the Metal Building Manufacturers Association. Any opinions, findings and conclusions or recommendations expressed in this material are those of the authors and do not necessarily reflect the views of the sponsors.

7.12 References

[1] ABAQUS. ABAQUS/CAE User's Manual Version 6.12, Simulia. 2012.

[2] AISI S310-13: AISI Standard "North American Standard for the Design of Profiled Steel Diaphragm Panels." American Iron and Steel Institute.

[3] Briassoulis, D. (1986). Equivalent orthotropic properties of corrugated sheets. Computers & Structures, 23(2), 129-138.

[4] Canam Group, (2007). Steel Deck Diaphragm Profile Manual. 2007.

[5] Davies, J. M. (1976). Calculation of steel diaphragm behavior. Journal of the Structural Division, 102(ASCE# 12254).

[6] Easley, J. T., & McFarland, D. E. (1969). "Buckling of light-gage corrugated metal shear diaphragms." Journal of the Structural Division, 95(7), 1497-1516.

[7] Samanta, A., & Mukhopadhyay, M. (1999). "Finite element static and dynamic analyses of folded plates." Engineering Structures, 21(3), 277-287.

[8] Steel Deck Institute, (2015) Diaphragm Design Manual Fourth Edition. 2015

[9] Xia, Y., Friswell, M. I., & Flores, E. S. (2012). "Equivalent models of corrugated panels." International Journal of Solids and Structures, 49(13), 1453-1462.

CHAPTER 8

SHELL FINITE ELEMENT MODELING OF ELASTIC SHEAR STIFFNESS OF BARE STEEL DECK DIAPHRAGM

8.1 Abstract

The objective of this chapter is to explore elastic shear stiffness of bare steel deck diaphragms through high fidelity finite element modeling. Profiled steel panels, i.e, metal deck, often serve as a key distribution element in building lateral force resisting systems. Acting largely as an in-plane shear diaphragm, metal deck as employed in walls, roofs, and floors plays a key role in creating and driving three-dimensional building response. Accurate prediction of shear stiffness is needed to better understand the shear behavior of bare steel deck. According to the shear stiffness expression in AISI S310 or SDI's DDM, total shear deformation can be separated into three parts: pure shear deformation, warping deformation, and connection slip. In this chapter, bare deck finite element models were built with typical fastener layouts from the DDM. The shear condition was performed on the models by imposing deformations at the edge node. By changing boundary conditions, these shear deformation terms can be separated and the values of shear stiffness were compared with DDM expressions. The results showed that the prediction of shear stiffness from pure shear deformation and connection slip from finite element modeling agreed well with the DDM prediction. The warping stiffness from DDM is smaller than finite element predictions. DDM uses a simplified model to predict warping deformation and this model may need to be revised.

8.2 Introduction

Profiled steel panels, i.e., metal deck, are roll-formed from thin steel sheet and can result in simple corrugated shapes or relatively complex longitudinal profiles with additional transverse features such as embossments (Figure 8-1a). These panels serve as the walls and roof in many metal buildings, see Figure 8-1b, and form an integral component of common floor systems in a wide variety of buildings. Under lateral loads the panels play a particularly important role as a distribution element, one in which the in-plane shear behavior of the panel is paramount. A typical profiled steel panel roof is illustrated in Figure 8-1. When distributing lateral load this system acts as a diaphragm, with all elements in the system contributing: panel, panel inter-connections, joists, joist-to-panel connections, primary framing, and framing-to-panel connections.

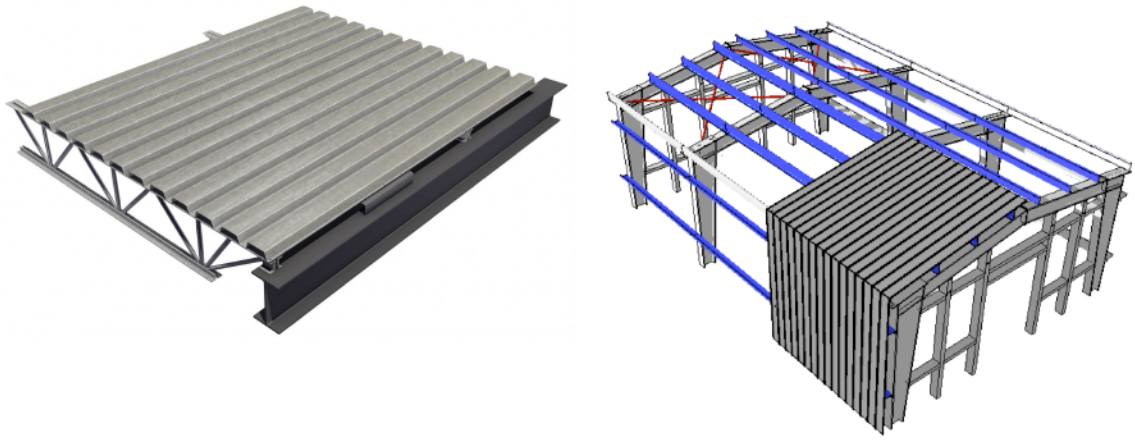

(a) Bare steel deck[1] (b) Metal building with deck[2]

Figure 8-1. Metal deck in building

Figure 8-2 shows the deformed shape of bare steel deck under shear.

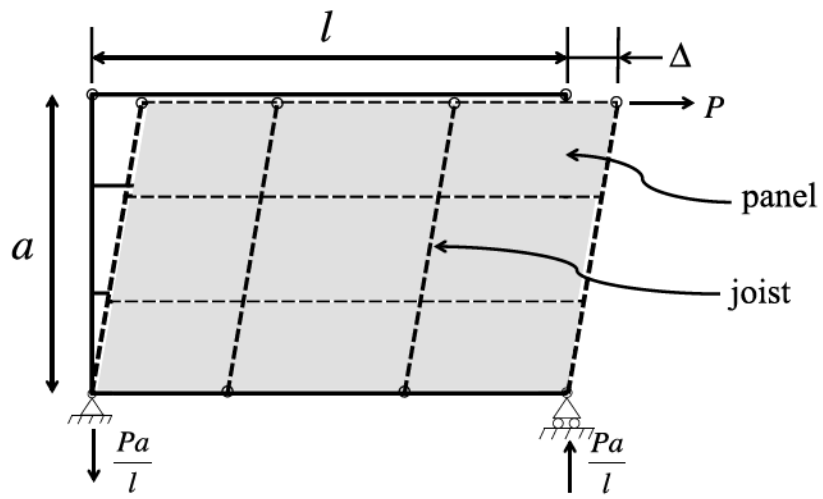

Figure 8-2. Steel deck panel under pure shear and its displacement

From AISI S310 or the Diaphragm Design Manual (DDM, DDM04 was published in 2016 and used herein), shear stiffness *G'* of the bare deck diaphragm is defined as:

$$G' = Gt = \frac{P/l}{\Delta/a} = \frac{Pa/l}{\Delta} \tag{8-1}$$

Where, P is the applied shear load and l, a are the panel length and width and t is the thickness. Δ is the total panel deformation under shear loading. Panel deformation comes from three terms: shear deformation of the panel Δ_s, warping deformation Δ_d, and connection slip Δ_c. Therefore, Eq. 8-1 can be written as following:

$$G' = \frac{Pa/l}{\Delta_s + \Delta_d + \Delta_c} \tag{8-2}$$

8.3 Description of Bare Deck Models

To understand the shear behavior of a bare deck diaphragm, Shell finite element (FE) models were built and compared with DDM's prediction. pure shear boundary conditions were enforced by imposing shear displacement at the panel edge and any interior purlin/joist nodes (the same as shown in Fig. 8-2). In the models, from Eq. 8-1, by dividing the total reaction force by the rotation angle we can obtain the bare deck shear stiffness.

Table 8-1. Modeling matrix

across corrugation		along corrugation (in.)						
designation	spacing (in.)	12	6	4	3	2	0[c]	0[d]
36/4	12	✔	✔	–	–	–	✔	✔
36/5	12	✔	✔	–	–	–	✔	✔
36/7	6	–	✔	✔	✔	✔	✔	✔
36/9	6	–	✔	✔	–	–	✔	✔
bottom	(a)	✔	–	–	–	–	✔	✔
every	(b)	✔	–	–	–	–	✔	✔

(a) single row of all FE nodes in the bottom of the flute are connected and experience imposed shear displacements
(b) entire end cross-section are connected in a rigid plane and experience imposed shear displacements (warping restricted)
(c) no sidelap, model uses continuous deck equivalent to perfect fastening (ideal case)
(d) every node along a line connected driven to imposed shear displacement

In steel deck testing or in real construction, all shear forces are transferred to the neighboring deck or frame through sidelap or deck-to-frame (structural) connections. In our FE models, each diaphragm is made of four separate pieces of deck. In our FE models all imposed shear deformation act at connection locations. The considered fastener layouts in both directions along the deck are shown in Table 8-1. These fastener layouts are typical cases from DDM04 Chapter 9 augmented with some additional ideal cases. For the parallel-to-purlin/joist direction, there are four different cases while for the perpendicular-to-purlin/joist direction there are five cases, as shown in Fig. 8-3.

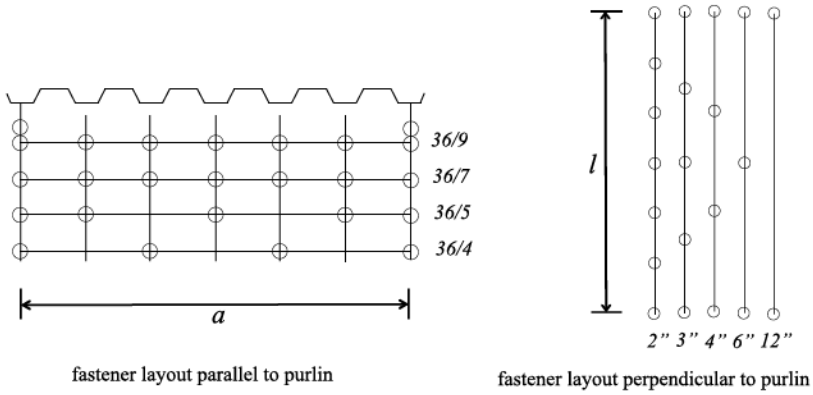

Figure 8-3. Fastener pattern in the models

Some special fastener layout cases (Table 1 a, b, c, and d) can affect the deformation term. By imposing displacement at all edge nodes in the parallel-to-purlin/joist direction, warping can be eliminated, while by imposing displacement at all edge nodes in the perpendicular-to-purlin direction connection slip can be eliminated. By modeling a whole panel board (12' wide), instead of four different panels, the effect of the sidelap connection can be examined.

A typical B type WR deck cross section is selected as shown in Fig. 8-4.

According to the three terms contributing to the shear deformation of the diaphragm (see Eq. 8-2), our models can be divided into four categories:

The first category: shear deformation is contributed to by Δ_s, Δ_d and Δ_c;

The second category: shear deformation is contributed to by Δ_s and Δ_d (no connection slip);

The third category: shear deformation is contributed to by Δ_s and Δ_c (no edge warping);

The fourth category: shear deformation is contributed by Δ_s only (no warping and connection slip)

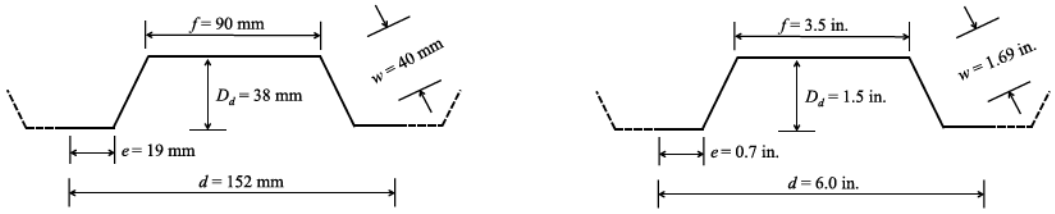

(a) unit: mm (b) unit: inch

Figure 8-4. Steel deck panel cross section dimensions

According to the three terms contributing to the shear deformation of the diaphragm (see Eq. 8-2), models can be divided into four categories:

The first category: shear deformation is contributed to by Δ_s, Δ_d and Δ_c;

The second category: shear deformation is contributed to by Δ_s and Δ_d (no connection slip);

The third category: shear deformation is contributed to by Δ_s and Δ_c (no edge warping);

The fourth category: shear deformation is contributed by Δ_s only (no warping and connection slip)

Panel dimension and length-to-width ratio is another factor that can potentially affect the shear behavior of the bare deck. Therefore, for each model in Table 8-1, the dimension and length-to-width ratio were changed. The length width ratio of each model changes

from 0.25 to 4, as shown in Fig. 8-5. (Note that here 'length' means the direction perpendicular to the purlin and 'width' is the direction parallel to the purlin) This 'length-to-width ratio' can affect the warping behavior and connection behavior of the panel.

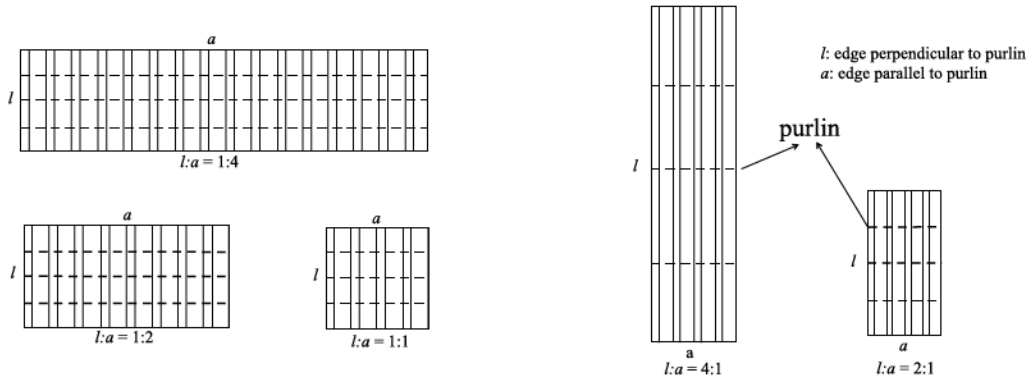

(a) (b)

Figure 8-5. Steel deck panels with different aspect ratios

8.4 Evaluation of Shear Stiffness from Diaphragm Design Manual (DDM)

8.4.1 Mechanism of Shear Deformation

As discussed in the last section, in Eq. 8-2 the denominator is the summation of three terms according to the shear deformation mechanism. If the shear stiffness is treated as three separate terms, Eq. 8-2 can be written as:

$$G' = \frac{1}{\frac{1}{G_s'} + \frac{1}{G_c'} + \frac{1}{G_d'}} \tag{8-3}$$

Explicit expressions for the Δ terms in Eq. 8-2 are provided in DDM04, and result in the following:

$$G' = \frac{Et}{2(1+\nu)\frac{s}{d} + D_n + C} \tag{8-4a}$$

or

$$G' = \frac{1}{\frac{2(1+\nu)\frac{s}{d}}{Et} + \frac{D_n}{Et} + \frac{C}{Et}} \tag{8-4b}$$

Details of the parameters in Eq. 8-4 (a) and (b) are explained below.

8.4.2 Shear Stiffness from Panel Shear Deformation G_s'

The first term in the denominator of Eq. 8-4 (b) represents the deformation caused by panel shear deformation. If shear stiffness is defined for pure panel deformation, the expression for G_s' will be:

$$G_s' = \frac{Et}{2(1+\nu)\frac{s}{d}} \quad or \quad \frac{Gt}{\frac{s}{d}} \tag{8-5}$$

For our models, the developed flute width per width:

$$s = 2(e+w)+f \tag{8-6}$$

Where *e, w and f* are all cross section dimensions (See Fig. 8-4). Panel corrugation pitch d = 152 mm.

Substituting values into Eq. 8-5, G_s' becomes 52149.3 N/mm (298.0 kip/in.), which is the DDM prediction for panel shear stiffness from pure panel deformation.

8.4.3 Shear Stiffness from Warping Deformation G_d'

The second term in the denominator of Eq. 8-4 (b) represents the deformation caused by warping deformation. Per DDM the shear stiffness for warping deformation is:

$$G_d' = \frac{Et}{D_n} \tag{8-7}$$

Where D_n is the warping coefficient shown below.

$$D_n = \frac{D}{L} \tag{8-8}$$

Where D is the warping constant given in DDM04 Table 3.3-2 and L is the panel length. The effect of D_n is often reduced to ρD_n depending on the number of equal spans within the panel.

G_d' is defined in the table below.

The origins of the G_d' prediction can be found in DDM 01 (1981). The model assumes the top flange "warping" movement is restrained by an elastic foundation coming from the transverse stiffness of the web.

Table 8-2. G_d' calculated from Diaphragm Design Manual
(a) in unit N/mm

across corrugation	along corrugation	aspect ratio 1:4	1:2	1:1	2:1	4:1
36/4	12	4303.1	4303.1	4303.1	8606.2	17212.4
	6	4303.1	4303.1	4303.1	8606.2	17212.4
36/5	12	6080.7	6080.7	6080.7	12161.5	24322.9
	6	6080.7	6080.7	6080.7	12161.5	24322.9
36/7	6	35941.4	35941.4	35941.4	71882.8	143765.7
	4	35941.4	35941.4	35941.4	71882.8	143765.7
	3	35941.4	35941.4	35941.4	71882.8	143765.7
	2	35941.4	35941.4	35941.4	71882.8	143765.7
36/9	6	35941.4	35941.4	35941.4	71882.8	143765.7
	4	35941.4	35941.4	35941.4	71882.8	143765.7

(b) in unit kip/inch

across corrugation	along corrugation	aspect ratio 1:4	1:2	1:1	2:1	4:1
36/4	12	24.6	24.6	24.6	49.2	98.4
	6	24.6	24.6	24.6	49.2	98.4
36/5	12	34.7	34.7	34.7	69.5	139.0
	6	34.7	34.7	34.7	69.5	139.0
36/7	6	205.4	205.4	205.4	410.8	821.5
	4	205.4	205.4	205.4	410.8	821.5
	3	205.4	205.4	205.4	410.8	821.5
	2	205.4	205.4	205.4	410.8	821.5
36/9	6	205.4	205.4	205.4	410.8	821.5
	4	205.4	205.4	205.4	410.8	821.5

8.4.4 Shear Stiffness from Connection Slip G_c'

The last term in the denominator of Eq. 8-4 (b) represents the deformation caused by connection slip. If shear stiffness is defined for connection slip, it is:

$$G_c' = \frac{Et}{C} \tag{8-9}$$

In Eq. 8-9, C is the slip coefficient and is defined in AISI S310 or DDM04 as:

$$C = E\frac{t}{w}S_f\left(\frac{2}{2\alpha_1 + n_p\alpha_2 + 2n_s\frac{S_f}{S_s}}\right)l \tag{8-10}$$

Where S_f is the structural connection flexibility and S_s is the sidelap connector flexibility. For an ideal case with equal fasteners employed for sidelap and from connections, noting that the sidelap has two sides of panels and panel-to-framing has only one side of panel, then:

$$S_f = \frac{S_s}{2} \tag{8-11}$$

Eq. 8-10 then becomes:

$$G_c' = \frac{1}{S_f}\frac{w}{l}\left(\frac{2\alpha_1 + n_p\alpha_2 + n_s}{2}\right) \tag{8-12}$$

In which:

α_1 is end distribution factor.

α_2 is the same as α_1.

n_p is the number of purlins. n_p=3 for all models here.

n_s is the number of stitch connectors within the length L.

α_1, α_2, n_p and n_s can be obtained from DDM04 Section 2.2.

The result of G_c' calculated from Eq. 8-12 is provided in Table 8-3.

Table 8-3. G_c' calculated from Diaphragm Design Manual
(a): in unit N/mm

across corrugation	along corrugation	aspect ratio 1:4	1:2	1:1	2:1	4:1
36/4	12	38504.5	38504.5	38504.5	41573.7	43108.3
	6	83147.3	83147.3	83147.3	86216.5	87751.1
36/5	12	41480.7	41480.7	41480.7	43061.8	43852.3
	6	86123.5	86123.5	86123.5	87704.6	88495.2
36/7	6	89285.7	89285.7	89285.7	89285.7	89285.7
	4	133928.6	133928.6	133928.6	133928.6	133928.6
	3	178571.4	178571.4	178571.4	178571.4	178571.4
	2	267857.1	267857.1	267857.1	267857.1	267857.1
36/9	6	120907.7	120907.7	120907.7	105096.7	97191.2
	4	172991.1	172991.1	172991.1	157180.1	149274.6

(b): in unit kip/inch

across corrugation	along corrugation	aspect ratio 1:4	1:2	1:1	2:1	4:1
36/4	12	220.0	220.0	220.0	237.6	246.3
	6	475.1	475.1	475.1	492.7	501.4
36/5	12	237.0	237.0	237.0	246.1	250.6
	6	492.1	492.1	492.1	501.2	505.7
36/7	6	510.2	510.2	510.2	510.2	510.2
	4	765.3	765.3	765.3	765.3	765.3
	3	1020.4	1020.4	1020.4	1020.4	1020.4
	2	1530.6	1530.6	1530.6	1530.6	1530.6
36/9	6	690.9	690.9	690.9	600.6	555.4
	4	988.5	988.5	988.5	898.2	853.0

Note: S_f is estimated from isolated finite element models. Details in Section 8-4.

8.5 Description of Finite Element Models in ABAQUS

In ABAQUS a series of models are developed. Linear elastic isotropic material is used for cold-formed steel. Material Young's modulus is 203500 N/mm^2 (29500 ksi) with Poisson's ratio at 0.3. S4R element is used. Single step linear elastic analysis (linear perturbation) was conducted under the shear boundary condition. To simulate the pure shear behavior, shear displacement was imposed at the edge fasteners and purlin fasteners. Out of plane movement and rotational degrees of freedom are constrained at edge nodes. Boundary condition details are illustrated in Fig. 8-6.

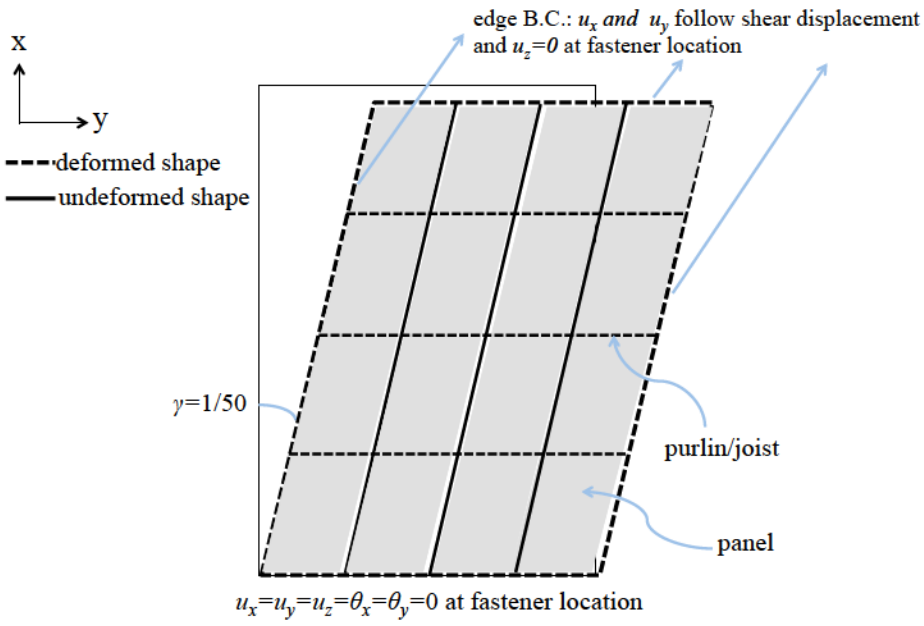

Figure 8-6. Boundary condition in ABAQUS models

The undeformed model (at aspect ratio 1) in ABAQUS and details of boundary condition are shown in Fig. 8-7.

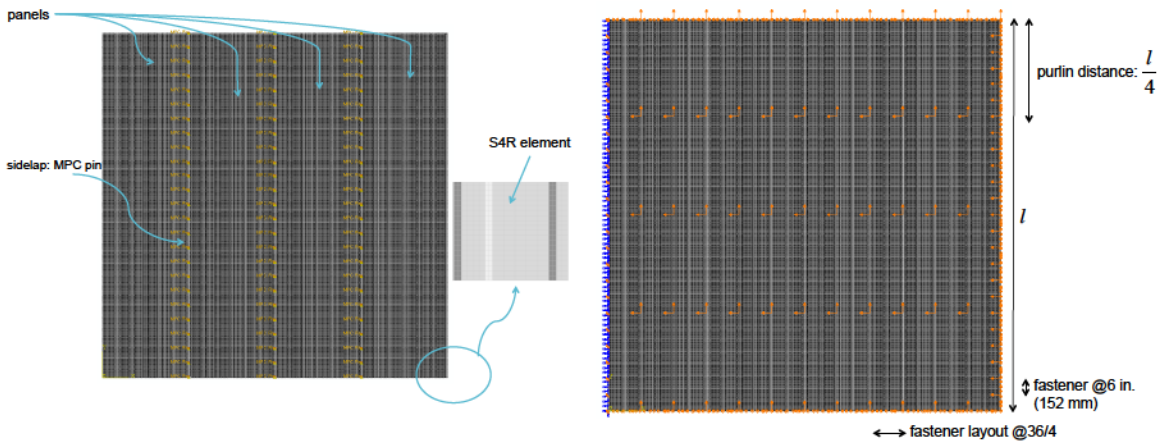

Figure 8-7. Undeformed shape of shell FE model (fastener layout: 36/4-6)

Fig. 8-8 (a), (b) and (c) provide three representative models at aspect ratio 1:4, 1:1 and 4:1 with deformed shape. Fig. 8-8 (d) illustrated the local deformation at fastener locations.

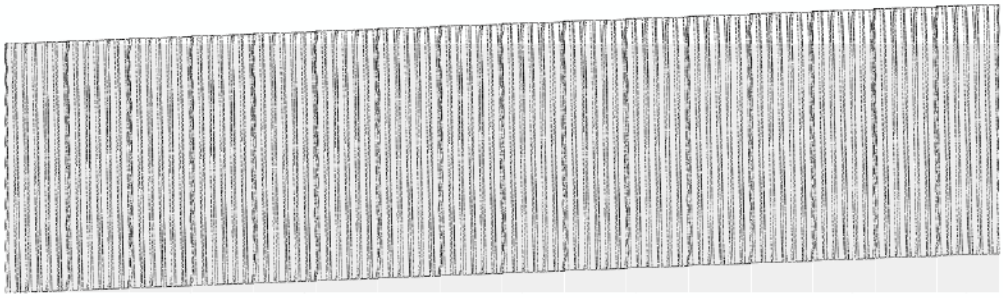

(a) Deformed shape of FE model with aspect ratio 1:4

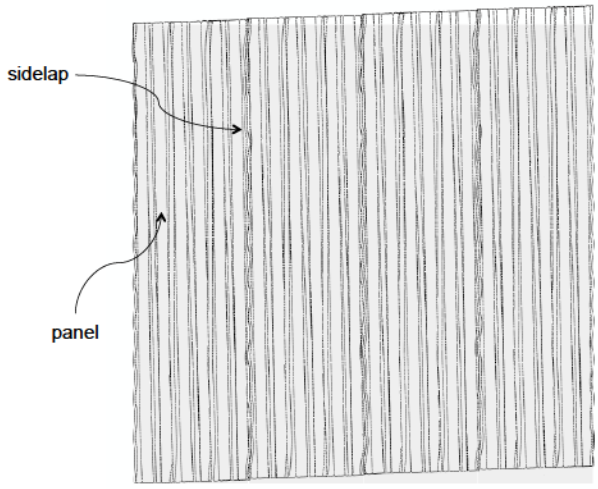

(b) Deformed shape of FE model with aspect ratio 1:1

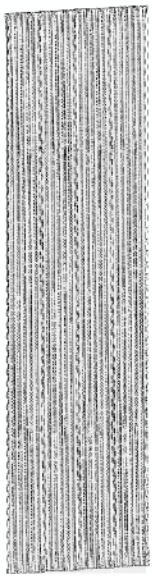

(c) Deformed shape of FE model with aspect ratio 4:1

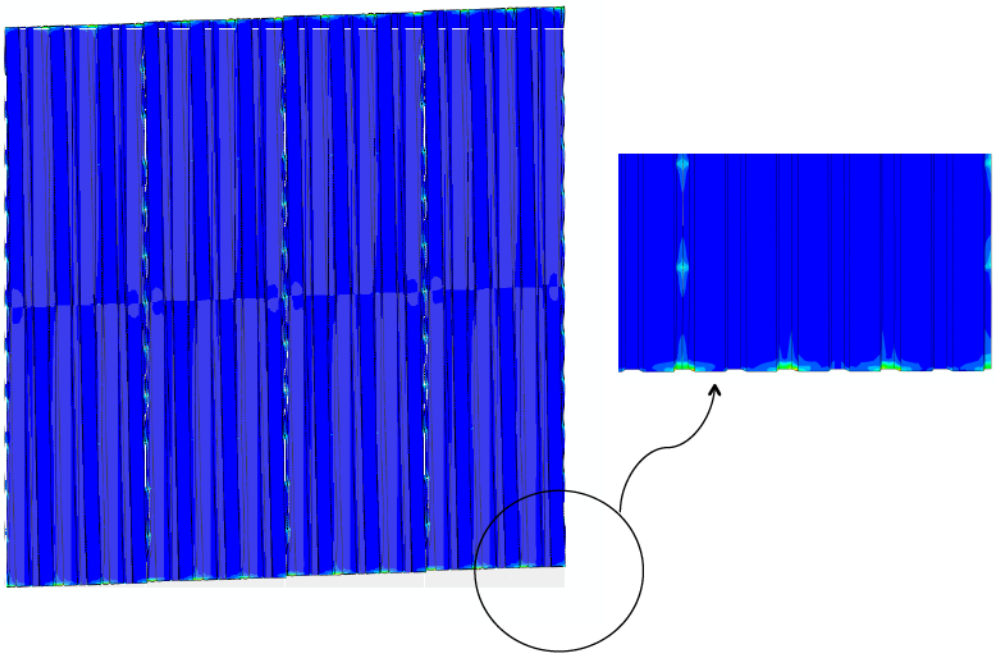

(d) local deformation in model

Figure 8-8. Deformed shape of selected finite element models

To estimate S_f and S_s in Eq. 8-12, representative finite element models with the same boundary condition as in pure shear were built, and a unit load was imposed at a single fastener location. The finite element models are illustrated in Fig. 8-9 (a) and (b). Since connections in all models are ideal and their stiffness is infinity, S_f and S_s here include local plate deformation around connections in the shell finite element models. The resulting flexibility are S_f=3.3×10^{-5} mm/N and S_s=6.6×10^{-5} mm/N. Note in this case S_f= $S_s/2$. In actual diaphragms different types of connectors are used.

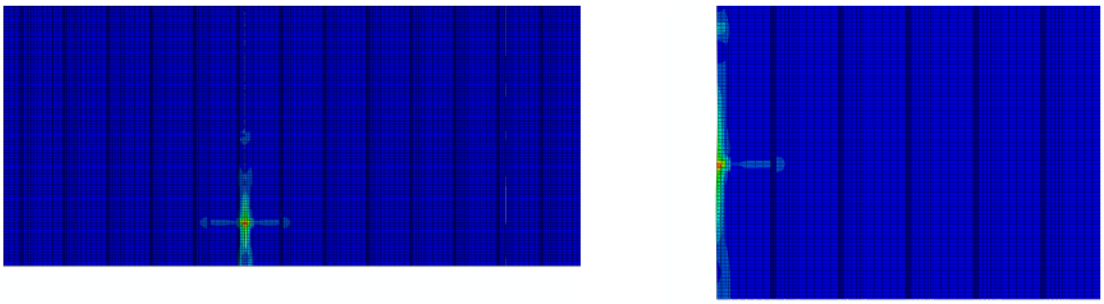

(a) model to evaluate S_s (b) model to evaluate S_f

Figure 8-9. Finite element models to evaluate S_f and S_s

8.6 Evaluation of Shear Stiffness from Finite Element Modeling

8.6.1 Overall Result

In Eq. 8-1, Δ/a (shear angle) =1/50 for all FE models. Therefore, shear stiffness of the panel deck can be obtained from the following:

$$G' = \frac{P/l}{\Delta/a} = \frac{50P}{l} \tag{8-13}$$

Where P is the reaction force and l is panel length.

With finite element results and Eq. 8-13, elastic shear stiffness of all the models is calculated. Results are shown in Table 8-4. From the results, can see that as the aspect ratio of the models changes from 1:4 to 1:1, the shear stiffness doesn't change. However, when the ratio is larger than 1, as the ratio increases, the elastic stiffness increases.

In all discrete fastener layout cases, the deformation is contributed to by the three terms in Eq. 8-2. For the special boundary conditions in the last two rows of Table 8-4, we can separate either shear deformation caused by warping or by connection slip. The effect of fastener layout on shear stiffness is provided in next sections.

To illustrate how the elastic shear stiffness increases and converges as the aspect ratio increases, additional models were completed with aspect ratio from 0.1 to 10. From the results, as shown in Fig. 8-10, we can see that the shear stiffness asymptotically converges to a constant at large aspect ratio. A model with aspect ratio of 50 is deemed large enough to estimate the asymptote.

Table 8-4. Shear stiffness from finite element models
(a): in unit N/mm

perimeter fastener spacing			field (interior) fastener spacing			panel dimensions and aspect ratio				
across corrugation		along corr.	across corrugation		along corr.	a(ft)	12	12	12	24	48
						b(ft)	48	24	12	12	12
designation	spacing (in.)	spacing (in.)	designation	spacing (in.)	spacing (in.)	a/4 (ft)[e]	3	3	3	6	12
						(a/b)	0.25	0.5	1	2	4
	12	12		12	12		11418.6	11418.6	11418.6	15347.0	18224.8
	12	12		12	0[c]		12078.5	12078.5	12078.5	18476.2	25934.6
36/4	12	6	36/4	12	6		14483.1	14483.1	14483.1	20820.2	26337.9
	12	6		12	0[c]		14795.8	14795.8	14795.8	22550.8	30742.1
	12	0[d]		12	0[d]		17203.6	17203.6	17203.6	25871.3	34374.3
	12	12		12	12		11730.5	11730.5	11730.5	15738.8	18727.0
	12	12		12	0[c]		12494.1	12494.1	12494.1	18955.8	26691.9
36/5	12	6	36/5	12	6		16881.4	16881.4	16881.4	22642.1	27896.8
	12	6		12	0[c]		17248.4	17248.4	17248.4	24528.0	32614.6
	12	0[d]		12	0[d]		22512.5	22512.5	22512.5	29606.5	37354.0
	6	6		6	6		22916.7	22916.7	22916.7	28344.7	31906.6
	6	6		6	0[c]		23376.4	23376.4	23376.4	30836.1	37745.2
	6	4		6	4		26812.9	26812.9	26812.9	32836.9	37090.5
	6	4		6	0[c]		27109.0	27109.0	27109.0	34103.8	40560.8
36/7	6	3	36/7	6	3		27805.9	27805.9	27805.9	34313.8	38802.2
	6	3		6	0[c]		28056.1	28056.1	28056.1	35644.0	41795.1
	6	2		6	2		29538.2	29538.2	29538.2	36406.2	41215.0
	6	2		6	0[c]		29684.6	29684.6	29684.6	37223.1	43041.5
	6	0[d]		6	0[d]		32444.3	32444.3	32444.3	39631.0	44817.6
	6	6		6	6		24123.2	24123.0	24123.0	28808.0	32162.0
	6	6		6	0[c]		24567.1	24567.1	24567.1	31485.0	38063.0
36/9	6	4	36/9	6	4		27223.0	27223.0	27223.0	32834.0	36841.0
	6	4		6	0[c]		27549.4	27549.4	27549.4	34546.9	40787.0
	6	0[d]		6	0[d]		32574.9	32574.9	32574.9	39780.3	44947.9
	(a)	12		(a)	12		9886.6	9886.6	9886.6	15207.3	18837.2
bottom	(a)	12	bottom	(a)	0[c]		10224.3	10224.3	10224.3	17357.7	26023.3
	(a)	0[d]		(a)	0[d]		36288.1	36288.1	36288.1	42034.4	46262.8
	(a)	0[d]		(a)	0[c]		36338.3	36338.3	36338.3	42069.0	46280.5
	(b)	12		(b)	12		8963.7	8963.7	8963.7	14296.3	18790.3
every	(b)	12	every	(b)	0[c]		9184.9	9184.9	9184.9	15100.8	22752.9
	(b)	0[d]		(b)	0[d]		52758.4	52758.4	52758.4	52419.4	52290.6
	(b)	0[d]		(b)	0[c]		52758.4	52758.4	52758.4	52419.4	52290.6

(b): in unit kip/inch

perimeter fastener spacing			field (interior) fastener spacing			panel dimensions and aspect ratio				
across corrugation		along corr.	across corrugation		along corr.	a(ft)	12	12	12	24	48
						b(ft)	48	24	12	12	12
designation	spacing (in.)	spacing (in.)	designation	spacing (in.)	spacing (in.)	a/4 (ft)[e]	3	3	3	6	12
						(a/b)	0.25	0.5	1	2	4
	12	12		12	12		65.2	65.2	65.2	87.7	104.1
	12	12		12	0[c]		69.0	69.0	69.0	105.6	148.2
36/4	12	6	36/4	12	6		82.8	82.8	82.8	119.0	150.5
	12	6		12	0[c]		84.5	84.5	84.5	128.9	175.7
	12	0[d]		12	0[d]		98.3	98.3	98.3	147.8	196.4
	12	12		12	12		67.0	67.0	67.0	89.9	107.0
	12	12		12	0[c]		71.4	71.4	71.4	108.3	152.5
36/5	12	6	36/5	12	6		96.5	96.5	96.5	129.4	159.4
	12	6		12	0[c]		98.6	98.6	98.6	140.2	186.4
	12	0[d]		12	0[d]		128.6	128.6	128.6	169.2	213.5
	6	6		6	6		131.0	131.0	131.0	162.0	182.3
	6	6		6	0[c]		133.6	133.6	133.6	176.2	215.7
	6	4		6	4		153.2	153.2	153.2	187.6	211.9
	6	4		6	0[c]		154.9	154.9	154.9	194.9	231.8
36/7	6	3	36/7	6	3		158.9	158.9	158.9	196.1	221.7
	6	3		6	0[c]		160.3	160.3	160.3	203.7	238.8
	6	2		6	2		168.8	168.8	168.8	208.0	235.5
	6	2		6	0[c]		169.6	169.6	169.6	212.7	246.0
	6	0[d]		6	0[d]		185.4	185.4	185.4	226.5	256.1
	6	6		6	6		137.8	137.8	137.8	164.6	183.8
	6	6		6	0[c]		140.4	140.4	140.4	179.9	217.5
36/9	6	4	36/9	6	4		155.6	155.6	155.6	187.6	210.5
	6	4		6	0[c]		157.4	157.4	157.4	197.4	233.1
	6	0[d]		6	0[d]		186.1	186.1	186.1	227.3	256.8
	(a)	12		(a)	12		56.5	56.5	56.5	86.9	107.6
bottom	(a)	12	bottom	(a)	0[c]		58.4	58.4	58.4	99.2	148.7
	(a)	0[d]		(a)	0[d]		207.4	207.4	207.4	240.2	264.4
	(a)	0[d]		(a)	0[c]		207.6	207.6	207.6	240.4	264.5
	(b)	12		(b)	12		51.2	51.2	51.2	81.7	107.4
every	(b)	12	every	(b)	0[c]		52.5	52.5	52.5	86.3	130.0
	(b)	0[d]		(b)	0[d]		301.5	301.5	301.5	299.5	298.8
	(b)	0[d]		(b)	0[c]		301.5	301.5	301.5	299.5	298.8

(a) single row of all FE nodes in the bottom of the flute are connected and experience imposed shear displacements
(b) entire end cross-section are connected in a rigid plane and experience imposed shear displacements (warping restricted)
(c) no sidelap, model uses continuous deck equivalent to perfect fastening (ideal case)
(d) every node along a line connected driven to imposed shear displacement

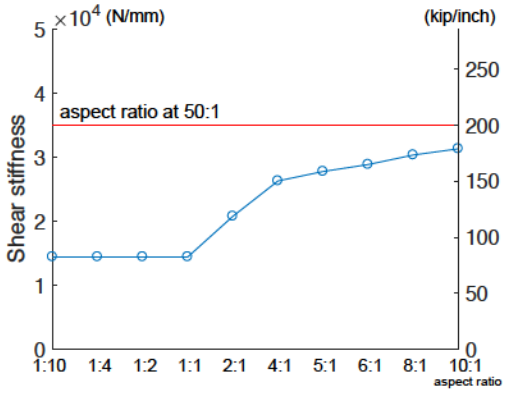

(a) 36/4-6

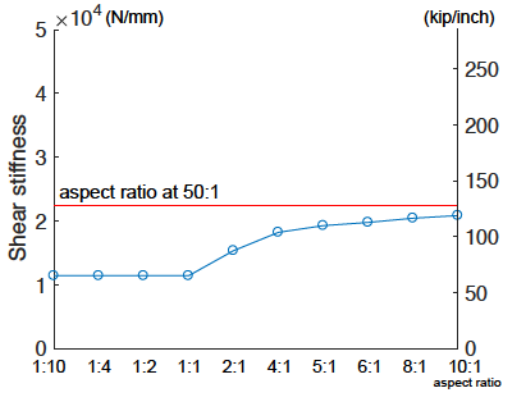

(b) 36/4-12

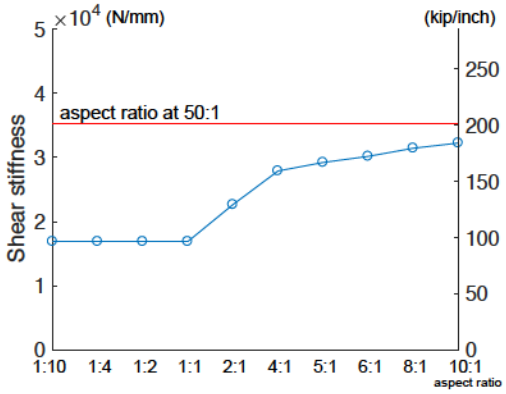

(c) 36/5-6

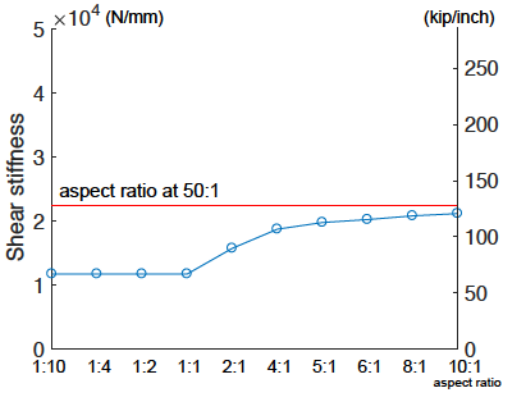

(d) 36/5-12

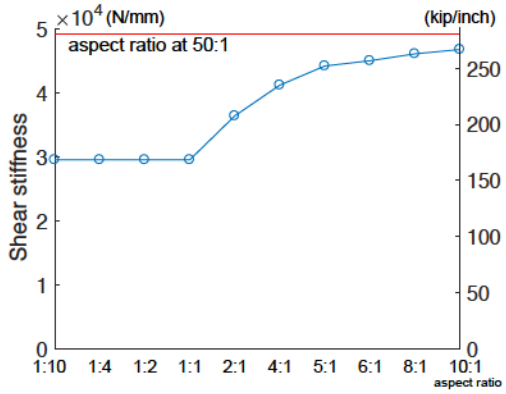

(e) 36/7-2

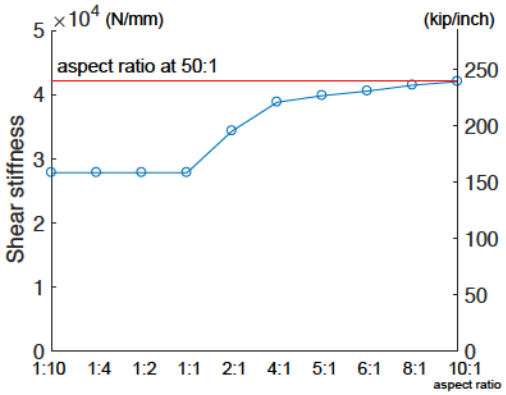

(f) 36/7-3

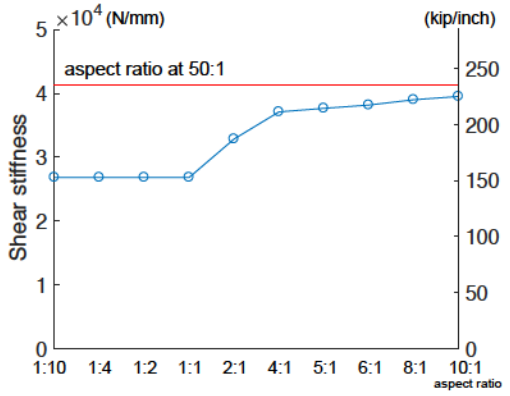

(g) 36/7-4

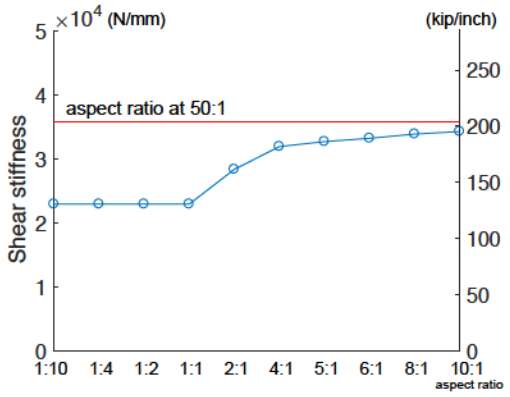

(h) 36/7-6

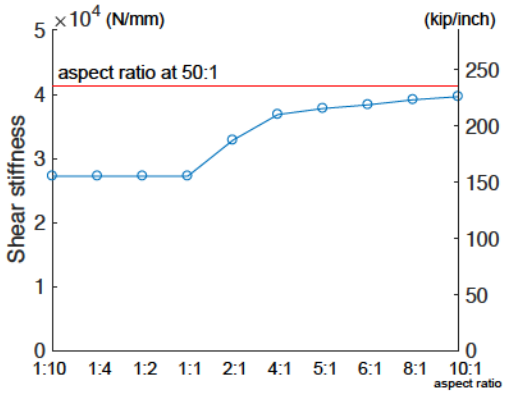

(i) 36/9-4

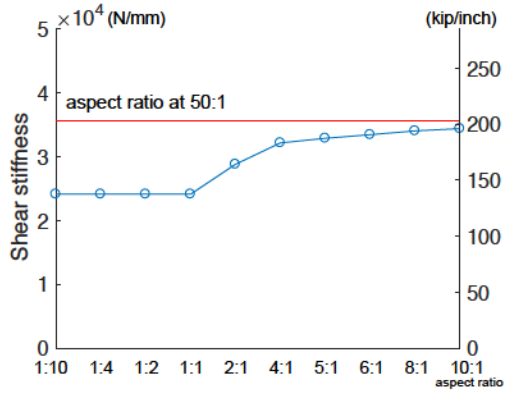

(j) 36/9-6

Figure 8-10. Shear stiffness *G'* of different models, designated by fastener layout across and along corrugation

8.6.2 Effect of Sidelap Connection

Sidelap connections decrease shear stiffness of the bare deck by connection slip. For any model with a given fastener layout, there are two sets of models: the first includes discrete panels and sidelaps, the second has one whole panel with no sidelap. Table 8-5 shows the ratio of shear stiffness *G'* between the two models with the same fastener layout and dimension. Table 8-5 shows that the sidelap effect is not very significant for most models with aspect ratio less than 1. As model length increases there are more

sidelap connectors and the effect becomes more significant. Generally, the factor decreases as the dimension ratio increases, but still no less than 0.7. The results of Table 8-5 depend on 'perfect' sidelap connectors – it only considers panel local deformation instead of connection failure. Thus this gives only an idea of the influence of local panels flexibility on overall stiffness. It is known that if the sidelap fasteners are highly flexible this can dominate the full response.

Table 8-5. Ratio of shear stiffness between models w/o and w/ sidelap

across corrugation	along corrugation	aspect ratio 1:4	1:2	1:1	2:1	4:1
36/4	12	0.95	0.95	0.95	0.83	0.70
	6	0.98	0.98	0.98	0.92	0.86
36/5	12	0.94	0.94	0.94	0.83	0.70
	6	0.98	0.98	0.98	0.92	0.86
36/7	6	0.98	0.98	0.98	0.92	0.85
	4	0.99	0.99	0.99	0.96	0.91
	3	0.99	0.99	0.99	0.96	0.93
	2	1.00	1.00	1.00	0.98	0.96
36/9	6	0.98	0.98	0.98	0.91	0.84
	4	0.99	0.99	0.99	0.95	0.90
bottom	12	0.97	0.97	0.97	0.88	0.72
	every	1.00	1.00	1.00	1.00	1.00
every	12	0.98	0.98	0.98	0.95	0.83
	every	1.00	1.00	1.00	1.00	1.00

8.6.3 Effect of Connections Parallel to Purlins

From Figure 8-11 we can see that as the number of fasteners is increased at the edge and purlins, shear stiffness of the bare steel deck increases. For different dimension aspect ratios, the increase in shear stiffness follows a similar magnitude. As in the Diaphragm Design Manual (DDM04), there is almost double the shear stiffness if the fastener layout is changed from 36/4 to 36/9 at 6 in. connector spacing at the other direction.

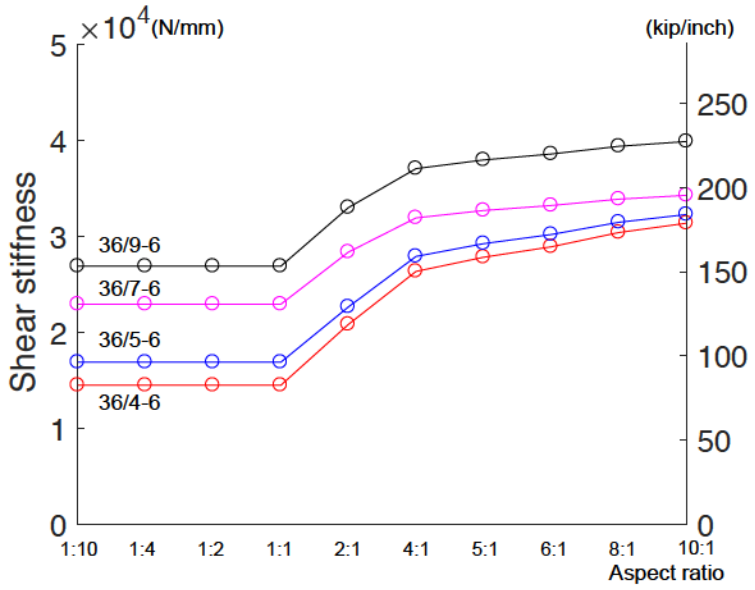

Figure 8-11. Effect of connections parallel to purlin

8.6.4 Effect of Connections Perpendicular to Purlins

With a fixed fastener layout in the parallel-to-purlin direction (36/7 in the figure below), as fasteners increase in the other direction, shear stiffness changes. In Fig. 8-12, as the fastener layout changes from 36/7-6 to 36/7-2, shear stiffness changes from 2.2×10^4 N/mm (120 kip/inch) to 3×10^4 N/mm (170 kip/inch) at low aspect ratio. The magnitude of increase for higher aspect ratio will increase, e.g.: from 35000 N/mm (200 kip/inch) to 47200 N/mm (270 kip/inch).

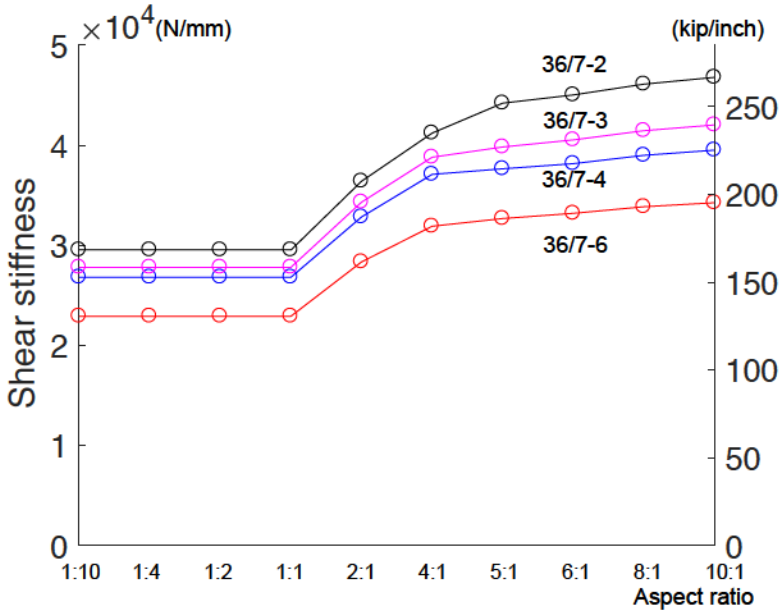

Figure 8-12. Effect of connections perpendicular to purlin

8.7 Comparison of Shear Stiffness between FEM and DDM

8.7.1 Comparison of G_s' and G_c'

In one set of FE models in Table 8-4, we assume the connectors are at all FE mesh nodes along the panel edge and sidelaps (footnote b/d and b/c in Table 8-4). This boundary condition can eliminate the effect of warping deformation and connection slip. In this case shear stiffness $G' = G_s'$ and it is 52758 N/mm (304.5 kip/in.) from FEM, while it is 52149 N/mm (298.0 kip/inch) from DDM prediction.

By making the 'length' of the finite element models (the dimension perpendicular to purlin) as large as 50 times the 'width' of the models, the warping stiffness will be as

large as infinity (From Eq. 8-7). For these special cases, shear stiffness of the steel deck from connection slip can be obtained from the equation below:

$$G_c' = \frac{1}{\frac{1}{G'} - \frac{1}{G_s'}} \tag{8-14}$$

G_c' from DDM are from Eq. (8-9)-(8-12). G_c' for different panels is provided and compared in Figure 8-13. From the plot we can see that for models 36/4 and 36/5, FE results can well predict the shear stiffness from connection slip. However, as the number of connectors in the model increases, the difference between the FE prediction and the DDM prediction is increasing - FEM prediction is always larger than DDM prediction.

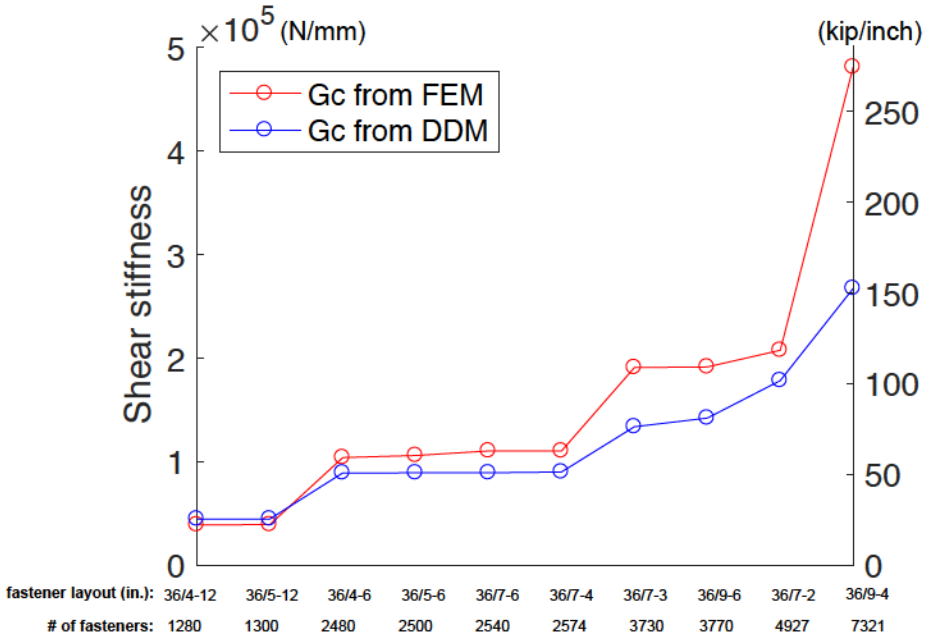

Figure 8-13. Shear stiffness from connection slip G_c' of FEM and DDM

This FE model does not use discrete springs, but rather the local flexibility that derives from applying a point load to a plate element. For the extreme cases with many fasteners, each loading point in the mesh is not independent. (See the influence area in Figure 8-9) In the real word it also don't act independently and it is not clear whether the FE or DDM predictions are more accurate in this case.

8.7.2 Warping Stiffness G_d'

For selected finite element models (Table 8-4 footnote d), all fasteners are coincident with the FE mesh nodes in the perpendicular-to-purlin direction. The large amount of fasteners can eliminate connection slip effect, and the shear stiffness from edge warping can be expressed as following:

$$G_d' = \frac{1}{\frac{1}{G'} - \frac{1}{G_s'}} \tag{8-15}$$

The FE modeling prediction of shear stiffness caused by warping is provided in Table 8-6. By comparing the results in Table 8-2 we can see that DDM and FEM predictions are quite different. In DDM01 (1981), the expression for warping stiffness is calculated from the assumption of a cantilever beam with springs distributed along the panel. Apparently this assumption varies significantly from the warping behavior obtained in the FE model. It is also possible the S4R in shear is providing artificially high results Additional study may be needed.

Table 8-6. G_d' calculated from finite element modeling
(a): in unit N/mm

across corrugation	along corrugation	aspect ratio 1:4	1:2	1:1	2:1	4:1
36/4	12	25527.8	25527.8	25527.8	50765.2	98646.8
	6	25527.8	25527.8	25527.8	50765.2	98646.8
36/5	12	39268.9	39268.9	39268.9	67467.1	127933.4
	6	39268.9	39268.9	39268.9	67467.1	127933.4
36/7	6	84262.1	84262.1	84262.1	159275.1	297766.6
	4	84262.1	84262.1	84262.1	159275.1	297766.6
	3	84262.1	84262.1	84262.1	159275.1	297766.6
	2	84262.1	84262.1	84262.1	159275.1	297766.6
36/9	6	85148.7	85148.7	85148.7	161714.3	303614.3
	4	85148.7	85148.7	85148.7	161714.3	303614.3

(b): in unit kip/inch

across corrugation	along corrugation	aspect ratio 1:4	1:2	1:1	2:1	4:1
36/4	12	145.9	145.9	145.9	290.1	563.7
	6	145.9	145.9	145.9	290.1	563.7
36/5	12	224.4	224.4	224.4	385.5	731.0
	6	224.4	224.4	224.4	385.5	731.0
36/7	6	481.5	481.5	481.5	910.1	1701.5
	4	481.5	481.5	481.5	910.1	1701.5
	3	481.5	481.5	481.5	910.1	1701.5
	2	481.5	481.5	481.5	910.1	1701.5
36/9	6	486.6	486.6	486.6	924.1	1734.9
	4	486.6	486.6	486.6	924.1	1734.9

8.8 Discussion

In this chapter, the elastic shear "diaphragm" stiffness of bare steel deck is explored through shell finite element modeling. The effect of different fastener layout and diaphragm dimensions is considered. Shell FE models are built in ABAQUS and modeling results are compared with AISI 310/Diaphragm Design Manual (DDM) prediction. The diaphragm stiffness (G') term could be written in a series of three stiffness terms: pure shear (G_s'), warping (G_d') and connection slip (G_c'). The finite element prediction for G_s' and G_c' agrees well with the DDM prediction. However, prediction for the G_d' term attributed to warping is stiffer than DDM prediction. This

work shows that shell finite element models are capable of capturing the complex deformation that are inherent in the shear behavior of diaphragm composed of inter-connected steel deck. Differences in the model and methods in DDM suggest that additional investigation into the warping deformation prediction of DDM is warranted.

8.9 Acknowledgements

This chapter was part of the U.S. National Science Foundation sponsored SDII project: NSF-CMMI-1562821: NEESR-CR: Transforming Building Structural Resilience through Innovation in Steel Diaphragms. The project also received supplementary support and funding from AISC, AISI, SDI, SJI, and MBMA. Project updates are available at http://steeli.org/. Any opinions, findings, and conclusions or recommendations expressed in this publication are those of the author(s) and do not necessarily reflect the views of the National Science Foundation, nor the industry sponsors.

8.10 References

[1] https://www.canam-construction.com/en/construction-products/steel-deck/

[2] Bian, G., Torabian, S, and Schafer, B. W. (2016). "Reduced Order Models for Profiled Steel Diaphragm Panels." *Proceedings of Wei-Wen Yu International Specialty Conference on Cold-Formed Steel Structures 2016*, Baltimore, MD, USA.

[3] Steel Deck Institute. Diaphragm Design Manual, first edition, 1981.

[4] Steel Deck Institute. Diaphragm Design Manual, fourth edition, 2015.

[5] AISI-S310-16. North American Standard for Design of Profiled Steel Diaphragm Panels.

[6] http://steeli.org/

CONCLUSIONS

This dissertation summarized the author's Ph.D. research on modeling work of cold-formed steel members and systems.

Based on statistical results, for most available thin-walled open cross sections in the U.S., their torsional behavior is dominated by warping response. In Chapter 2, based on a small series of torsion tests on a cold-formed steel lipped channels, finite element models in ABAQUS are developed, and these models demonstrates that inelastic reserve is existed before the member fails. Similar to design expressions in Direct Strength Method developed previously for axial, shear loading and bending, torsional slenderness is used to predict the ultimate torsional strength in this work.

A model for cold-formed steel framed, wood sheathed shear wall is developed in Chapter 3 and the model is used to predict shear wall lateral response. An OpenSees model is developed with beam-column element as cold-formed framing and rigid diaphragm for sheathing. The stud-to-sheathing connections are modeled as zero-length springs utilizing a Pingching04 material response developed from isolated fastener tests. Models for different shear wall configurations are validated against previous conducted, monotonic and cyclic shear wall tests, and showed good agreement on maximum force, displacement and energy dissipation. The OpenSees fastener-based models can give a conservative prediction of the shear wall lateral resistance, which can be applied in future research.

Cold-formed steel framed, wood sheathed shear wall has two main limit states: fastener failure and chord stud failure. Fastener based shear wall model is extended to a model with chord stud nonlinearity in Chapter 4. This advanced model can be used to demonstrate the switch of limit states from fastener failure to chord stud buckling at a high level of superimposed gravity load. Verification of this extended fastener based model is provided with ABAQUS high fidelity models, and the load-displacement results from OpenSees model and ABAQUS model agree well. This is the first time a model is proposed to consider chord stud failure mode.

CFS-NEES experiment and simulation of a full-scale cold-formed steel building showed that the gravity wall can benefit the full wall system on its lateral resistance capacity. Previously proposed fastener based shear wall model is used to predict the lateral behavior for different shear wall and gravity wall combinations in Chapter 5. In the studied example in this thesis, the gravity wall can carry as much as half of the lateral force, although it is not accounted for in the design process.

A typical CFS shear wall may rely on more than 100 connections with each connection having variation at its strength. Although each fastener as a subsystem has high variable, but shear wall as a full system benefits from a system effect and has less variation. In the cases studied herein the coefficient of variation for individual fastener strength is 13%, while for the system strength the coefficient of variation is predicted to be less than 3%. On the other hand, mean shear wall strength is modestly reduced (approximately 3%) below deterministic predictions. Examination of existing and proposed shear wall design

methods indicate that the predicted reduction in variability is a major system benefit when considering reliability. Based on the analysis provided herein the current resistance factor used in the American Iron and Steel Institute standard for cold-formed steel framed shear walls (AISI S400-15) may be excessively conservative.

Diaphragm plays another important role in cold-formed steel building as part of lateral force resistance system. However, the effect of diaphragm on lateral behavior is unknown either from experiment or simulation. In Chapter 7 and Chapter 8, bare steel deck modeling is presented in two aspects: development and utilization of a reduced order model; and shell finite element modeling of elastic shear stiffness of bare steel deck. Reduced order models increase computational efficiency by reducing the degrees of freedom. In this reduced order model important features are maintained and no compromise is required. The equivalent orthotropic plate reduced order model pursued here can accurately reproduce a variety of complex global stiffness behavior under idealized conditions, and with the explicit expressions of Xia et al. (2012) are relatively easy to implement. However, local features of the model are lost, and when applied in non-idealized conditions these features become important to the response and the accuracy of the model degrades. The application of equivalent orthotropic plate models must be done with care or the results can be overly conservative.

Under lateral loads bare deck diaphragm plays a particularly important role as a distribution element, one in which the in-plane shear behavior of the panel is paramount. Shell finite element modeling of elastic shear stiffness of bare steel deck is explored for

different panel dimensions and fastener layout. According to the shear mechanism, shear deformation can be treated as three separated terms: panel shear, warping deformation and connection slip. Shear stiffness is isolated as a series of separated stiffness according to these three deformations from finite element modeling. Finite element models are built and used to predict these shear stiffness by changing its boundary conditions. The result shows that the pure shear and connection slip shear stiffness terms agree well with Diaphragm Design Manual prediction, but the warping term has some discrepancy between FEM and DDM prediction.

FUTURE WORK

The torsion work in Chapter 2 is a limited investigation of torsion in cold-formed steel members. Significant work remains to develop a robust means of handling torsion. Although thin-walled members are dominated by warping torsion, additional cases (e.g. due to thickness, end boundary conditions, etc.) where the contribution of St. Venant torsion is non-negligible need further study. Systematic study of the impact of this longitudinal variation of warping stresses is needed to understand the impact on buckling modes and on yielding. Simplified methods are needed for predicting torque under partial or full plastification. The lack of a simplified calculation for plastic torque in thin-walled members leads to the type of gross simplifications provided in the currently developed prediction methods. Focused tests and models varying torsional slenderness in each of local, distortional, and global buckling are needed to fully understand the complete torsional strength. Torsion in combined loading should be revisited with the goal of investigating limit-states based strength interaction equations to replace the stress-based expressions in current use in design. Further testing, modeling, and analytical developments are all needed.

In the research work of cold-formed steel framed, OSB sheathed shear wall modeling, significant additional work remains to utilize the model more formally in seismic shear wall design and in full building models. Based on the current available fastener tests data (Moen et al. 2016, Peterman et al. 2012 and Landolfo et al. 2016), the fastener-based model can be used for modeling different shear wall configurations and the modeling results can be compared with current design specification (AISI S400). In Chapter 4, the

authors utilized an element with Pinching04 material for shear wall chord studs, which can estimate the chord stud buckling failure. A more systematic research remains to explore the shear wall behavior under different superimposed gravity load for capacity-based design. The modeling results need to be formalized and suggestions need to be provided for a more accurate protection factor for capacity-based design. For CFS gravity modeling work, more wall configurations and building details need to be considered to explore the gravity wall effect on the whole wall lateral resistance. In the work of CFS shear wall Monte Carlo simulation, additional analyses are recommended and complications related to seismic reliability discussed, all with a goal of advancing reliability and design for cold-formed steel framed shear walls.

Future work remains for research on shear stiffness of bare steel deck. Finite element models need to be extended to more broad dimensions, and nonlinear fasteners based on deck panel shear test can be included into the model. Warping mechanism in DDM needs to be checked and a more accurate expression needs to be proposed. Optimization of connection layout for both shear wall and bare steel deck is potentially another important future work.

BIOGRAPHICAL STATEMENT

Guanbo Bian attended Johns Hopkins University from August 2012 to May 2017, where he received his M.S. in Applied Math & Statistics and Ph.D. in Civil Engineering. His Ph.D. dissertation focused on modeling cold-formed steel members, shear wall and diaphragm, and reliability assessment of cold-formed steel building system. Before coming to Hopkins, Guanbo graduated with B.S. and M.S. in Civil Engineering from Dalian University of Technology in China.

After graduation, Guanbo will work on financial modeling and analytics in industry.